CHEMICAL REVIEWS

pubs.acs.org/CR

Review

Fundamental Aspects of Phase-Separated Biomolecular Condensates

Huan-Xiang Zhou,* Divya Kota, Sanbo Qin, and Ramesh Prasad

Cite This: https://doi.org/10.1021/acs.chemrev.4c00138

Read Online

ACCESS | Metrics & More | Article Recommendations | Supporting Information

ABSTRACT: Biomolecular condensates, formed through phase separation, are upending our understanding in much of molecular, cell, and developmental biology. There is an urgent need to elucidate the physicochemical foundations of the behaviors and properties of biomolecular condensates. Here we aim to fill this need by writing a comprehensive, critical, and accessible review on the fundamental aspects of phase-separated biomolecular condensates. We introduce the relevant theoretical background, present the theoretical basis for the computation and experimental measurement of condensate properties, and give mechanistic interpretations of condensate behaviors and properties in terms of interactions at the molecular and residue levels.

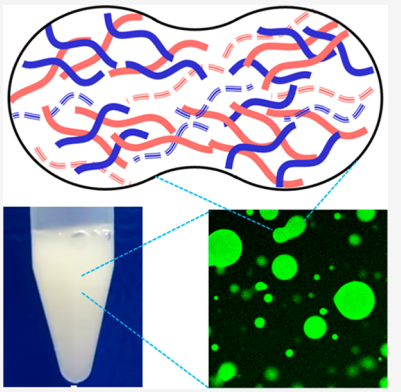

CONTENTS

Received: February 15, 2024
Revised: May 17, 2024
Accepted: May 23, 2024

1. INTRODUCTION

Biology is undergoing a revolution, where biomolecular condensates are upending our understanding in much of molecular, cell, and developmental biology.[1−8] These condensates include membraneless organelles such as P granules, stress granules, and nucleoli, and are formed through phase separation.[9−11] Literature reports of biological processes being mediated by condensates are growing at a dizzying rate.[12−39] Ample evidence also indicates that condensates are linked with neurodegeneration, cancer, and other diseases.[8,40−42] We are now starting to gain better and better physical understanding of the properties and complex behaviors of biomolecular condensates.[43−47]

Phase separation is the process where a dense phase (comprising the condensates) emerges from the bulk solution. The dense phase is typically seen as micronsized droplets under a microscope (Figure 1a), which scatter light, thereby making the solution appear cloudy. According to theory, phase separation of a protein solution occurs for the same reason that the liquid and vapor phases of water coexist at particular thermodynamic conditions (Figure 1b).[44] Similar to the much higher density of liquid water relative to vapor, the dense phase has much higher protein concentrations than the surrounding bulk phase. High concentrations correspond to short distances between solute molecules. Therefore, the dense phase, like liquid water, is stabilized by multivalent, nonspecific interactions of the constituent macromolecules, whereas the bulk phase, like water vapor, is favored by translational entropy of these molecules.

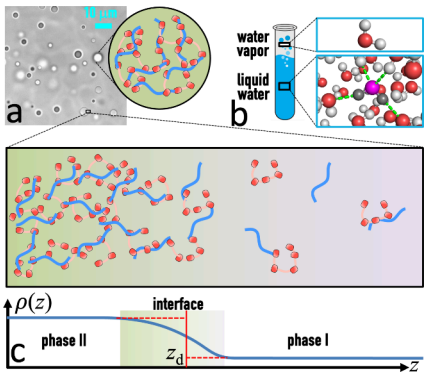

Figure 1. Molecular nature of biomolecular condensates. (a) Protein droplets and the intermolecular interaction networks inside. The brightfield image has appeared in ref 48. Copyright 2019 the original authors. (b) Analogy between biomolecular phase separation and water liquid−vapor coexistence. (c) Top: molecular picture of the interface. Bottom: density profile in the interfacial region.

Phase separation of polymer solutions was first systematically studied in the 1930s and a theoretical explanation was provided by Flory in 1942.[49] In the polymer literature, condensates are commonly referred to as coacervates. For biomacromolecules, phase separation was observed on purified (folded) proteins in the 1970s, on their way to crystallization.[50,51] From the 1980s to the 2000s, the Benedek group conducted studies on the two-phase equilibria of the eye lens proteins γ-crystallins.[52−57] It was toward the end of this period that the field of biomolecular phase separation started its rapid rise, ushered by reports that condensates formed by intrinsically disordered proteins (IDPs) make up membraneless organelles such as P granules[9] and mediate essential cellular functions such as the initiation of actin polymerization.[58] While proteins are major players, these and subsequent studies have shown that RNA can be important constituents of biomolecular condensates (refs 10, 11, 15, 17, 18, 20, 26, 29, and 59−97). (For recent reviews, see refs 98−102.) In the presence of Mg^{2+}, RNAs can phase separate without any proteins.[103−110] Phase separation of protein−DNA mixtures has also been observed[13,23,30,31,111−125] (see ref 126 for a recent review). DNA with sticky ends has been designed to phase separate.[127,128] Lastly, small molecules including ATP are found to drive phase separation of IDPs, by forming bridging interactions[81,129−135] or by regulating protein conformations[136,137] or protein−protein binding[138,139] (see ref 140 for a recent review).

For most biomolecular condensates, an important distinguishing feature is that they behave like liquids. As the surrounding bulk phase, a dilute protein solution, is obviously a liquid, the process that forms biomolecular condensates is also called liquid−liquid phase separation (LLPS; see Table 1 for a list of all abbreviations). The liquid-like behaviors of biomolecular condensates include the tendency to adopt a spherical shape, the spread over a solid surface like a glass slide, and the disposition to fuse with each other upon contact. The corresponding behaviors of water droplets are largely driven by surface tension, which tends to minimize the surface area and

https://doi.org/10.1021/acs.chemrev.4c00138
Chem. Rev. XXXX, XXX, XXX−XXX

Table 1. List of Abbreviations

A1-LCD	hnRNPA1 low-complexity domain
FMAP	Fast Fourier transform-based modeling of atomistic protein−protein interactions
FRAP	Fluorescence recovery after photobleaching
GAFF	General Amber force field
IDP	Intrinsically disordered proteins
LCST	Lower critical solution temperature
LLPS	Liquid−liquid phase separation
MSD	Mean square displacement
OT	Optical-tweezers instrument
RPA	Random phase approximation
UCST	Upper critical solution temperature

hence results in a spherical shape of a water droplet. For water droplets, the exterior is air (plus a small amount of water vapor) and can thus be treated as a vacuum. For protein droplets, the exterior is the bulk phase. In contrast to membrane-bound organelles, there is no membrane that separates the two phases. Rather, both solvent and solute molecules can freely exchange between the phases (hence the term membraneless organelles). The interphase interface is a finite region where the protein concentrations transition from high values to low values (Figure 1c).

The liquid-like properties are essential for the functions of many biomolecular condensates. For example, free exchange of molecules between the bulk and dense phases allows for the sequestration of certain molecules inside condensates (e.g., mRNA inside stress granules[82,88,141]), and for biochemical reactions to occur at elevated concentrations of reactants (and enzymes) inside condensates[142] and for the release of products into the bulk phase.[15,143] Moreover, liquid-like condensates can readily assemble and disassemble in response to, e.g., change in constituent concentrations[9,31,144] or posttranslational modifications.[13,58,66,78,141,145] However, it is important to emphasize that biomolecular condensates are only partly liquid-like; they are also partly solid-like. Because molecules are free to move in liquids but are confined to their local positions in solids, liquids respond to a moving force as a viscous flow (Figure 2a) whereas solids respond to a static force as an elastic deformation in shape (Figure 2b). Materials including biomolecular condensates that are partly liquid-like and partly solid-like are said to be viscoelastic. Some biomolecular condensates are purely solid-like, in the form of reversible aggregates (Figure 2c) or gels. Over time, many condensates transition from more liquid-like to more solid-like, a process known as aging.

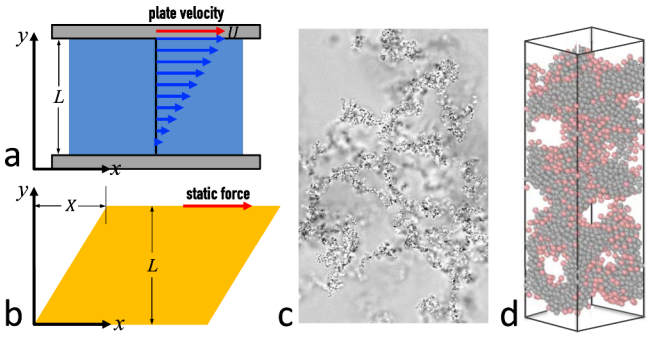

Figure 2. Different material states. (a) A liquid in a steady shear flow. (b) A solid under a static shear strain. (c) Reversible aggregates as a solid-like form of biomolecular condensates. A cropped version of the brightfield image is shown in Figure 15d and has appeared in ref 146. Copyright 2020 American Chemical Society. (d) A gel produced by arrested spinodal decomposition in coarse-grained simulations. Reproduced from ref 147. Copyright 2022 the original authors.

This review provides the fundamentals for understanding the complex behaviors and properties of biomolecular condensates. We also strive to present mechanistic interpretations of experimental data from the literature, and hope that the materials here can help others derive interpretations of their data. Particular attention is paid to the integration of theoretical models and molecular simulations with experimental observations in deriving physical insights.

2. THEORETICAL BACKGROUND

Throughout this review, we take the simplifying conceptual view where only solute molecules are considered explicitly. The solvent is in the background but affects the interactions between solute molecules. The intermolecular interaction energy is thus actually a potential of mean force, with solvent degrees of freedom averaged out. When such effective interactions between solute molecules vanish, the solution is called "ideal", similar to an ideal gas. For solutions as well as for gases, intermolecular interactions cause deviations from ideality.

With this conceptual view, a solution with a single protein solute species is then a one-component system; likewise when the solution contains two different proteins it is a two-component system. The thermodynamic state of a single-component system is specified by its temperature (T) and pressure (p). For a two-component system, we need to additionally specify its composition, e.g., the mole fraction (x_1) of one of the two components. The thermodynamic state of a ν-component system is specified by $\nu + 1$ variables: T, p, and x_i where $i = 1$ to ν - 1.

Exceptions to the implicit view of solvent will be made when presenting the Flory−Huggins theory for polymer solutions (Subsection 2.4) and when discussing explicit-solvent molecular dynamics simulations (Subsection 3.1.5). Meanings of mathematical symbols are collected in Table 2.

2.1. Phase Boundaries

When the system forms two coexisting phases (labeled as I and II), the following conditions must be satisfied:

$$T_{\mathrm{I}} = T_{\mathrm{II}} \tag{1a}$$

$$p_{\mathrm{I}} = p_{\mathrm{II}} \tag{1b}$$

$$\mu_{i,\mathrm{I}} = \mu_{i,\mathrm{II}}, \quad i = 1 \text{ to } \nu \tag{1c}$$

where μ_i denotes the chemical potential, or free energy on a per molecule basis, of component i in a given phase. The two phases require a total of $2(\nu + 1)$ variables for full specification, but eqs 1a−1c contain only $\nu + 2$ identities, $2(\nu + 1) - (\nu + 2) = \nu$ variables remain free when the two phases coexist. In particular, for a one-component system, there is one such free variable. This could be either T or p, but not both. For example, at 1 atmospheric pressure, the liquid−vapor phase transition of water occurs precisely at 100 °C. That is, when p is varied, T at two-phase coexistence cannot independently vary but is a function of p. This $T - p$ curve defines the boundary between the phases (Figure 3a). Each point on the boundary corresponds to two coexisting phases, one at a low concentration (the bulk or dilute phase) and one at a high concentration (the dense phase).

https://doi.org/10.1021/acs.chemrev.4c00138
Chem. Rev. XXXX, XXX, XXX−XXX

Table 2. List of Symbols

Symbols	Meanings
a	Radius of a solid bead
α	Constant in van der Waals equation
A	Area
b	Constant in van der Waals equation
B_l	Virial coefficients
C	Concentration
d	Range of intermolecular interaction
$\mathbf{e}$	Unit vector
E	Internal energy
$f(x)$	A function
$\mathbf{f}$	Force between two molecules
f	Helmholtz free energy per unit volume
F, $\mathbf{F}$	Force
$\mathcal{F}$	Helmholtz free energy
g	Gibbs free energy per unit volume
$\mathbf{g}$	Force per unit mass
G_0	Shear modulus
$G(t)$	Shear relaxation modulus
$G^*(\omega)$	Complex shear modulus
$G'(\omega)$, $G''(\omega)$	Elastic modulus and viscous modulus
$\mathcal{G}$	Gibbs free energy
H	Height
$\tilde{\mathrm{I}}$	Unit tensor
k_B	Boltzmann constant
$\mathbb{K}$	Instantaneous total kinetic energy
L	Length
m	Mass
$\mathbf{n}$	Unit normal vector
n, n'	Particle index
N	Number of molecules
p	Pressure
$\tilde{p}$	Pressure tensor
$\tilde{\mathbb{p}}$	Instantaneous pressure tensor
p	Momentum vector
$P_l(x)$	Legendre polynomials
q	NMR relaxation parameter
$Q_l(x)$	Variant form of Legendre polynomials
r	Intermolecular distance; radial distance
R	Droplet radius
s	Axial distance; separation between two interfaces
S	Entropy

Symbols	Meanings
t	Time
$\mathbf{t}$	Unit tangential vector
T	Temperature
$\mathbf{u}$	Displacement vector
U, $\mathbf{U}$	Velocity
v	Molecular-scale volume; velocity
$\mathbf{v}$	Velocity vector
V	Volume
w	Radius of a Gaussian laser beam
W	Work
$\mathbb{W}$	Virial
x, y, z	Cartesian coordinates
x	Mole fraction
$\mathbf{x}$	Position vector
X	Bead position
Z_N	Partition function
α	A critical exponent
β	$1/k_BT$
γ	Interfacial tension
δ, Δ	Phase shift
$\tilde{\varepsilon}$	Strain-rate tensor
ϵ	Magnitude of intermolecular attractive energy
η	Viscosity
θ	Polar angle
$\Theta(x)$	Heaviside step function
κ	Spring constant or stiffness
λ	Stickiness parameter
μ	Chemical potential
ν	Number of solute components
ξ	Friction coefficient
ρ	Number density; probability density
ϱ	Mass density
$\tilde{\sigma}$	Shear-strain tensor
τ	Time difference; time constant
$\tilde{\tau}$	Stress tensor
ϕ	Volume fraction; azimuthal angle
$\varphi(r)$	Intermolecular interaction energy at distance r
Φ	Total potential energy
χ	Flory–Huggins interaction parameter; effective spring constant
Ψ	Stream function
ω	Angular frequency

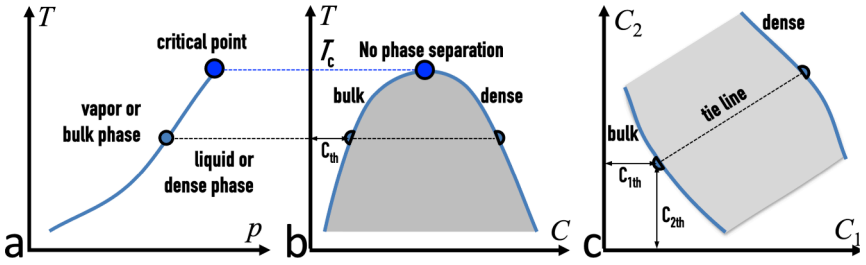

Figure 3. Different forms of phase boundaries. (a) Phase boundary of a one-component system on the $T-p$ plane. (b) The same phase boundary shown as a binodal. At a given temperature, the concentrations of the two phases (including C_{th} for the bulk phase) are fixed even as the total amount of the solute is changed. The latter change only affects the volume fractions of the two phases. (c) The phase boundary of a two-component system at a given temperature. Now the concentrations vary according to the composition (i.e., molar ratio). Each composition determines the concentrations of the two components in each of the two phases; a tie line connects the concentrations in the two phases.

https://doi.org/10.1021/acs.chemrev.4c00138
Chem. Rev. XXXX, XXX, XXX−XXX

Another form of phase boundary is to plot the concentrations of the two phases at different temperatures (Figure 3b); this plot is called a binodal. At a given temperature, when the concentration of the protein solution is below the bulk concentration on the binodal, phase separation cannot happen. When the protein concentration is increased to between the bulk and dense concentrations on the binodal, phase separation happens, because the initial homogeneous solution is thermodynamically less stable than the phase-separated state. The amount of protein that is found in the dense phase, as specified by the volume fraction of the dense phase, depends on the initial concentration. The higher the initial concentration (closer to the high-concentration arm of the binodal), the higher the total volume of protein droplets. In the physics literature, the minimal concentration required for phase separation is called the saturation concentration. We refer to it as the threshold concentration and denote it as C_{th}.

For water, there exists a high temperature, 374 °C, above which there is no more liquid−vapor phase transition. This point is known as the critical point and the temperature is known as the critical temperature (T_c). In essence, at such a high temperature, there is no more difference between the two phases. Biomolecular condensates usually exhibit such a critical point. The critical temperature for most biomolecular condensates serves as the ceiling (upper critical solution temperature, or UCST) of phase-separation temperatures (Figure 3a, b). For some condensates, T_c serves as the floor (lower critical solution temperature, or LCST) of phase-separation temperatures.[110,145,148−150] We limit ourselves to UCST. Both C_{th} and T_c can serve as an indicator of the easiness of phase separation: proteins with a lower C_{th} or a higher T_c more readily phase separate. Biomolecular condensates typically have C_{th} at the low μM or even sub-μM range, allowing for their formation at physiological concentrations.

For a two-component system, the number of independent variables at two-phase coexistence increases to two. At a given temperature, the threshold concentrations are no longer a single value but are a variable (Figure 3c), changing with the initial molar ratio of the two components. Similar to the one-component system, the dense phases of biomolecular condensates are characterized by much higher concentrations than the bulk phases, at least for the major components, i.e., those with the highest mole fractions and hence drivers of phase separation. A different situation is represented by the phase separation of oil-vinegar mixtures: here one phase is rich in oil and another is rich in vinegar. Sometimes analogy has been drawn between biomolecular condensates and oil-vinegar mixtures. This analogy is not entirely appropriate, as the main difference between the condensate phase and the surrounding bulk phase is in the concentrations, not compositions, of the major components; a much better analogy, as has been made above, is between phase separation and vapor−liquid (or gas−liquid) phase transition.

In making the latter analogy, the pressure in a gas−liquid system corresponds to the osmotic pressure of a protein solution, i.e., the increase in solution pressure due to the presence of protein solute molecules.[151] All free energies, including the Gibbs free energy ($\mathcal{G}$), Helmholtz free energy ($\mathcal{F}$), and chemical potential, are relative to the hypothetical undissolved state (where solute and solvent are separated). Also note that we use the terms concentration and density interchangeably.

2.1.1. Phase Separation as a Noise Buffering Mechanism? The fact that, at a given temperature, a one-component system upon phase separation has a fixed concentration (C_{th}) in the bulk phase (Figure 3b) motivated Kosin et al.[152] to propose that LLPS provides a mechanism to buffer noise, i.e., concentration fluctuations, in cells. However, Riback and Brangwynne[153] argued that, for multicomponent systems, C_{th} for each component is no longer fixed but varies with the composition as illustrated in Figure 3c. Riback et al.[143] then showed that nucleoli and other condensates do not have fixed C_{th}, as endogenous LLPS is driven by multicomponent interactions. This debate has stimulated theoretical studies.[154]

2.2. van der Waals Equation of State

A simple model for explaining gas−liquid phase transition and, by extension, phase separation is provided by the van der Waals equation of state:[155]

$$(p + aN^2/V^2)(V - bN) = Nk_BT \quad (2)$$

where N is the number of molecules, V is the volume of the container, and k_B is the Boltzmann constant. Without the terms with coefficients a and b, eq 2 reduces to the ideal gas law. These terms represent corrections to the pressure and volume, respectively, due to intermolecular interactions. These corrections were motivated by a generic form of intermolecular interaction energy function $\varphi(r)$ displayed in Figure 4a, which

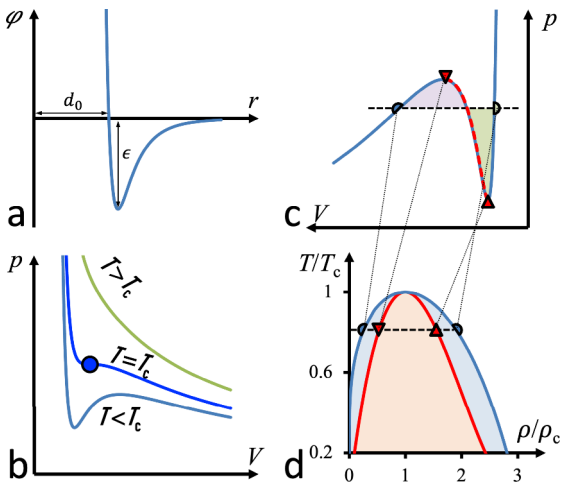

Figure 4. van der Waals model for the gas−liquid phase transition of simple fluids and for the phase separation of protein solutions. (a) A generic intermolecular potential, as represented by the Lennard-Jones potential $\varphi(r) = 4\epsilon\,[(d_0/r)^6 - (d_0/r)^{12}]$. (b) p−V isotherms. (c) The van der Waals loop and Maxwell equal-area construction. Semicircles indicate binodal densities; triangles indicate spinodal densities. (d) The binodal (blue curve) and spinodal (red curve).

features soft attraction (with magnitude ϵ) when the molecules come into contact and steric repulsion when they further approach to become overlapping with each other (intermolecular distance $r < d_0$). The steric repulsion gives rise to the volume correction in the van der Waals equation, as the volume actually accessible to each molecule is less than the volume of the container. The soft attraction gives rise to the pressure correction, as intermolecular attraction reduces the chance of molecules bombarding the container wall and hence the measured pressure. These considerations lead to

$$a = \nu_{att}\epsilon \quad (3a)$$

https://doi.org/10.1021/acs.chemrev.4c00138
Chem. Rev. XXXX, XXX, XXX−XXX

$$b = v_{rep} \tag{3b}$$

where v_{att} is a volume set by the width of the soft attraction and v_{rep} is a volume set by the width of the steric repulsion.

Figure 4b displays the $p - V$ relation of eq 2 at constant temperatures (with N fixed). At high temperatures, p monotonically decreases with increasing V, similar to an ideal gas. As T is decreased, at a certain value (i.e., the critical temperature, T_c), the $p - V$ isotherm starts to be nonmonotonic. The nonmonotonic portion is known as the van der Waals loop, and is a signature for gas−liquid phase transition. The volumes (or number densities, $\rho \equiv N/V$) of the two coexisting phases are determined by the conditions of eqs 1a−1c. By definition, every point on a $p - V$ isotherm has the same temperature; so eq 1a is automatically satisfied. If we draw a horizontal line through the van der Waals loop, the intersection points all have the same pressure, thereby satisfying eq 1b (Figure 4c). Lastly we can adjust the vertical position of this horizontal line to satisfy eq 1c. That latter condition is satisfied when the horizontal line is at a position such that the area under the $p - V$ curve and above the line (shaded in magenta) and the area over the $p - V$ curve and below the line (shaded in green) are equal. This procedure for identifying the coexisting gas and liquid phases is known as Maxwell construction.[156] The equal-area condition ensures that the difference in Gibbs free energy ($= N\mu$) is zero between the gas and liquid phases. The corresponding densities become two points on the binodal (blue curve in Figure 4d). Equal-area construction can also be carried out over $\mu - \rho$ isotherms (Subsection 3.1.1).[157]

The critical point is where the van der Waals loop collapses into a single point (indicated by a circle in Figure 4b). At this special point, the first and second derivatives of the $p - V$ curve are both zero:

$$\left.\frac{\partial p}{\partial V}\right|_{N,T=T_c} = 0 \tag{4a}$$

$$\left.\frac{\partial^2 p}{\partial V^2}\right|_{N,T=T_c} = 0 \tag{4b}$$

These conditions allow us to find the critical point as

$$k_B T_c = \frac{8a}{27b} \tag{5a}$$

$$\rho_c = \frac{1}{3b} \tag{5b}$$

Using eqs 3a and 3b in eq 5a, we obtain

$$k_B T_c = (8v_{att}/27v_{rep})\epsilon \tag{5c}$$

The last expression captures the very important conclusion that the critical temperature increases with the strength of intermolecular attraction—the stronger the attraction, the higher the critical temperature. An ideal gas does not have intermolecular attraction (or repulsion) and hence cannot undergo gas−liquid phase transition. Neither can a hard-sphere liquid, which has steric repulsion but not attraction.

2.2.1. Mechanisms of Phase Separation. Note that the van der Waals loop has a portion, drawn as a red dash in Figure 4c and demarcated by two triangles at the local maximum and local minimum, where the pressure increases with increasing volume. The simultaneous increase of p and V is unphysical and indicates that the system is unstable over this range of densities. The two bounds of this density range define the spinodal (red curve in Figure 4d). As these bounds occur at the extrema of the $p - V$ curve, they can be found by requiring that the first derivative be zero:

$$\left.\frac{\partial p}{\partial V}\right|_{N,T} = 0 \text{ on spinodal} \tag{6a}$$

This condition leads to the following equation for the spinodal:

$$\frac{T}{T_c} = \frac{4}{9}\frac{\rho}{\rho_c}\left(1 - \frac{\rho}{3\rho_c}\right)^2 \tag{6b}$$

Within the spinodal, the system is unstable and thus spontaneously undergoes phase transition. The mechanism by which this transition happens is called spinodal decomposition (see Subsection 3.1.4).

Between gas and liquid densities, the van der Waals loop has two regions where p decreases with increasing V as expected of physical systems (Figure 4c). These regions are located inside the binodal but outside the spinodal, one on the low-density side and the other on the high-density side (Figure 4d). In both of these regions, the system is metastable and correspondingly phase transition can be slow. An oversaturated vapor (on the low-density side) condenses by forming molecular clusters, referred to as nuclei. For a spherical nucleus with radius R, the difference of its Gibbs free energy from that of the oversaturated vapor of the same volume is[158]

$$\Delta\mathcal{G}(R) = -\Delta g_V(4\pi R^3/3) + \gamma(4\pi R^2) \tag{7}$$

where Δg_V is a positive quantity denoting the free-energy difference between a unit volume of oversaturated vapor and a unit volume of the nucleus, and γ, known as surface tension, is another positive quantity representing the increase in the energy of the nucleus per unit surface area created. (see Subsection 2.5). Starting from a 0 value at $R = 0$, $\Delta\mathcal{G}(R)$ becomes more and more positive with increasing R, and hence it is more favorable for the nucleus to disappear. However, upon reaching a critical size where $\Delta\mathcal{G}(R)$ is at its maximum, further growth becomes favorable. Equation 7 suffers from a number of deficiencies, including not accounting for the fact that the maximum of $\Delta\mathcal{G}(R)$ should vanish when the initial vapor approaches the spinodal.[159] Nevertheless it makes the crucial point that condensation by the nucleation-and-growth mechanism, in contrast to spinodal decomposition, is a slow process. It likewise qualitatively models the evaporation of superheated liquids (on the high-density side); the nuclei are now gas bubbles.

In short, gas−liquid phase transition and also phase separation occur by two distinct mechanisms: by (spontaneous) spinodal decomposition inside the spinodal and by (slow) nucleation and growth between the spinodal and binodal. Both spinodal decomposition and nucleation and growth have been observed for the formation of biomolecular condensates.[28,144,160−168] The binodal and spinodal from the van der Waals equation, displayed in Figure 4d, illustrate another fact: the area within the spinodal is much larger than that between the spinodal and binodal. Based on this fact and the observation that biomolecular condensates are usually formed quickly, Mazarakos et al. have concluded that spinodal decomposition is the dominant mechanism for biomolecular condensates.[147] On the other hand, it has been suggested that cells may want to keep component concentrations to a minimum required for phase

https://doi.org/10.1021/acs.chemrev.4c00138
Chem. Rev. XXXX, XXX, XXX−XXX

separation, i.e., crossing the low-concentration arm of the binodal just enough into the left metastable region, and thus nucleation and growth would the favored mechanism.[169]

2.3. Virial Expansion

A formal way to write the equation of state is a virial expansion:

$$\beta p = \rho + \sum_{l=2}^{\infty} B_l \rho^l \tag{8}$$

where B_l are constants known as virial coefficients. The first term is what is given by the ideal gas law; the higher-order terms thus account for intermolecular interactions. While eq 8 can be viewed as a Taylor expansion, what is interesting is that each B_l coefficient can be calculated from integrals involving precisely l molecules.[170] In particular, the second virial coefficient is

$$B_2 = -\frac{1}{2}\int_0^{\infty} \mathrm{d}r 4\pi r^2 [e^{-\beta\varphi(r)} - 1] \tag{9}$$

where $\beta = 1/k_B T$. A simple intermolecular interaction energy function that conforms to the generic form of Figure 4a is the square-well potential:

$$\varphi(r) = \begin{cases} \infty, & r < d_0 \\ -\epsilon, & d_0 < r < d \\ 0, & r > d \end{cases} \tag{10}$$

Its second virial coefficient is

$$B_2 = \frac{2\pi}{3} d_0^3 - \frac{2\pi}{3}(d^3 - d_0^3)(e^{\beta\epsilon} - 1) \tag{11a}$$

Note that the steric repulsion of the potential makes B_2 positive whereas the soft attraction makes B_2 negative. The stronger the attraction is, the more negative B_2 becomes. Also, the virial coefficients are temperature-dependent. At high temperatures (i.e., small β), we can expand the Boltzmann factor $e^{\beta\epsilon}$ to first order in β, leading to

$$B_2 \approx \frac{2\pi}{3} d_0^3 - \frac{2\pi}{3}(d^3 - d_0^3)\epsilon\beta \tag{11b}$$

B_2 grows more negative with decreasing temperature.

The van der Waals equation of state can be expressed as a virial expansion:

$$\beta p = \frac{\rho}{1 - b\rho} - a\beta\rho^2 \tag{12a}$$

$$= \rho + (b - a\beta)\rho^2 + b^2\rho^3 + b^3\rho^4 + \cdots \tag{12b}$$

The second virial coefficient here is

$$B_2 = b - a\beta \tag{12c}$$

Comparing with eq 11b, we can now see further justification for eqs 3a and 3b in relating a and b to the attractive and repulsive parts of the potential, respectively. Note that the attractive part of the potential contributes only to B_2 and not any higher-order virial coefficient. The dependence of p on ρ as given by eq 12b is nonmonotonic only because B_2 is negative, and a gas−liquid phase transition occurs only when p is a nonmonotonic function of ρ. Equation 12b thus perfectly illustrates why B_2 is an indicator of phase transition. More specifically, the more negative B_2 is, the higher the critical temperature becomes.

The temperature at which B_2 becomes 0 is called the Boyle temperature, denoted as T_B. Setting the right-hand side of eq 12c to 0, one finds

$$k_B T_B = \frac{a}{b} \tag{13a}$$

Compared with eq 5a, we have

$$T_c = \frac{8}{27} T_B \tag{13b}$$

A thermodynamic result that will be used next and also later is the Gibbs−Duhem equation:

$$S\mathrm{d}T - V\mathrm{d}p + N\mathrm{d}\mu = 0 \tag{14a}$$

where S denotes entropy. For processes at constant temperature, the first term drops out. Dividing by V, we find

$$\mathrm{d}p = \rho\mathrm{d}\mu \tag{14b}$$

or

$$\mathrm{d}\mu = \frac{1}{\rho}\mathrm{d}p \tag{14c}$$

Using this last result, we obtain a virial expansion for the chemical potential:[171]

$$\beta\mu = \int_0^{\rho} \mathrm{d}\rho \frac{1}{\rho}\frac{\partial p}{\partial \rho}\bigg|_{\beta} + A_1 \tag{15a}$$

$$= \ln(A_2\rho) + \sum_{l=2}^{\infty} \frac{lB_l}{l-1}\rho^{l-1} \tag{15b}$$

$$\equiv \beta\mu^{\mathrm{id}} + \beta\mu^{\mathrm{ex}} \tag{15c}$$

where A_1 and A_2 are unimportant constants. The first term on the right-hand side of eq 15b expresses the chemical potential of an ideal gas (or ideal solution; denoted as μ^{id}). The higher order terms are due to intermolecular interactions, and together make up the "excess" part (denoted as μ^{ex}). Equation 15b will serve as a motivation for Subsection 3.1.1.

For the van der Waals equation of state, applying eq 15a results in

$$\beta\mu = \ln\left(\frac{A_2\rho}{1 - b\rho}\right) + \frac{b\rho}{1 - b\rho} - 2a\beta\rho \tag{16}$$

The Helmholtz free energy per unit volume is

$$\beta f \equiv \frac{\beta\mathcal{F}}{V} = \beta\mu\rho - p \tag{17a}$$

$$= -\rho + \rho\ln(A_2\rho) - \rho\ln(1 - b\rho) - a\beta\rho^2 \tag{17b}$$

2.4. Flory−Huggins Theory

Flory and Huggins developed a theory for the phase separation of polymer solutions, by combining a lattice model for the entropy of mixing polymer and solvent molecules and a mean-field treatment for interaction energies.[49] The result is the following expression for the change in Helmholtz free energy per unit volume, from the undissolved state where the polymers and solvent molecules are confined to separate subcompartments to the dissolved state with homogeneous polymer−solvent mixing:

https://doi.org/10.1021/acs.chemrev.4c00138
Chem. Rev. XXXX, XXX, XXX−XXX

$$v_1 \beta f = \frac{\phi}{L} \ln \phi + (1 - \phi)\ln(1 - \phi) + \chi_{FH} \beta \phi (1 - \phi) \tag{18}$$

The meanings of the symbols are as follows: v_1 is the volume of a monomeric unit as well as that of a solvent molecule (each of which occupies a single cell in the lattice); L is the chain length of the polymer, measured as the number of monomeric units; $\phi = Lv_1\rho$ is the fraction of volume occupied by polymers instead of solvent molecules (ρ: number density of polymer chains); and χ_{FH} is the Flory–Huggins interaction parameter, equal to one-half of the change in energy when one polymer–polymer contact and one solvent–solvent contact are broken to form two polymer–solvent contacts. Note that a positive χ_{FH} means that polymer–polymer contacts are more attractive than polymer–solvent contacts; this is the case that will be considered below.

Comparing eq 18 for polymer solutions with the counterpart, eq 17b, for the van der Waals model for protein solutions, we see certain resemblance. In particular, χ_{FH} corresponds to the van der Waals parameter a for the magnitude of solute–solute attraction. The (osmotic) pressure here is

$$\beta p = -\left.\frac{\partial \beta \mathcal{F}}{\partial V}\right|_{N,T} \tag{19a}$$

$$= \phi \left.\frac{\partial \beta f}{\partial \phi}\right|_{\beta} - \beta f \tag{19b}$$

$$= \frac{1}{v_1}\left[\frac{\phi}{L} - \phi - \ln(1 - \phi) - \chi_{FH}\beta\phi^2\right] \tag{19c}$$

$$= \rho + \left(\frac{1}{2} - \chi_{FH}\beta\right)v_1 L^2 \rho^2 + \frac{1}{3}v_1^2 L^3 \rho^3 + \frac{1}{4}v_1^3 L^4 \rho^4 + \cdots \tag{19d}$$

This last expression is to be compared with the virial expansion, eq 12b, of the van der Waals model. In both cases, only the second virial coefficient can be negative. For the present case,

$$B_2 = \left(\frac{1}{2} - \chi_{FH}\beta\right)v_1 L^2 \tag{19e}$$

which, when compared with eq 12c, clearly shows that χ_{FH} plays the same role as the van der Waals parameter a. The Boyle temperature is given by

$$\frac{\chi_{FH}}{k_B T_B} = \frac{1}{2} \tag{20}$$

Similar to the van der Waals equation, eq 18 predicts a critical temperature below which two phases coexist (Figure 5a); the two phases differ in polymer concentrations (i.e., different ϕ values). The critical point can be determined by eqs 5a and 5b, i.e., the first and second derivatives of p with respect to V are 0. Because p itself is the first derivative of the Helmholtz free energy (eq 19a), eqs 5a and 5b become conditions on the second and third derivatives of f:

$$\left.\frac{\partial^2 f}{\partial \phi^2}\right|_{T=T_c} = 0 \tag{21a}$$

$$\left.\frac{\partial^3 f}{\partial \phi^3}\right|_{T=T_c} = 0 \tag{21b}$$

The resulting critical point is

$$\frac{\chi_{FH}}{k_B T_c} = \frac{(1 + \sqrt{L})^2}{2L} \tag{22a}$$

$$\phi_c = \frac{1}{1 + \sqrt{L}} \tag{22b}$$

Comparing eq 22a with eq 20, we find

$$T_c = \frac{T_B}{1 + 2L^{-1/2} + L^{-1}} \tag{23}$$

Dignon et al.[172] found a very strong correlation between T_B and T_c for coarse-grained IDP chains; they determined T_B by calculating the second virial coefficient using umbrella-sampling Monte Carlo simulations and determined T_c by calculating the binodal using slab-geometry molecular dynamics simulations.

The equation for the spinodal can be found by setting to 0 the second derivative of f with respect to ϕ (i.e., eq 21a), and is

$$\chi_{FH}\beta = \frac{1}{2L\phi} + \frac{1}{2(1 - \phi)} \tag{24}$$

The binodal has to be found numerically, though Qian et al.[173] have recently found a near-exact analytical solution. Illustrative results for the binodal and spinodal are shown in Figure 5b. Again, only a small portion of the area within the binodal is outside the spinodal.

The Flory–Huggins theory has been extremely important for conceptual understanding of phase separation. As recognized by Flory,[49] quantitatively it has limitations due to the simplifications made to derive the theory, in particular the assumption that a polymer chain can cross itself (instead of self-avoiding). Nevertheless the theory and its extensions have been used to fit experimental data.[173−177] The multicomponent version of the Flory–Huggins theory has been used to study noise buffering[154] and the number of coexisting phases.[178]

A lowest-order correction to the mean-field treatment is random phase approximation (RPA),[179,180] a name that originated from the theory of correlated electrons.[181,182] Chan and co-workers developed a sequence-dependent RPA to model phase separation of IDPs.[183,184] RPA captures the trend of charge-pattern dependence of polyampholyte phase separation, though lattice Monte Carlo simulations[185] and field-theoretic simulations[186] have revealed inaccuracies (e.g., overestimation of the chemical potential at low densities). Lastly we note that Chang et al.[187] have combined the Flory–Huggins mixing entropy with the excess free energy calculated from Monte Carlo simulations to determine the binodals of oppositely charged polyelectrolytes.

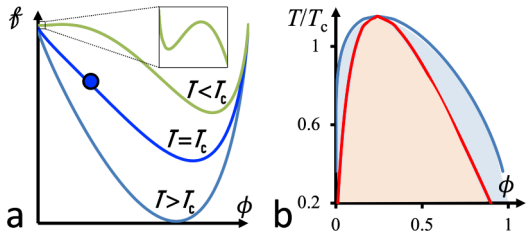

Figure 5. Flory–Huggins theory for polymer solutions. (a) $f - \phi$ isotherms. At $T < T_c$, a local minimum merges at very small ϕ (zoomed region). (b) The binodal (blue curve) and spinodal (red curve).

https://doi.org/10.1021/acs.chemrev.4c00138
Chem. Rev. XXXX, XXX, XXX−XXX

2.5. Interfaces

As alluded to in the Introduction, the interfaces of biomolecular condensates with the bulk phase (Figure 1c) are the place where many of their liquid-like behaviors are manifested, in particular the tendency to minimize the interfacial area. At the interface, the interactions between molecules are different from those in the interior of each homogeneous phase. Hence there is tension at the interface and an expansion in the interfacial area leads to an increase in the energy of the system, just like compression of a fluid would. Indeed, whereas the change in energy resulting from a volume change dV is $-pdV$, the change in energy resulting from an interfacial area change dA is γdA. Thus, the interfacial tension γ, or energy per unit area, is similar to the pressure in many respects. For a one-component system with an interphase interface, the fundamental thermodynamic relation for the internal energy becomes

$$dE = TdS - pdV + \mu dN + \gamma dA \tag{25}$$

A γA term has already appeared in eq 7.

Given that the interface has a finite thickness, spanned by a gradual change in the number density, $\rho(z)$, measured per unit length along the z axis, how can we select a single dividing surface (at $z = z_d$) between the two phases (referred to as I and II; bottom panel of Figure 1c)? Consider a hypothetical state where each phase is homogeneous all the way to the dividing surface. In particular, the number densities are uniform in both phases (as indicated by the dashed lines in bottom panel of Figure 1c), and suffer an abrupt change at $z = z_d$. In this hypothetical state, any extensive thermodynamic property H (= $E, S, V, N, \ldots$) is the sum of its values in the two phases: $H_I + H_{II}$. The difference in H between the real system and the hypothetical state can be attributed to the interface:

$$H_{intf} = H - (H_I + H_{II}) \tag{26}$$

By definition, $V_{intf} = 0$. The number of molecules attributed to the interface can be found as

$$N_{intf} = \int_{-\infty}^{\infty} dz\rho(z) - \int_{-\infty}^{z_d} dz\rho_{II} - \int_{z_d}^{\infty} dz\rho_I \tag{27a}$$

We can choose z_d such that

$$N_{intf} = 0 \tag{27b}$$

resulting in the Gibbs dividing surface. The differential form for the internal energy of the interface is

$$dE_{intf} = TdS_{intf} + \gamma dA \tag{28}$$

For a two-component system, we can use eq 27b on one of the components (say component 1) but not both. The number of component-2 molecules, $N_{2;intf}$, attributed to the interface can be either positive or negative, corresponding to either enrichment or depletion at the interface (relative to the dense phase). Eq 28 is modified to

$$dE_{intf} = TdS_{intf} + \mu_2 dN_{2;intf} + \gamma dA \tag{29a}$$

The fact that all extensive thermodynamic properties are first-order homogeneous functions implies

$$E_{intf} = TS_{intf} + \mu_2 N_{2;intf} + \gamma A \tag{29b}$$

Using eq 29b in eq 29a, we obtain

$$S_{intf} dT + N_{2;intf} d\mu_2 + Ad\gamma = 0 \tag{29c}$$

which can be seen as a generalization of the Gibbs–Duhem eq (eq 14a). Under constant temperature, the last equation leads to

$$\left.\frac{\partial \gamma}{\partial \rho_{2,II}}\right|_T = -\frac{N_{2;intf}}{A}\left.\frac{\partial \mu_2}{\partial \rho_{2,II}}\right|_T \tag{30}$$

Note that for any thermodynamically stable state,

$$\left.\frac{\partial \mu}{\partial \rho}\right|_T > 0 \tag{31}$$

similar to the condition $\left.\frac{\partial p}{\partial V}\right|_T < 0$ (see Subsections 2.2.1 and 3.1.1). Therefore, according to eq 30, the presence of a component-2 that is enriched at the interface (i.e., $N_{2;intf} > 0$) will decrease the interfacial tension. This is just the mechanism for surfactants (e.g., soap): their enrichment at the water–air interface reduces the surface tension, allowing the surface to stretch more easily. Conversely, depletion of an additive results in an increase in the surface tension of water; salts are such examples.

2.6. Viscous Flows

The flow of liquids is governed by the Navier–Stokes eqs (Supporting Information Section S1), which model the liquids as viscous (with viscosity η; see Subsection 4.3.1). The solution of this equation is the velocity field $\mathbf{v}(\mathbf{x},t)$, comprising the velocity at all positions (represented by $\mathbf{x}$) of the liquid at time t.

2.6.1. Time-Dependent Shear Flow. In the shear flow illustrated in Figure 2a, the flow velocity (v_x, along the x axis) and its gradient ($\partial v_x/\partial y$, along the y axis) are perpendicular to each other. The Navier–Stokes equations then simplify to (Supporting Information eq S147)

$$\frac{\partial v_x(y,t)}{\partial t} = \frac{\eta}{\varrho}\frac{\partial^2 v_x(y,t)}{\partial y^2} \tag{32}$$

where ϱ is the mass density (= $m\rho$, with m denoting molecular mass and ρ denoting number density). This equation has exactly the same form as the diffusion equation, and is used in Supporting Information Subsection S7.2 to derive the microscopic formulation of the viscosity.

If a thin layer in the middle of the liquid is forced to flow in the x direction at time $t = 0$, then neighboring layers will also flow in the same direction (Figure 6a). The magnitudes of the flow velocities decrease as the layers are farther positioned from the initial layer; the overall velocity profile is a Gaussian function as predicted by eq 32.

2.6.2. Steady Shear Flow. As depicted in Figure 2a, for a liquid confined between two plates, when the top plate is moving

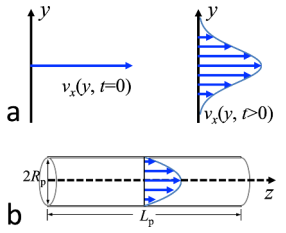

Figure 6. Viscous flows. (a) A boundless shear flow. A flow velocity in the x direction is generated in a small bin around $y = 0$ at time 0 (left panel). Over time, the velocity field spreads to other y values (right panel). (b) A Poiseuille flow. Arrowed lines indicate velocity fields.

https://doi.org/10.1021/acs.chemrev.4c00138
Chem. Rev. XXXX, XXX, XXX−XXX

at a constant velocity U, a steady flow field will be established. Because there is no dependence on time, eq 32 reduces to

$$\frac{\partial^2 v_x(y)}{\partial y^2} = 0 \tag{33}$$

The velocity gradient is a constant

$$\frac{\partial v_x(y)}{\partial y} = \frac{U}{L} \tag{34a}$$

where L is the separation between the two plates. Such a velocity gradient will be used in Subsection 4.3.1 to explain viscosity. The resulting velocity field is a linear function,

$$v_x = \frac{U}{L} y \tag{34b}$$

displayed by a set of arrowed lines in Figure 2a.

2.6.3. Poiseuille Flow. Another type of flow, relevant to a method for measuring viscosity[188] (Subsection 4.3.5), is driven by a constant pressure gradient, $\Delta p/L_p$, across a long circular pipe (Figure 6b). For this Poiseuille flow, the Navier−Stokes equations become (Supporting Information eq S8)

$$\frac{1}{s}\frac{\partial}{\partial s}\left(s\frac{\partial v_z}{\partial s}\right) = -\frac{1}{\eta}\frac{\Delta p}{L_p} \tag{35}$$

where s denotes the axial distance. The velocity profile is given by

$$v_z = \frac{1}{4\eta}\frac{\Delta p}{L_p}(R_p{}^2 - s^2) \tag{36a}$$

where R_p is the radius of the pipe. The average over the cross section is

$$\overline{v_z} = \frac{R_p{}^2}{8\eta}\frac{\Delta p}{L_p} \tag{36b}$$

3. PHASE EQUILIBRIUM PROPERTIES

This section focuses on factors that affect the equilibrium between bimolecular condensates and the surrounding bulk (or dilute) phase. We first summarize various methods that have been developed or applied to compute binodals. We then delve into how global factors including temperature, salts, and pH affect the phase equilibrium, highlight recent progress in predicting the sequence dependence of IDP phase-separation threshold concentration, and present general rules on how intermolecular interaction strengths govern multicomponent phase separation.

3.1. Computational Methods

Phase equilibria are determined by eqs 1a−1c, i.e., equalities in temperature, pressure, and chemical potential between the two coexisting phases. Any method that computes the phase equilibrium must satisfy these equalities. Below we explain how each method achieves these equalities and note other important details. In all cases the system is maintained at constant temperature, thereby guaranteeing the equality in temperature between the phases; hence this equality will not be elaborated further. Implementations of the first three methods are illustrated in ref 189.

3.1.1. FMAP-Based Chemical Potential Calculation. In Subsection 2.2 we mentioned that the phase equilibrium can be determined by a Maxwell-type equal-area construction over $\mu - \rho$ isotherms. We will demonstrate this point shortly, but first we want to describe the FMAP for calculating chemical potentials.[157] FMAP stands for fast Fourier transform-based modeling of atomistic protein−protein interactions. It is rooted in Widom's formulation of the excess chemical potential (see eq 15c):[190]

$$e^{-\beta\mu^{ex}} = \langle e^{-\beta U_I}\rangle_{N,V,T} \tag{37}$$

where U_I is the interaction energy of a test molecule with a system of N molecules at constant volume V and constant temperature T − i.e., in a canonical ensemble, and $\langle\cdots\rangle_{N,V,T}$ signifies averaging over a canonical ensemble of system configurations and over a uniform distribution of the locations where the test molecule is to be inserted (Figure 7a). The key idea behind FMAP is to express the interaction energy U_I (or each of its terms) as a correlation function and then evaluate the latter via fast Fourier transform.

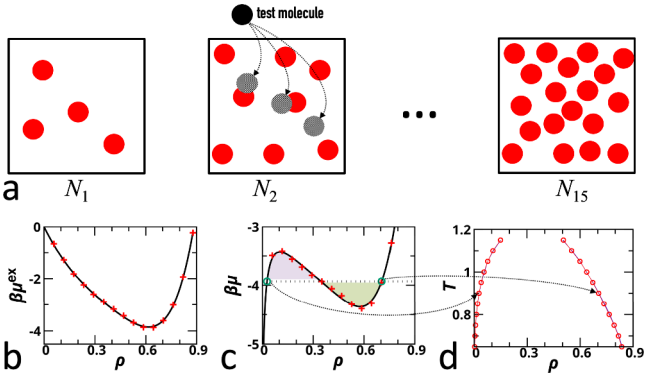

Figure 7. Binodal determination by FMAP-based chemical potential calculation. (a) FMAP calculation over a range of densities. (b) Excess chemical ("+" symbols) and its fit to a polynomial (curve). (c) The full chemical potential and equal-area construction. Circles indicate binodal densities. (d) The binodal. Adapted from ref 189 with permission. Copyright 2023 the original authors.

To generate a $\mu - \rho$ isotherm, μ calculations are carried out for a range of number densities, obtained by preparing systems with different numbers of molecules (N_1, N_2, . . .) in the same volume (Figure 7a). Once μ^{ex} is calculated at these different densities, its dependence on ρ is fit to a fifth-order polynomial (see eq 15b; Figure 7b). The ideal part of the chemical potential is then added in (eq 15c; Figure 7c). Normally, μ is a monotonically increasing function of ρ, but when two phases can coexist, a nonmonotonic portion appears, similar to the van der Waals loop shown in Figure 4c. We can thus carry out an equal-area construction (Figure 7c), similar to the Maxwell construction for a $p - V$ isotherm (Figure 4c). Here, the horizontal line bisecting the $\mu - \rho$ isotherm ensures the two stable phases (referred to as I and II), identified by the inner and outer intersection points of the horizontal line and the $\mu - \rho$ curve, have the same chemical potential. The equal-area requirement last fulfills the condition of equality in pressure. To see this point, we integrate both sides of eq 14b to obtain

$$p_{II} - p_I = \int_I^{II} \rho \mathrm{d}\mu \tag{38}$$

https://doi.org/10.1021/acs.chemrev.4c00138
Chem. Rev. XXXX, XXX, XXX−XXX

which can be seen as the difference between the enclosed areas above and below the horizontal line and is thus 0 under the equal-area condition.

We note that field-theoretic simulations have been used to calculate the chemical potentials of IDPs modeled as polymer chains.[186] In field-theoretic simulations, one works not with particles but with a chemical potential field.[191]

The ρ_I and ρ_{II} values determined at a series of temperatures are finally plotted as a binodal (Figure 7d). To determine the critical point, one can simultaneously fit the mean of ρ_I and ρ_{II} to the law of rectilinear diameter[192]

$$\frac{\rho_I + \rho_{II}}{2} = \rho_c + A(T - T_c) \tag{39a}$$

and the difference in density to a scaling law

$$\frac{\rho_{II} - \rho_I}{2} = B(T_c - T)^{\alpha_1} \tag{39b}$$

where A and B are fitting parameters and α_1 is known as a critical exponent in the physics literature. For phase separation, gas−liquid transition, and other phase transitions of the same universal class, $\alpha_1 \approx 0.32$.

By collecting the local maximum and local minimum of the van der Waals loop, one can also obtain the spinodal, similar to what is described for the van der Waals model (Subsection 2.2) and the Flory−Huggins theory for polymer solutions (Subsection 2.4).

FMAP was also implemented to calculate the second virial coefficient (B_2 in Subsection 2.3) and the cross second virial coefficient B_{23}, which extends B_2 to the interaction between two different solute components.[139,193] Consistent with the predictions of simple theoretical models (Subsections 2.2 and 2.4), a decrease in B_2 was found to correspond to an increase in T_c for γ-crystallins modeled at the all-atom level.[194]

3.1.2. Gibbs Ensemble Simulations. Panagiotopoulos[195] introduced a method where two separate simulation boxes, initially identical (Figure 8a), evolve to become two phases that differ in density and are at equilibrium with each other (Figure 8b, c). The evolution involves exchanges of volumes and molecules between the two boxes, which are designed to achieve equalities in pressure and chemical potential, respectively. The densities of the two boxes can then be used to build the binodal (Figure 8d). The combined system, with the total molecule number and total volume fixed, is said to be in a Gibbs ensemble.

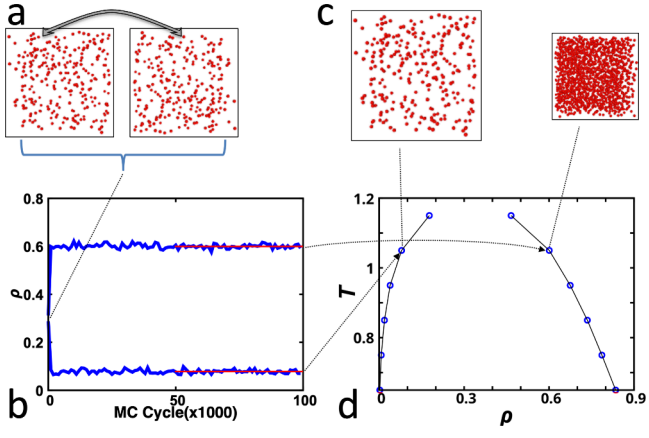

Figure 8. Gibbs ensemble simulation. (a) Two identical boxes at the start. (b) Densities of the two boxes monitored in a Monte Carlo simulation. Red lines indicate average densities calculated over the second half of the simulation. (c) The final snapshot of the simulation. (d) The binodal. Adapted from ref 189 with permission. Copyright 2023 the original authors.

Exchanges in volumes and molecules between the two boxes as well as molecule movements within each box were originally implemented through Monte Carlo procedures. An interesting recent development is the implementation by field-theoretic simulations.[186,196] In Gibbs ensemble simulations of polymer systems by Monte Carlo, insertion of polymer chains into a dense box, a step necessary for implementing molecule exchange, has a very low success rate, leading to the omission of the exchange of polymer chains.[197,198] Field-theoretic simulations enable such exchanges.[186]

3.1.3. Slab-Geometry Simulations. A binodal calculation method that has an even longer history than the Gibbs ensemble and is the most widely used for modeling biomolecular condensates is slab-geometry simulation (Figure 9). The earliest report of such a simulation that we are aware of is by Rao et al. in 1976 for the gas−liquid coexistence of a Lennard-Jones fluid.[199] In a typical implementation, one starts with a very dense slab at the center of a long simulation box (Figure 9a). Molecules then move out of the dense slab and eventually reach equilibrium between a dense phase at the center and a dilute phase on the two sides. Because of the free exchange of molecules between them, the two phases naturally reach equalities in pressure and chemical potential. The densities in different bins along the long axis (taken as the z axis) are then calculated and are fit to a function like (Figure 9b)

$$\rho(z) = \frac{\rho_I + \rho_{II}}{2} + \frac{\rho_I - \rho_{II}}{2} \tanh \frac{z - z_d}{d} \tag{40}$$

to obtain the densities ρ_I and ρ_{II} in the two phases as well as the position z_d of the dividing surface and the width d of the interface.

Slab-geometry simulations are unique in that they produce two phases that coexist side by side, separated by two planar interfaces. The presence of these interfaces allows the calculation of the interfacial tension (see Subsection 4.2.1).

3.1.4. SpiDec Simulations. The initial dense slab in slab-geometry simulations may be difficult to prepare and also hinders the exchange of molecules with the dilute phase (see next subsection). Mazarakos et al.[147] recently developed a variation dubbed SpiDec, exploiting the idea that a molecular system started at an intermediate density that is inside the spinodal should spontaneously and quickly phase separate. In line with other studies,[200] their coarse-grained simulations inside the spinodal have shown that the systems form dense spheres or cylinders when started very close to the low-density arm of the spinodal, and form hollow cylinders or spheres when started very close to the high-density arm of the spinodal (Figure 10a). However, in a wide swath at the center of the spinodal, the systems form slabs, which can be used to build binodals.

These simulations also revealed the details of the spinodal decomposition process. Starting from a homogeneous state, density fluctuations instantaneously lead to dense regions and voids (Figure 10b, first panel). Neighboring dense regions quickly condense to form domains that often are connected to other domains (Figure 10b, second panel). The domains further condense, typically into a single slab in a cubic box. Interestingly, in an elongated box, the necks between domains can break, producing separate slabs (Figure 10b, third panel). Finally, the slabs slowly fuse into a single slab (Figure 10b, last panel).

https://doi.org/10.1021/acs.chemrev.4c00138
Chem. Rev. XXXX, XXX, XXX−XXX

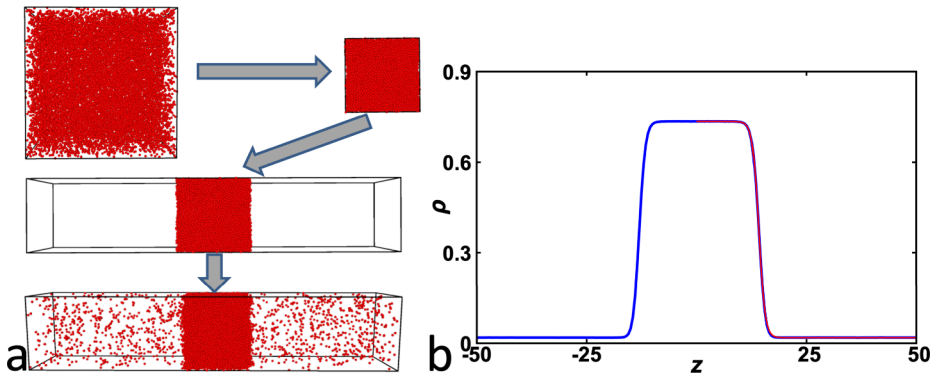

Figure 9. Slab-geometry simulation. (a) A typical setup. (b) Density profile (blue curve) and its fit (red curve) to eq 40. Adapted from ref 189 with permission. Copyright 2023 the original authors.

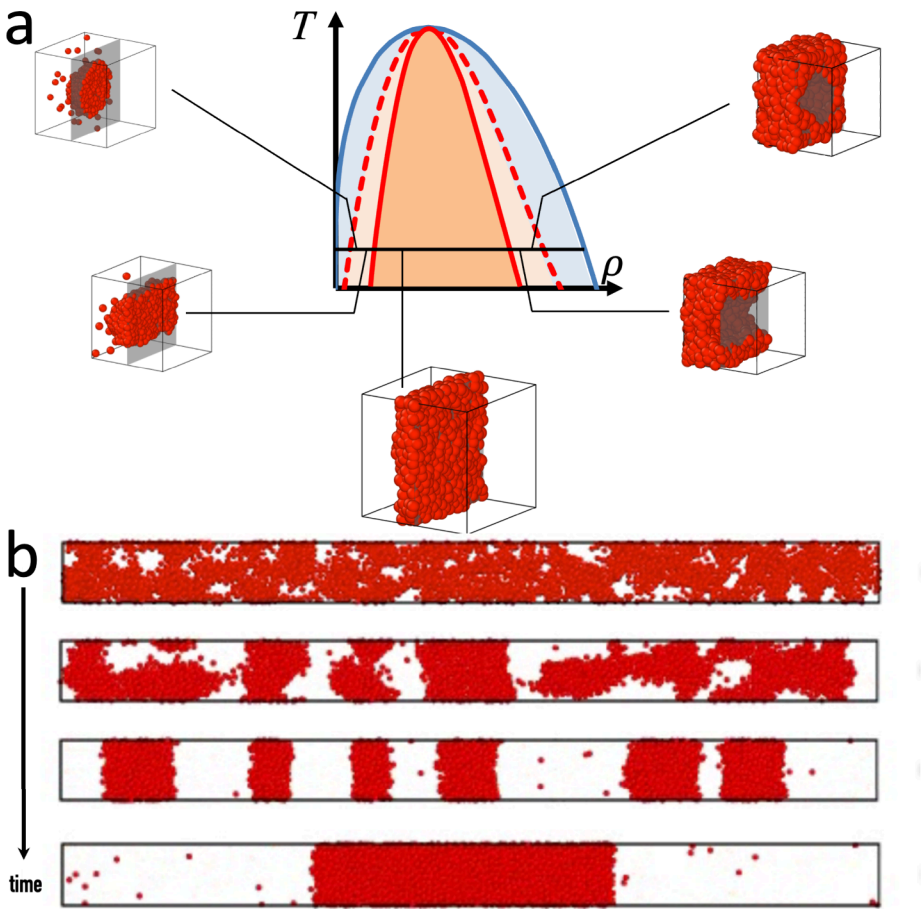

Figure 10. Spinodal decomposition and its use for starting simulations to calculate binodals. (a) A variety of condensate morphologies when simulations are started inside the spinodal. In each image, the cubic box is cut by a plane (appearing as gray in an empty background) and the half behind the cut is displayed. (b) Details of the spinodal decomposition process. Images of molecular systems are from ref 147. Copyright 2022 the original authors.

3.1.5. Levels of Representation of Biomolecular Systems in Simulations. The foregoing methods can all work with a coarse-grained representation of solute molecules with solvent treated implicitly. Many slab-geometry simulations at the coarse-grained level have been carried out for biomolecular condensates.[84,85,137,168,172,201−248] FMAP has been used to calculate binodals for proteins represented at the all-atom level, albeit with the proteins treated as rigid and the solvent treated implicitly.[157,194] Zhang et al.[249] have developed a hybrid model for proteins, where the backbone is represented at the all-atom level whereas side chains are at the coarse-grained level, and the solvent is treated implicitly. They reached phase equilibrium in two ways. In one, similar in spirit to SpiDec, they started under a dilute condition to form a dense sphere (Figure 10a); in the second, similar in spirit to slab-geometry, they started from a compacted region to reach equilibrium with the dilute phase.

Zheng et al.[250] attempted to migrate slab-geometry simulations from a coarse-grained model to an all-atom representation of IDPs in explicit solvent. The systems were

https://doi.org/10.1021/acs.chemrev.4c00138
Chem. Rev. XXXX, XXX, XXX−XXX

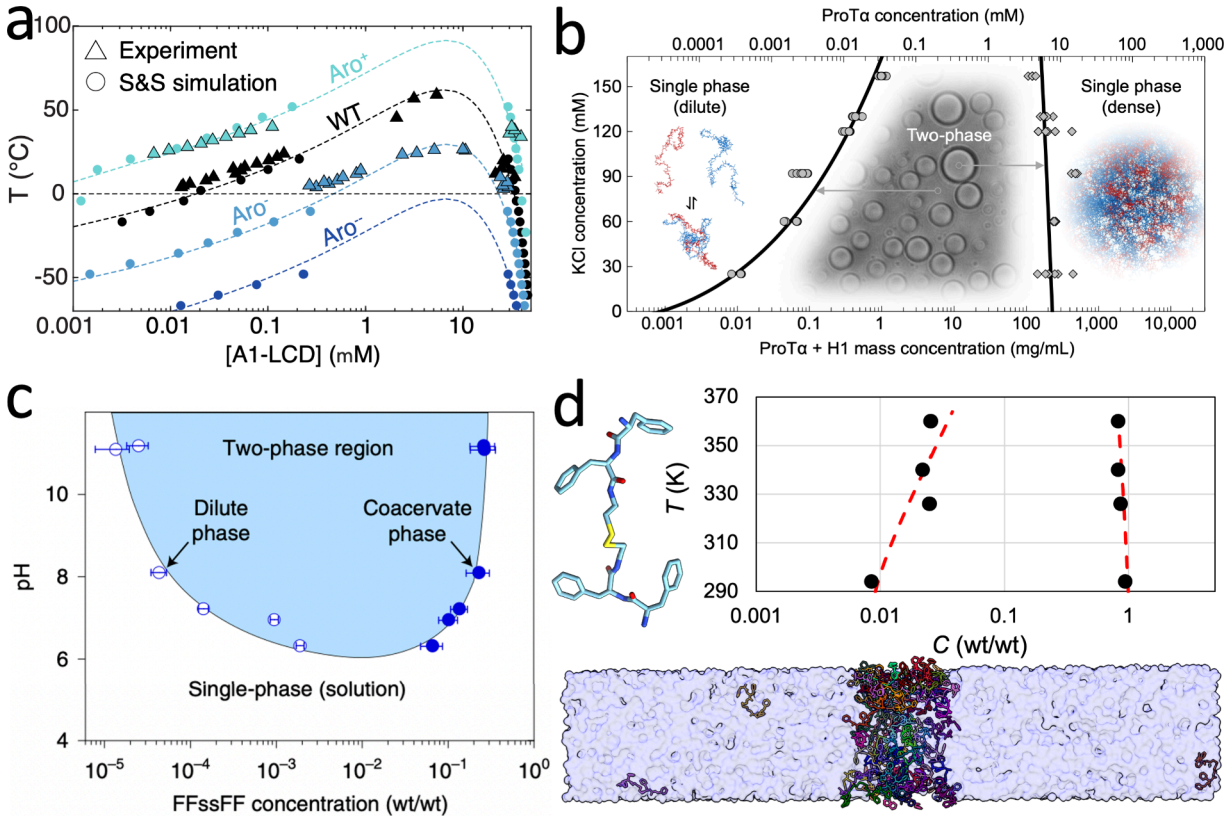

Figure 11. Effects of temperature, salt, and pH on the phase equilibria of IDPs. (a) Binodals of A1-LCD and variants with increased (Aro^+) or decreased (Aro^- and $Aro^{-\,-}$) aromatic contents. Reproduced from ref 176 with permission. Copyright 2020 The American Association for the Advancement of Science. (b) Coexistence concentrations of H1-ProTα mixtures as a function of salt concentration. Reproduced from ref 177 with permission. Copyright 2023 Springer Nature. (c) Coexistence concentrations of FFssFF as a function of pH. A 0.1 wt/wt concentration is approximately 100 mg/mL. Reproduced from ref 253 with permission. Copyright 2021 Springer Nature. (d) Binodal calculated from all-atom simulations. The force fields were the general Amber force field (GAFF)[256] plus partial charges from a Gaussian calculation for the peptide and TIP3P[257] for water. Reproduced from ref 147. Copyright 2022 the original authors.

prepared by replacing coarse-grained chains in a dense slab with all-atom ones. In their simulations, protein chains in the dense phase failed to move to the dilute phase. Similarly, Welsh et al.[251] replaced coarse-grained IDP and RNA chains with all-atom ones, in a phase-separated configuration from coarse-grained slab-geometry simulations. Again, the all-atom chains did not appear to exchange between the phases in the simulations. Therefore, no binodals were obtained from the all-atom simulations in either of these studies. For a recent review of related work, see ref 252.

Using SpiDec, Mazarakos et al.[147] finally succeeded in achieving phase equilibrium in all-atom simulations and calculating the binodal for a tetrapeptide that was observed to phase separate (Figure 11d below).[253] The simulations were prepared with 64 copies of the peptide randomly solvated in a cubic box. To span a range of initial concentrations, different numbers of water molecules were removed and each system was equilibrated at constant temperature and pressure. For some initial concentrations, they observed slab formation in 5 to 10 μs of simulations, similar to coarse-grained simulations (Figure 10a). The simulations then continued in an elongated box at constant temperature and volume to produce phase equilibration. Around the same time, De Sancho reported spontaneous slab formation for all-atom simulations of single amino acids.[254]

Similar to a SpiDec setup, Galvanetto et al.[177] carried out all-atom simulations of two oppositely charged IDPs, histone 1 (H1) and prothymosin-α (ProTα), at copy numbers of 80 and 96, respectively, with random initial placement. They observed slab formation in the simulations. Kota et al.[135] used SpiDec-based all-atom simulations to characterize the condensate formed by mixing a small basic IDP (bIDP) called protamine with ATP. In neither of these last two studies the solute molecules in the dense slab exchanged with the dilute phase in the available simulation time. Polyansky et al.[255] also started all-atom simulations of 24 copies of the N-terminal disordered fragment of Lge1 with random initial placement, but observed a percolating cluster instead of a slab. Such clusters likely correspond to amorphous aggregates (Figure 2c, d) instead of liquid droplets.

3.2. Effects of Temperature, Salts, pH, and Pressure

The basic principle from the theoretical models in Subsections 2.2−2.4 and the computational results from the methods outlined in Subsection 3.1 is that intermolecular attraction drives phase separation, and changes that strengthen the attraction thus in general promote phase separation. Subsections 3.2−3.4 will illustrate how this principle is at work in actual biomolecular condensates. First let us look at how the phase equilibrium is affected by global factors, which act everywhere in the (phase-separated) macromolecular solution.

3.2.1. IDPs. In statistical thermodynamics, the Boltzmann factor $\exp(-\varphi/k_BT)$ of the interaction energy φ determines the probabilities of states. Intermolecular attraction is thus scaled by the absolute temperature (see, e.g., eqs 11b and 19e); raising the

https://doi.org/10.1021/acs.chemrev.4c00138
Chem. Rev. XXXX, XXX, XXX−XXX

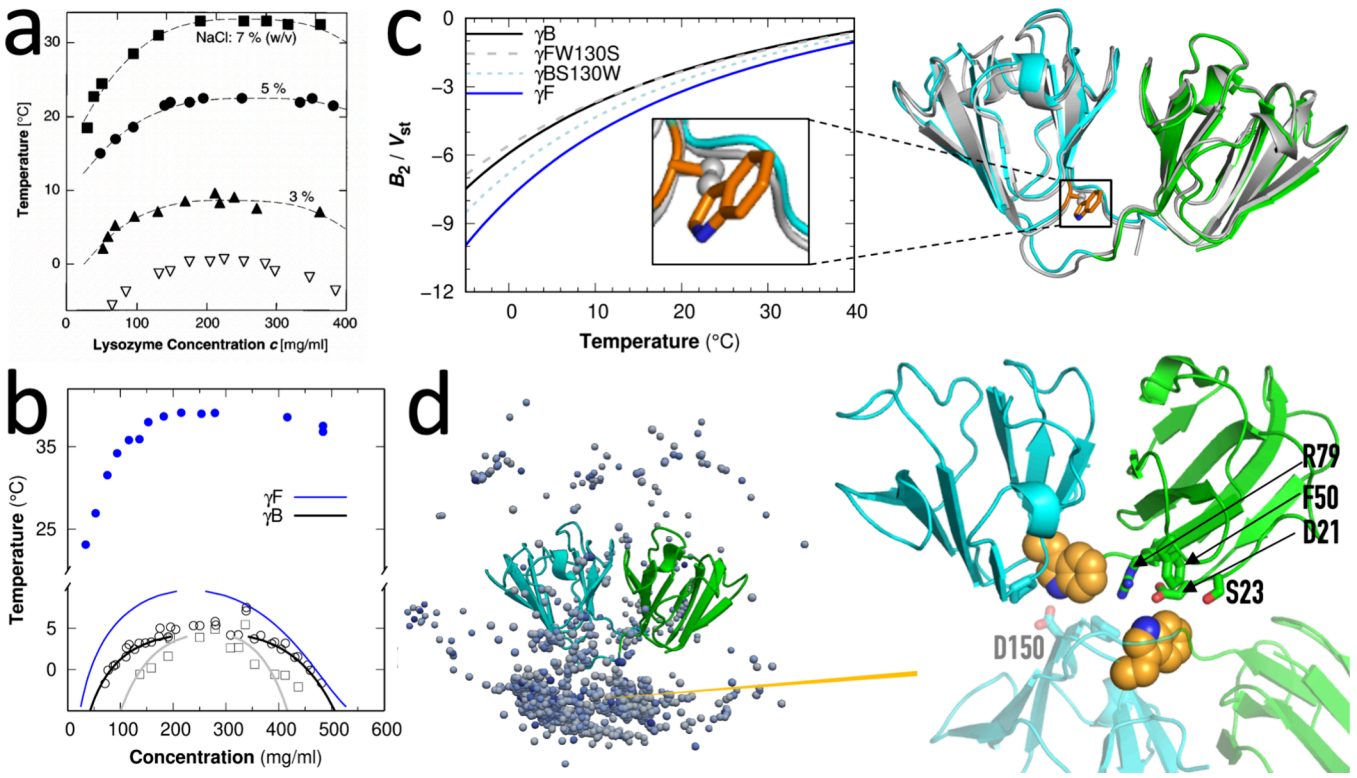

Figure 12. Effects of salt and temperature on the phase equilibria of folded proteins. (a) Binodals of lysozyme at pH 4.5 in 100 mM NaAc buffer and indicated NaCl concentrations (filled symbols) or at pH 6.0 in 600 mM sodium phosphate (open symbols[277]). 5% w/v NaCl is 856 mM. Reproduced from ref 264 with permission. Copyright 1997 AIP Publishing. (b) Binodals of bovine γ-crystallins, with experimental data (symbols) from refs 53 and 55 and FMAP results (curves) from ref 194. For γB, circles and black curve display the binodal whereas squares and gray curve displays the spinodal. (c) Right: structures of γB (gray) and γF (cyan and green);[276] left: calculated second virial coefficients of γB, γF, and two point mutants. (d) Left: configurations of 1000 lowest interaction energy binary poses for γF; right: interface of one such binary complex. Panels (b–d) are adapted from ref 194. Copyright 2023 the original authors.

temperature has the same effect as weakening the attraction. That is why the binodal becomes narrower as the temperature is raised, eventually to a point at the critical temperature. Figure 11a presents the binodals of the hnRNPA1 low-complexity domain (A1-LCD) and two variants measured by Martin et al.[176] The data fit well to an extended Flory–Huggins theory. Moreover, the authors calculated the binodals from lattice Monte Carlo simulations, with the IDPs represented by a stickers-and-spacers ("S&S") model where aromatic residues were assumed to be stickers and all other residues as spacers; the strengths of attraction progressively weakened from sticker–sticker to sticker-spacer to space–spacer pairs. Phase equilibrium was achieved by forming a dense sphere with the simulations started under a dilute condition (Figure 10a). The S&S simulations predicted an increase or decrease in T_c by adding or reducing the content of aromatic restudies, and these predictions were validated by experimental measurements. Binodals of other IDPs have also been measured.[174]

The A1-LCD results highlight the importance of $\pi-\pi$ interactions between aromatic residues in driving phase separation. Other attractive interactions in biomolecular systems include hydrophobic interactions, cation- and amino-π interactions, hydrogen bonds, and interactions between opposite charges. The latter attraction can be easily weakened by adding salts such as KCl. Therefore, the dependence of the coexistence concentrations on salt concentration is qualitative similar to a binodal. Figure 11b presents such a salt dependence for H1-ProTα mixtures at a 1:1.2 molar ratio.[177] At neutral pH, H1 and ProTα carry net charges of +53e and −44e, respectively, and therefore experience very strong charge–charge attraction. Raising KCl concentration from 25 mM to 157 mM has an enormous effect on the phase equilibrium, increasing the threshold concentration of ProTα for phase separation by 100-fold, from 0.35 μM to 35 μM, while marginally affecting the ProTα concentration in the dense phase. Similar increases in C_{th} with increasing NaCl have been observed for many other IDPs.[12,60,65,78,174,175,258,259] In contrast, A1-LCD,[259] TDP-43 LCD,[260] a prion protein variant,[261] resilin-like peptides,[262] histidine-rich beak protein 2 (HBP-2),[263] and the folded protein lysozyme (Figure 12a)[264] all show a decrease in C_{th} with increasing NaCl concentration. This reverse trend is likely related to the high net positive charges of these proteins; in essence, charge neutralization by anion binding abrogates net-charge repulsion, leaving other attractive interactions (e.g., $\pi-\pi$) to drive phase separation.

In addition to screening charge–charge interactions, high salt can exert additional effects including modulating protein–water interfacial tension (Subsection 2.5).[265] Depletion of salt ions from nonpolar residues leads to an increase in interfacial tension and hence a strengthening of hydrophobic interactions. In an interesting study, Krainer et al.[266] found that FUS and several other IDPs phase separate at both low salt (22.5 mM NaCl) and high salt (500 mM NaCl) but not at intermediate salt (225 mM NaCl). They explained the reemergence of phase separation at high salt as due to salt-mediated strengthening of hydrophobic, $\pi-\pi$, and cation-π (specifically Arg-Tyr) interactions, based on

https://doi.org/10.1021/acs.chemrev.4c00138
Chem. Rev. XXXX, XXX, XXX–XXX

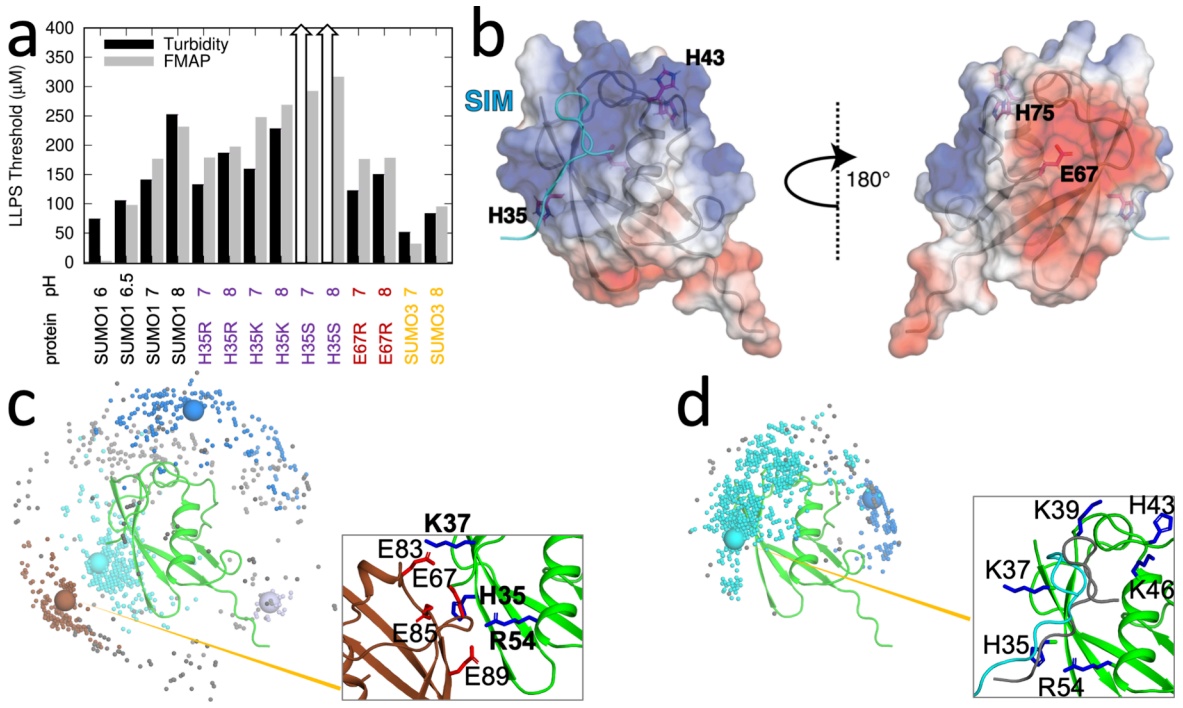

Figure 13. Effects of pH and mutations on the phase equilibrium of polySUMO−polySIM mixtures. (a) Threshold concentrations for SUMO variants at different pH values, either measured based on turbidity or predicted from FMAP-based calculations. For turbidity measurements, the two proteins were mixed at equimolar modules; the threshold concentration refers to the molarity of SUMO modules. (b) Surface electrostatic potential of SUMO1, showing a positive patch between H35 and H43 on one face and a negative patch centered around E67 on the opposite face. (c) 1000 lowest interaction energy configurations of a SUMO1−SUMO1 pair. The interface of one such pair is shown in the zoomed view. (d) 1000 lowest interaction energy configurations of a SUMO1−SIM pair. The interface of one such pair is shown in the zoomed view; the native complex[280] is shown with SIM in gray. Reproduced from ref 279. Copyright 2024 American Chemical Society.

potential of mean force calculations for amino-acid pairs in all-atom molecular dynamics simulations.

The charges on the side chains and the backbone termini can be changed by pH, making pH another global factor for influencing the phase equilibrium. We can expect a pH change that strengthens charge−charge attraction or weakens charge−charge repulsion to promote phase separation. The latter effect was observed by Abbas et al.[253] on a synthetic tetrapeptide formed by linking the C-termini of two copies of diphenylalanine by a disulfide bond, referred to as FFssFF (see structure in Figure 11d). The total charge on the peptide can be +2e when both of the N-termini are protonated (expected at low pH), + 1e when only one of the N-termini is protonated (at intermediate pH), and 0 when both N-termini are deprotonated (at high pH). This peptide started to phase separate around pH 6 (Figure 11c), where most of the chains are singly protonated. By further deprotonating the chains, higher pH promotes phase separation, as indicated by a substantial decrease in C_{th}; the concentration in the dense phase is much less affected by pH. Similar pH effects have been observed in other IDPs including TDP-43 LCD,[260] α-synuclein,[267] and HBP-1.[268]

As noted in Subsection 3.1, FFssFF is the first experimentally observed phase-separating system[253] for which a binodal has been calculated from all-atom explicit-solvent molecular dynamics simulations.[147] This distinction is due in large part to the small size of FFssFF. The binodal (for neutral pH) is shown in Figure 11d, along with a snapshot of the phase-separated configuration. The calculated coexistence concentrations at room temperature are similar to the experimental counterparts, but do overestimate the latter by ∼3-fold in both phases. The low-concentration arm of the binodal shows a higher sensitivity to temperature than the high-concentration arm, qualitatively similar to the experimental observation by varying pH. Recently Zhang et al.[269] reran the simulations using a force field that has been validated for IDPs,[270,271] which brought the coexistence concentrations closer to observed values. Phase equilibrium is exquisitely sensitive to force fields and therefore experimental data like binodals will be very valuable for their parametrization.

3.2.2. Folded Proteins and Proteins Containing Folded Domains. Besides lysozyme (Figure 12a), other folded proteins for which binodals have been determined include γ-crystallins. Starting from nearly four decades ago, it has been known that up to six highly homologous γ-crystallins are expressed in bovine, rat, and human eye lenses, and that they fall into two groups.[52,54−56,272−275] One, represented by bovine γB, has T_c below 10 °C; the other, represented by bovine γF, has T_c around body temperature (Figure 12b).[53,55] The sequences of the two groups are highly homologous and their structures are also very similar; e.g., bovine γB and γF have 82% sequence identity and their crystal structures[276] have a root-mean-square-deviation of only 0.19 Å (Figure 12c). The origin for the large gap in T_c between the two groups of γ-crystallins had remained a mystery, until it was revealed recently by FMAP-based calculations.[194] These calculations predicted well the binodal and spinodal of bovine γB, and a binodal with an increased T_c for γF, though the magnitude of the increase in T_c is clearly underestimated due to the inaccuracy of the interaction energy function and other limitations. The increased T_c arises from stronger attraction among γF molecules, as indicated by chemical potential values that are more negative when compared to γB. The stronger self-attraction of γF is confirmed by a more negative second virial

https://doi.org/10.1021/acs.chemrev.4c00138
Chem. Rev. XXXX, XXX, XXX−XXX

coefficient (Figure 12c). The decomposition of the binary interaction energies into contributions of individual residues finally identified a substitution, from Ser in γB to Trp in γF, at position 130 as a major contributor to the difference in binary interaction energy. This position is located at the foot of the interdomain cleft (Figure 12c), where a second γF molecule preferentially binds (Figure 12d).

In line with the complex effects of salts on the phase separation of IDPs noted above, the effects of salts on the binodal of lysozyme are more complicated than those presented for NaCl in Figure 12a. Taratuta et al.[277] measured the cloud-point temperature, T_{cloud}, at 90 mg/mL lysozyme and increasing NaCl (up to ∼500 mM) in pH 6.8 sodium phosphate buffer. T_{cloud} is the temperature value at which the solution first becomes cloudy, i.e., two phases come into coexistence, when the temperature is decreased. It is the coexistence temperature for a fixed initial protein concentration and can be viewed as a proxy for T_c. An increase in T_{cloud} was observed, similar to Figure 12a. However, the increase was greater when NaCl was replaced by NaBr; the identity of the anion thus plays a major role. The greater increase in T_{cloud} by Br^- can be attributed to its greater tendency to preferentially accumulate at the surface of a positively charged protein like lysozyme.[265] Zhang and Cremer[278] further extended the anion series to include NO_3^-, I^-, SCN^-, and ClO_4^-, with the increases in T_{cloud} going further to higher and higher levels in that order. However, the increases stopped at some intermediate salt concentration (200 to 500 mM). A further increase in salt concentration resulted in a turnover of T_{cloud}, indicating the setting in of another salt effect, namely a decrease in the interfacial tension due to the accumulation of anions at the protein surface (Subsection 2.5). The decrease in the protein−water interfacial tension means that protein surface area-related energies become less of a drive for phase separation. Taratuta et al.[277] also studied the effect of pH on the binodal of lysozyme (the result at pH 6.0 is included in Figure 12a), finding an increase in T_c with increasing pH. Qualitatively, the latter result is consistent with a reduction in net positive charge and hence a weakening of net charge repulsion at a higher pH, similar to the explanation for the effect of pH on the phase separation of the FFssFF peptide.

Even when net charges are close to 0, pH can still have significant effects on phase equilibrium, as recently reported by Kim et al.[279] These authors studied the phase separation of two synthetic modular proteins consisting of five SUMO domains (polySUMO) and 10 SUMO interaction motifs (polySIM), and observed a C_{th} increase from 75 to 300 μM when pH was increased from 6 to 8 (Figure 13a, black bars). The pH effects arose from the deprotonation of three His residues, as confirmed by mutations to a positively charged or neutral amino acid. These effects of pH and mutations were in good quantitative agreement with predictions using FMAP calculations of the second virial coefficient for SUMO and the cross second virial coefficient for SUMO and SIM (Figure 13a, gray bars). The basis of the predictions was that both the SUMO homotypic interaction and the SUMO-SIM heterotypic interaction contribute to the drive for phase separation. The surface charges of SUMO have a polarized distribution (Figure 13b) whereas SIM carries a small net negative charge. FMAP calculations revealed that both the SUMO homotypic interaction (Figure 13c) and the SUMO-SIM heterotypic interaction (Figure 13d) have a significant electrostatic component, and these interactions are weakened when the His residues are deprotonated. The effects of deprotonation are amplified here because the three His residues are part of a positive electrostatic patch on the folded SUMO domain (Figure 13b), which can participate in both the SUMO homotypic interaction and the SUMO-SIM heterotypic interaction. In comparison, pH effects in the phase separation of the IDP HBP-1 involved as many as 19 His residues.[268] Interestingly, a mutation, E67R, designed to moderate the negative electrostatic patch on the SUMO domain decreased C_{th}, especially at pH 8. This mutation weakens SUMO−SUMO attraction but strengthens SUMO-SIM attraction; the observed decrease in C_{th} thus confirms that both types of attraction contribute to the drive for phase separation.

There have been only a limited number of studies into the effects of external pressure on phase separation of proteins, due to the lack of easy access to high-pressure devices.[275,281−285] One recent study was on γ-crystallins.[275] As the external pressure was increased, the coexistence temperature decreased. The explanation is similar to that for pressure-induced protein unfolding,[286] namely the packing of protein molecules in the dense phase creates water-free voids, which are disfavored at high pressure. IDPs presumably have less a chance of creating such voids in the dense phase and therefore one would predict high pressure to have less of an effect. It will be interesting to test this prediction.

3.2.3. Contrast in C_{th} between IDPs and Folded Proteins. A striking difference between the phase equilibrium data of IDPs shown in Figure 11 and the binodals of folded proteins in Figure 12 lies in the threshold concentration, which at room temperature ranges from 0.01 to 1 mg/mL for the IDPs but around 50 mg/mL for the folded proteins. (Mass concentration provides a much fairer comparison across proteins with different sizes than molarity.) As emphasized throughout this review, phase separation is driven by intermolecular attractive interactions. Whereas every residue in an IDP can participate in intermolecular interactions, only surface residues of a folded protein can participate in intermolecular interactions. Moreover, IDPs adopt extended conformations but folded proteins are compact; thus for the same number of molecules in the same volume, intermolecular contacts are much more likely to form for IDPs than for folded proteins (see Figure 16 below). Lastly, IDP molecules can readily adapt to each other to form contact clusters that each involve multiple residues, but contact clusters between folded protein molecules require shape complementarity. For these reasons, an IDP can form many more intermolecular interactions than a folded protein at the same concentration, thus having a low threshold concentration for phase separation.

3.3. Differences Among the 20 Types of Amino Acids in Driving Phase Separation

Ultimately, one would like to predict the phase equilibrium of each protein from its amino acid sequence. As a stepping stone, knowledge is accumulating on the different magnitudes of the 20 types of natural amino acids in contributing to the drive for phase separation. As noted above, Martin et al.[176] identified aromatic residues as stickers in A1-LCD, whose attraction with other stickers is the strongest among all amino-acid pairs. Qin and Zhou[194] also identified a Ser-to-Trp substitution as the major reason for a large increase in T_c between two groups of γ-crystallins (Figure 12b-d). The C_{th} data of Kim et al.[279] shown in Figure 13a further illustrate that substitutions on the surface of a folded protein can significantly perturb the phase equilibrium.

https://doi.org/10.1021/acs.chemrev.4c00138
Chem. Rev. XXXX, XXX, XXX−XXX

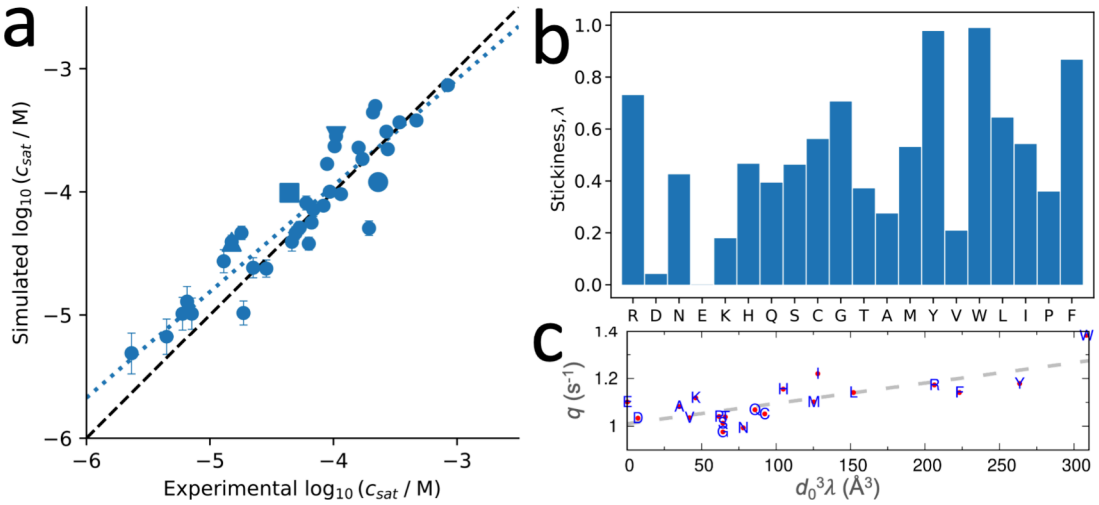

Figure 14. Prediction of phase-separation threshold concentration from coarse-grained simulations and stickiness parameters. (a) Correlation between predicted and measured threshold concentrations (here denoted as C_{sat}). The regression line is shown as dots; the resulting Pearson's correlation coefficient is 0.93. (b) The stickiness parameters. Panels (a) and (b) reproduced from ref 242. Copyright 2023 the original authors. (c) Correlation between the stickiness parameters (λ) and the NMR relaxation parameters (q). The regression line is shown as dashes. Reproduced from ref 292. Copyright 2023 the original authors.

Many other studies have reported C_{th} changes by mutations in IDPs.[255,287−291]

An exciting recent development is that the C_{th} data of IDPs are well predicted by slab-geometry simulations of a coarse-grained model called CALVADOS2 (one particle per residue) Figure 14a).[218,242] Following earlier work,[202] the CALVADOS2 energy function consists of Debye−Hückel potentials for the interactions between charged residues and Lennard-Jones potentials for the interactions between all residues. The relative strengths (ranging from 0 to 1; Figure 14b), or stickiness parameters (λ), of the Lennard-Jones potentials for the 20 types of natural amino acids were tuned against experimental data on radius of gyration and paramagnetic relaxation enhancement for single IDP chains as well as hydrophobicity scales.

Other single-chain data can potentially be used to tune the stickiness parameters. In particular, NMR relaxation data may bring additional information as they are related to IDP dynamics as opposed to conformational properties reported by the radius of gyration and paramagnetic relaxation enhancement. Martin et al.'s identification of aromatic residues as stickers was based in part on elevated transverse relaxation rates.[176] Elevated transverse relaxation rates correspond to slower motions of the backbone amides, which can be caused by transient secondary structure formation or local interactions.[271] Recently Qin and Zhou have developed a sequence-based model to predict the transverse relaxation rates of IDPs. The model includes a relaxation parameter (q) for each type of amino acid type. When the relaxation parameters are compared with the CALVADOS2 values of $d_0^3\lambda$, a combination motivated by eq 21a (d_0: Lennard-Jones diameter), a strong correlation can be recognized, with a Pearson's correlation coefficient of 0.77 (Figure 14c). Both q and $d_0^3\lambda$ rank the bulky amino acids Trp, Tyr, Phe, Arg, and Ile as among the top 6. q actually has a stronger correlation with d_0^3 than with $d_0^3\lambda$; that is, inclusion of λ slightly moderates the correlation with q, due to very low λ values for Glu and Asp. It is possible that both the q and λ parameters are biased by their training data. With accumulating biophysical and C_{th} data on IDPs, we are poised to make better predictions of C_{th} and reach deeper understanding on how amino-acid sequences tune the equilibrium of phase separation.

3.4. Relative Strengths of Intermolecular Interactions in Multicomponent Systems

Membraneless organelles including nucleoli, P granules, and stress granules typically contain dozens to hundreds of macromolecular components.[293−297] It is generally thought that a few major components drive the phase separation.[9−11,82] However, other components have also been shown to regulate the assembly, e.g., of stress granules.[88,104,141] Nguemaha and Zhou[298] studied the effects of macromolecular regulators on the phase equilibrium using Gibbs ensemble simulations of a simple model system, where both the driver and regulator components were represented by hard spheres with attractive patches on the surface. The driver component has self-attraction (strength ϵ_{DD} set to 1) whereas the regulatory component does not (strength ϵ_{RR} set to 0). By varying ϵ_{DR}, the strength of the driver-regulator attraction, a variety of regulatory effects were observed (Figure 15a). At ϵ_{DR} close to 0, where the regulator primarily exerts steric repulsion, or volume exclusion, to the driver, T_c increases with an increasing amount of the regulator, which takes up volume in the bulk phase and thereby indirectly displaces the driver into the dense phase. This effect represents the promotion of phase separation by crowding agents such as PEG and Ficoll reported in numerous studies.

As ϵ_{DR} is elevated but still below ϵ_{DD}, T_c decreases with an increasing amount of the regulator. Here the regulator gets partitioned into the dense phase but once there, it replaces some of the strong driver−driver interactions with weaker driver-regulator interactions. The opposite is observed when ϵ_{DR} is above ϵ_{DD}, but only up to a certain amount of the regulator. As even more of the strong-attraction regulator is added, T_c starts to decrease. This observation captures the so-called reentrant effect of RNA on IDP phase separation reported in many studies.[61,65,67,70,71] The reason for the suppressive effect of a strong-attraction regulator like RNA at a higher amount is very simple: the self-repulsion of the regulator in the dense phase begins to dominate over the driver-regulator attraction.

https://doi.org/10.1021/acs.chemrev.4c00138
Chem. Rev. XXXX, XXX, XXX−XXX

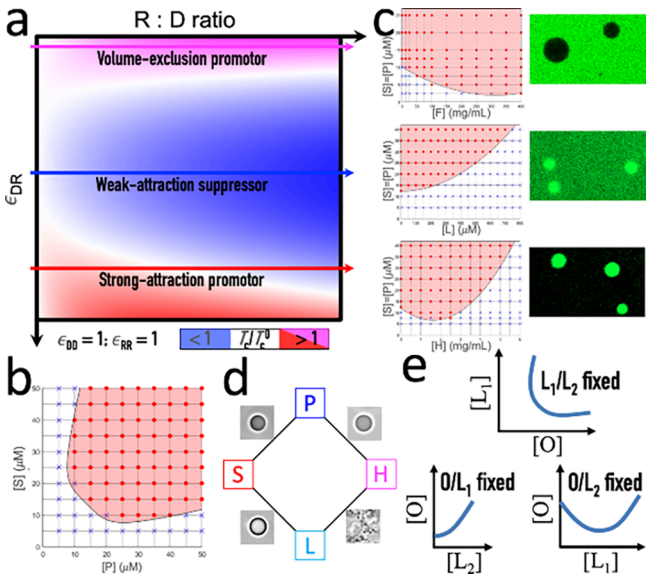

Figure 15. Effects of macromolecular regulators on phase separation. (a) Changes in critical temperature by the presence of different regulators. The ratio of critical temperatures in the presence (T_c) and absence (T_c^0) of a regulator is indicated by a color spectrum ranging from blue to white to red or magenta. (b) Phase boundary of the S−P system. (c) Regulators' effects on S−P C_{th} and partitioning into the dense phase. (d) Condensate formation by all the four binary mixtures with oppositely charged components. (e) Three distinct shapes of phase boundaries. The bottom two phase boundaries are for the case where the O-L_1 attraction is stronger than the O-L_2 attraction. Panels (a−c) adapted from ref 48. Copyright 2019 the original authors. Panel (d) adapted from ref 146. Copyright 2020 American Chemical Society.

To test these ideas and further establish the classification of macromolecular regulators into three archetypes according to the strength of driver-regulator attraction relative to that of driver self-attraction, Ghosh et al.[48] investigated how various macromolecular regulators affected the phase separation of the pentameric constructs of SH3 domains and protein-rich motifs (polySH3 and polyPRM, or "S" and "P" for short) introduced by Li et al.[58] S and P carry net negative and net positive charges, respectively. The phase boundary of the S−P system has the shape of a tilted parabola (Figure 15b), similar to that sketched in Figure 3c. The threshold concentration of the S−P system at equimolar mixing was monitored at increasing amounts of regulators (Figure 15c left panels). Consistent with the expectation for a crowding agent, the S−P C_{th} increased with an increasing amount of Ficoll70. Moreover, confocal imaging of FITC-labeled Ficoll70 indicated that it was largely excluded from the dense phase (Figure 15c top right panel). With lysozyme ("L" for short) as the regulator, a decrease in C_{th} and moderate partitioning into the dense phase were observed (Figure 15c middle row), consistent with the behaviors of weak regulator-driver attraction, presumably with the negatively charged S component. Finally, using the highly negatively charged polymer heparin ("H" for short) as the regulator, a reentrant dependence of C_{th} on H concentration, along with heavy partitioning into the dense phase, was observed (Figure 15c bottom row), likely mediated by strong H−P attraction. These ideas and observations have stimulated further theoretical developments in the regulation of the phase separation of multicomponent systems.[207,299]

Of the four components, S, P, H, and L, two are positively charged and two are negatively charged. They can form six different types of binary mixtures, with two involving like-charged components and four involving oppositely charged components. Phase separation was observed in each of the four oppositely charged binary mixtures (Figure 15d).[146] Three of the condensates appear as liquid droplets and one as reversible aggregates (see also Figure 2c). Relative to droplets, aggregates likely involve stronger intermolecular interactions to make them solid-like. The L:H aggregate could be dissolved by either dilution or adding salt. A related binary mixture, pairing polylysine with H, forms aggregates at low salt but turns into droplets at higher salt.[300] SpiDec-based coarse-grained simulations have shown that, when intermolecular interactions are too strong, spinodal decomposition is arrested and the resulting condensate becomes a gel (Figure 2d),[147] similar to amorphous aggregates found in *in vitro* studies (Figure 2c). These observations demonstrate that, while intermolecular attraction is required for forming droplets, attraction that is too strong turns them into solid-like.

Based on phase boundaries similar to those shown in Figure 15b, c, Ghosh et al.[146] proposed that their shapes can be used to determine the order of interaction strengths among three charged components (Figure 15e). Suppose that two of the components, L_1 and L_2, have like charges, and the third component, O, has an opposite charge. By fixing the molar ratio of two of the components at a time, three phase boundaries with distinct shapes will be produced. The phase boundary with a fixed L_1/L_2 ratio will have the shape of a tilted parabola, similar to what is shown in Figure 15b. The phase boundary with a fixed O/L_1 ratio will have either a half parabola or an upward parabola shape, similar to that shown in Figure 15c second or third row, depending on whether the O-L_1 attraction or the O-L_2 attraction is stronger. Using the foregoing rule, the L-H interaction was found to be the strongest among all the four oppositely charge pairs in Figure 15d, thereby explaining why the L:H mixture formed aggregated whereas the other three binary mixtures formed droplets. Relative strengths of intermolecular interactions can be quantified by the second virial coefficient and the cross second virial coefficient.[139]

4. MOLECULAR AND MATERIAL PROPERTIES

This section opens with the current molecular dynamic picture inside condensates and goes on to delineate the determinants of condensate material properties.

4.1. Molecular Networks and Dynamics in Condensates

All-atom simulations are starting to reveal the details of the extensive interaction networks inside condensates (refs 135, 147, 169, 177, 251, and 255). In the simulations of the H1-ProTα condensate by Galvanetto et al.,[177] each H1 chain interacts with eight ProTα chains and each ProTα chain interacts with six H1 chains on average (Figure 16a). The diffusion constant of a ProTα chain is ∼7 Å^2/ns when in the form of a dimer with H1 in a dilute solution, and reduces to ∼0.2 Å^2/ns inside the condensate. This is a significant reduction but an order of magnitude less than expected from the difference in viscosity between the dense and bulk phases (see Figure 23a below). Moreover, the chain reconfiguration time of ProTα in the dense phase is only 4-fold longer than in the dimer. The reason is that, while IDP chains have strong tendencies to form interchain contacts, these contacts switch partners very rapidly (on the 1 ns time scale), a situation not different from hydrogen bonds between water molecules in the liquid state. Importantly,

https://doi.org/10.1021/acs.chemrev.4c00138
Chem. Rev. XXXX, XXX, XXX−XXX

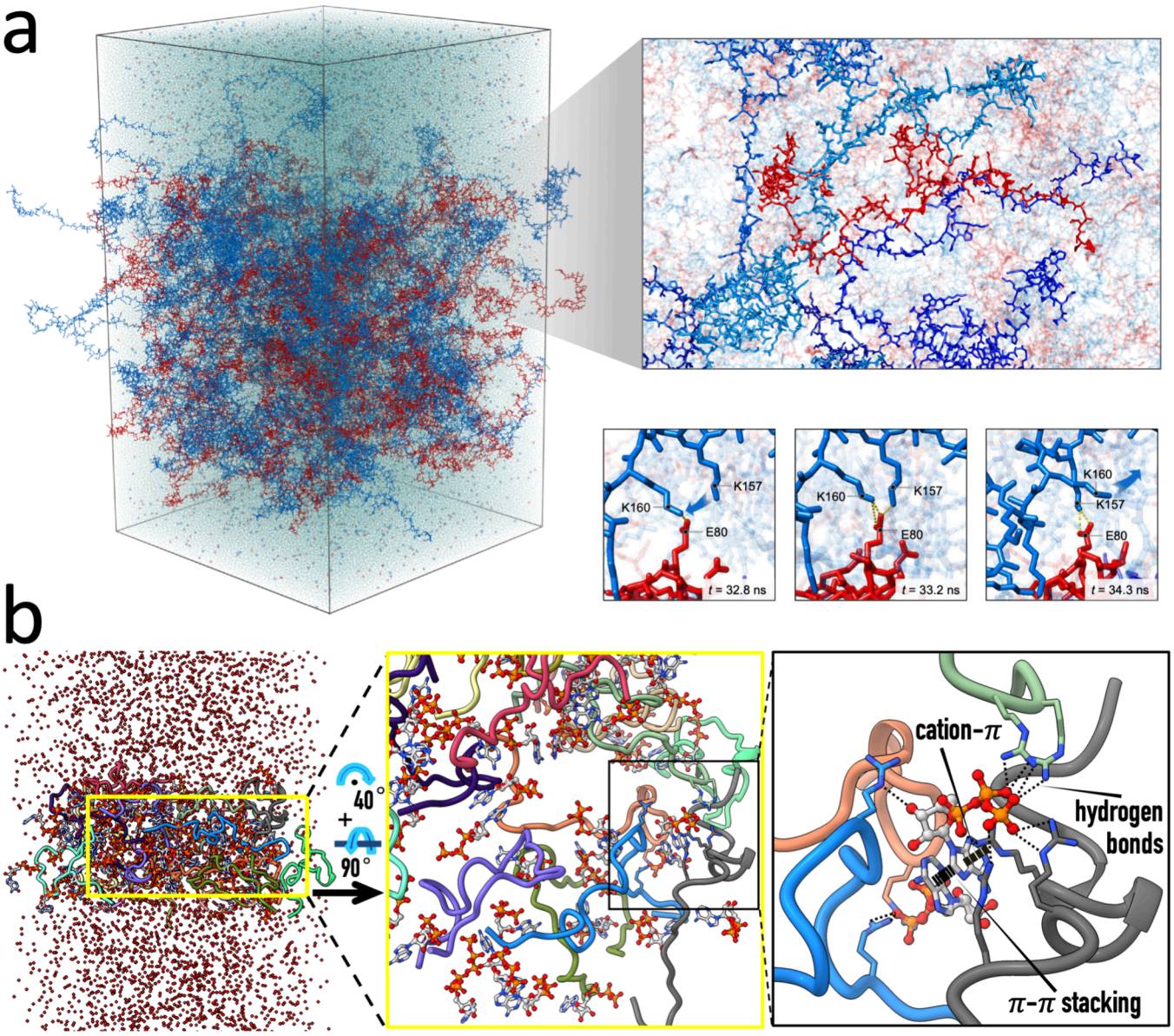

Figure 16. Interaction networks inside condensates revealed by all-atom molecular dynamics simulations. (a) H1-ProTα condensate. The bottom right panel highlights the rapid exchange of salt bridge partners. Reproduced from ref 177 with permission. Copyright 2023 Springer Nature. (b) Protamine-ATP condensate. The rightmost panel highlights extensive interactions between Arg side chains and ATP molecules, including multilayered $\pi-\pi$ and cation$-\pi$ stacks, additional cation$-\pi$ interactions, and hydrogen bonds. Reproduced from ref 135. Copyright 2024 American Chemical Society.

these calculated dynamic properties agree well with their measured values by fluorescence correlation spectroscopy.

A similar situation was found in the all-atom simulations of a condensate formed by mixing ATP with protamine, a 33-residue IDP containing 21 Arg residues (Figure 16b).[135] ATP bridges protamine chains, forming contacts with 2.5 chains on average, via extensive interactions between Arg side chains and all parts of ATP molecules, including multilayered cation$-\pi$ and $\pi-\pi$ and stacks. Each protamine chain forms contacts with 13.2 ATP molecules on average. The diffusion constant of a protamine chain is 2.1 Å^2/ns when bound with 9.6 ATP molecules in a dilute solution and reduces to 0.28 Å^2/ns inside the condensate. As will be further explained below (Subsections 4.3 and 4.4), the protamine-ATP condensate is extremely viscous, with a viscosity that is over 4 orders of magnitude higher than a dilute phase. Yet their fusion is very fast, implicating extreme shear thinning. Kota et al.[135] proposed that the fast fusion is made possible by rapid reformation of ATP bridges between the protamine chains during the fusion process (Subsection 4.4.3).

4.2. Interfacial Tension

As stated in Subsection 2.5, the interfacial tension is the energy per unit interfacial area. The increase in energy resulting from creating interfaces can be illustrated by the work required when an infinite body of liquid is sliced by a plane and pulled apart, thus creating two infinite planar liquid-vacuum interfaces (Figure 17a). A crude calculation, attributed to Laplace,[301] gives the following estimate for the interfacial tension, i.e., work per unit area created (Supporting Information eq S105b):

$$\gamma = -\frac{\pi\rho^2}{2}\int_0^d \mathrm{d}r r^3 \varphi(r) \tag{41}$$

https://doi.org/10.1021/acs.chemrev.4c00138
Chem. Rev. XXXX, XXX, XXX−XXX

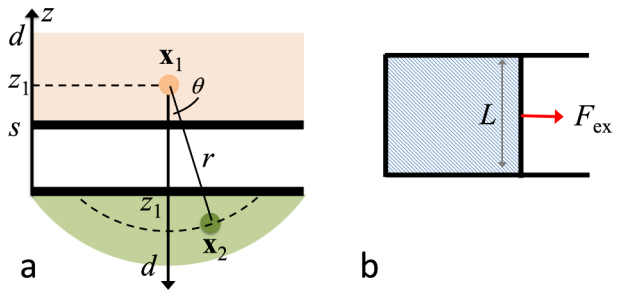

Figure 17. Interpretations of the interfacial tension. (a) As the work per unit interfacial area created. The calculation leading to eq 41 involves integration over $\mathbf{x}_1$ and $\mathbf{r} = \mathbf{x}_2 - \mathbf{x}_1$ or, more specifically, over the z coordinate z_1 of $\mathbf{x}_1$ and the spherical coordinates (r,θ,ϕ) of $\mathbf{r}$ (Supporting Information eq S104b). Domains of integration over $\mathbf{x}_1$ and $\mathbf{r}$ are shaded in light orange and olive green, respectively. (b) As the force per unit length.

where ρ is the number density of the liquid, $\varphi(r)$ is the attractive (i.e., negative) part of the intermolecular interaction energy function (Figure 4a), and d is the distance beyond which the attraction is negligible.

Another perspective on interfacial tension can be gained by examining a two-layer liquid film (such as a soap membrane) held in a metal frame with a movable boundary (Figure 17b). An external force, F_{ex}, is required to balance the tension in the film. When the boundary moves by δx, the work done by F_{ex} equals the increase in the energy of the film:

$$\gamma \delta A = F_{ex} \delta x \tag{42}$$

Now $\delta A = 2L\delta x$ where L is the length of the movable boundary and the factor of 2 accounts for the two layers of the film. Therefore, we have

$$\gamma = \frac{F_{ex}}{2L} \tag{43}$$

The last expression suggests that, in addition to energy per unit area, interfacial tension also represents force per unit length. This force is perpendicular both to the normal direction of the interface and to the boundary line; it is opposite to (hence balances) F_{ex} in the case illustrated in Figure 17b. This meaning of interfacial tension is used in deriving a boundary condition (Supporting Information eq S36). Note also that interfacial tension has the same unit as the spring constant (κ) of a spring. The similarity between an interface and a spring goes beyond a match in units between γ and κ: the forces stored in both of them resist deformation. In Subsection 4.2.4 we will see that, by virtue of its interface, a protein droplet effectively behaves like a spring.

4.2.1. Microscopic Formulation. As illustrated by eq 41, the interfacial tension is determined by intermolecular interactions. The rigorous formulation of the interfacial tension in terms of intermolecular interactions was developed by Kirkwood and co-workers,[302,303] and is summarized in Supporting Information Section S6. For a general review of calculating interfacial tension through molecular simulations, see ref 304. Calculated results for biomolecular condensates have been reported in recent studies (refs 147, 213, 217, 220, 222, 232, 246, and 305−307).

Kirkwood's formulation is most easily implemented in slab-geometry simulations, which produce two interphase interfaces (Figure 9a).[199] The interfacial tension is related to components of the position-averaged pressure tensor $\bar{\tilde{p}}$ (Supporting Information eq S118):

$$\gamma = \frac{L}{2}\left(\bar{p}_{zz} - \frac{\bar{p}_{xx} + \bar{p}_{yy}}{2}\right) \tag{44}$$

where L is the length of the simulation box along the z axis. p_{zz} everywhere equals the scalar pressure p measured far away from the two-phase interfaces, but p_{xx} and p_{yy} at each interface deviate from p. (For a recent perspective on the position-dependent pressure tensor $\tilde{\mathrm{p}}$, see ref 308.) Equation 44 differs from eq S118 by a factor of 2, to account for the fact that, in a slab-geometry simulation, there are two interfaces that contribute to the positional average of the pressure tensor $\tilde{\mathrm{p}}$. We have noted in Subsection 2.5 a qualitative similarity between γ and p; eq 44 shows that there is a direct link between these two properties.

The position-averaged pressure tensor $\bar{\tilde{p}}$ is given by the equilibrium average, denoted by $\langle\cdots\rangle_{eq}$, of the instantaneous pressure tensor (Supporting Information eq S134):

$$\bar{\tilde{p}} = \langle\tilde{\mathrm{p}}\rangle_{eq} \tag{45}$$

$\tilde{\mathrm{p}}$ itself is (Supporting Information eq S133c)

$$\tilde{\mathrm{p}} = \frac{1}{mV}\sum_{n=1}^{N} p_n p_n + \frac{1}{V}\sum_{n=1}^{N} \mathbf{x}_n \mathbf{F}_n \tag{46}$$

where p_n is the momentum of molecule n, $\mathbf{x}_n$ is its position, and $\mathbf{F}_n$ is the total force acting on it by other molecules. The two terms of $\tilde{\mathrm{p}}$ give the ideal and excess parts of $\bar{\tilde{p}}$, respectively; only the excess part contributes to γ. When the molecules are point-like particles and the total potential energy is a sum of all pairwise interactions,

$$\Phi(\{\mathbf{x}_n\}) = \sum_{n<n'}^{N} \varphi(r_{nn'}) \tag{47}$$

the interfacial tension is (Supporting Information eq S136)

$$\gamma = \frac{1}{8A}\sum_{n,n'}^{N} \frac{r_{nn'}^2 - 3z_{nn'}^2}{r_{nn'}} \varphi'(r_{nn'})_{eq} \tag{48}$$

where A is the area of each interface, and a prime on $\varphi(r)$ means the first derivative. Equation 48 differs from eq S136 by a factor of 2, again to account for the fact that the simulation system has two interfaces. For a homogeneous system, the average of $z_{nn'}^2$ is expected to be one-third of $r_{nn'}^2$, and hence $r_{nn'}^2 - 3z_{nn'}^2$ must average out to 0. Therefore, the average in eq 48 comes only from local regions, with dimensions of molecular sizes, where the molecular distributions are inhomogeneous, and these occur at the two interfaces, due to the disparity in density between the two phases. A simple conclusion is then that, other things being equal, the greater the two phases differ in concentration, the larger the interfacial tension.

Indeed, the effect of the disparity in density across the interface is already illustrated clearly by eq 41, where ρ is the difference between the liquid on one side of the interface and a vacuum on the other side. A relationship between γ and the density difference, $\rho_{II} - \rho_I$, between the two phases can also be obtained based on scaling laws. Similar to $\rho_{II} - \rho_I$ (eq 39b), γ is expected to obey a scaling law[192,309]

$$\gamma = \gamma_0(1 - T/T_c)^{\alpha_2} \tag{49a}$$

Combining this result with eq 39b, we obtain

$$\gamma = A(\rho_{II} - \rho_I)^{\alpha_3} \tag{49b}$$

https://doi.org/10.1021/acs.chemrev.4c00138
Chem. Rev. XXXX, XXX, XXX−XXX

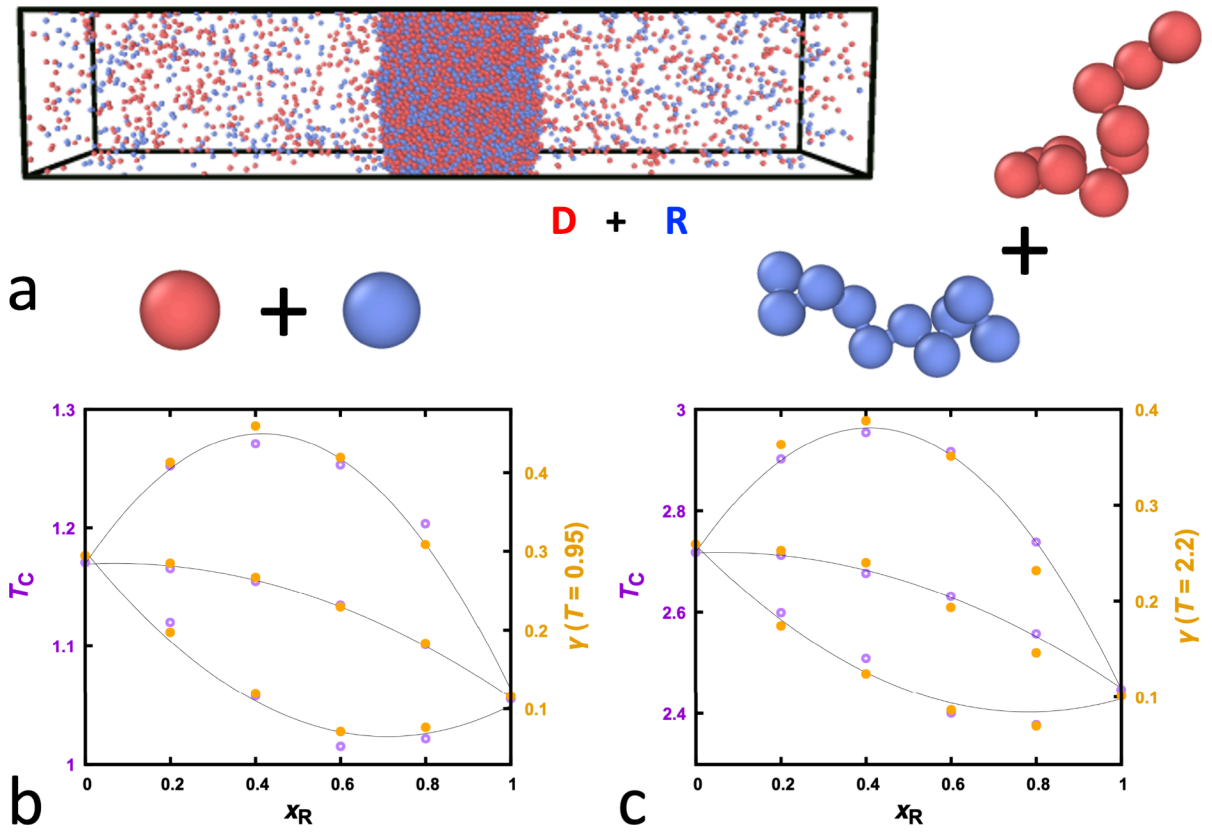

Figure 18. Parallel between the critical temperature and the interfacial tension. (a) The simulation systems. (b) Dependences of T_c and γ on the mole fraction, x_R, of the R component for particle systems. (c) Corresponding results for chain systems. In panels (b) and (c), data at $\epsilon_{DR}/\epsilon_{DD}$ = 1.2, 1.0, and 0.8 are displayed from top to bottom. Reproduced from ref 213 with permission. Copyright 2021 John Wiley and Sons.

Simulation results for systems of particles and polymer chains have confirmed this scaling law, with $\alpha_3 \sim 3.9$.[213] Note that, at the critical point, $\rho_{II} = \rho_I$ and the interfacial tension approaches 0.

It is now also clear that the interfacial tension is proportional to the strength of intermolecular interactions. In Subsections 2.2−2.4 we have emphasized the fact that the critical temperature, T_c, for phase separation is proportional to the strength of intermolecular interactions. Therefore, we expect T_c and γ to increase or decrease in parallel. Mazarakos and Zhou[213] calculated T_c and γ from slab-geometry simulations for binary mixtures of particles and chains (Figure 18a). The two components differed in their strengths of self-attraction, with $\epsilon_{DD} > \epsilon_{RR}$; the label "D" and "R" are for driver and regulator, respectively. The strength of the D-R cross attraction (ϵ_{DR}) was varied. The dependences of T_c on the mole fraction of the R component (x_R) at $\epsilon_{DR} > \epsilon_{DD}$ and $\epsilon_{DR} < \epsilon_{RR}$ (Figure 18b, c) are similar to those noted in Subsection 3.4 for strong-attraction protomers and weak-attraction repressors, respectively (Figure 15a), further validating the classification of macromolecular regulators according to the relative strengths of cross and self-attraction. More interestingly, Figure 18b, c shows that, for both particles and chains and at different ϵ_{DR} values, the change of γ with x_R at a fixed temperature tracks exactly the dependence of T_c on x_R. Validation of the matching effects of regulators on T_c and γ is presented below (Figure 21).

4.2.2. Shape Analysis. Next we describe experimental methods for measuring the interfacial tension. For a static protein droplet, force balance between pressure and interfacial tension leads to the Young−Laplace equation for the shape of the droplet (Supporting Information eq S40):

$$p_{II} - p_I = \gamma \nabla \cdot \mathbf{n} \tag{50}$$

where p_{II} and p_I refer to the interior and exterior pressure, respectively, $\mathbf{n}$ is the outward unit normal vector, and $\nabla \cdot \mathbf{n}$ represents the curvature of the interface. Without gravity or any other external force, eq 50 predicts that the droplet adopts a spherical shape, with radius R given by (Supporting Information eq S61)

$$p_{II} - p_I = \frac{2\gamma}{R} \tag{51}$$

Under gravity, the shape of the droplet will deviate from being spherical and this shape can be used to obtain γ (Figure 19a). Historically this is called the sessile drop method. For a droplet resting on a glass slide, if the radius measured in the equator is R and the height above the equator is H, then (Supporting Information eq S59)

$$\gamma = \frac{\Delta\varrho g H^2}{B(H/R)} \tag{52}$$

where $\Delta\varrho$ is the difference in mass density between the interior and exterior, g is the gravitational acceleration, and $B(x)$ is a cubic function (given by Supporting Information eq S60).

4.2.3. Micropipette Aspiration. The next method is micropipette aspiration, involving inserting a micropipette into the droplet (Figure 19b).[310] The dense phase spontaneously flows into the pipet, and a pressure has to be applied to balance

https://doi.org/10.1021/acs.chemrev.4c00138
Chem. Rev. XXXX, XXX, XXX−XXX

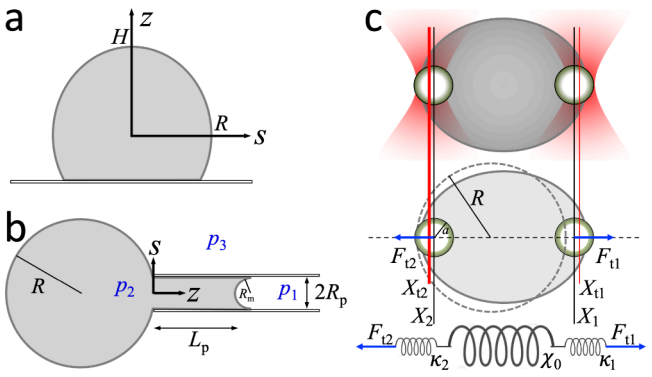

Figure 19. Methods for measuring interfacial tension. (a) Shape analysis. (b) Micropipette aspiration, adapted from ref 310 with permission. Copyright 2021 Elsevier. (c) OT-based active microrheology, adapted from ref 311. Copyright 2021 the original authors. The latter two methods each have a dynamic version, which allows the measurement of viscosity or viscoelasticity, respectively.

it. If the radius of curvature of the meniscus at the rim is R_m, then eq 51 gives us

$$p_1 - p_2 = \frac{2\gamma}{R_m} \tag{53a}$$

where p_1 is the pressure inside the pipet and p_2 is the pressure in the dense phase. R_m typically is close to the radius of the pipet (R_p) as biomolecular condensates tend to wet the glass inner surface of the pipet. Similarly, the pressure difference between the dense phase and the bulk phase gives

$$p_2 - p_3 = \frac{2\gamma}{R} \tag{53b}$$

where R denotes the radius of the droplet. Combining the last equations, one find that the measured aspiration pressure is

$$p_{asp} \equiv p_3 - p_1 \tag{54a}$$

$$= -2\gamma\left(\frac{1}{R_m} + \frac{1}{R}\right) \equiv p_\gamma \tag{54b}$$

$$\approx -\frac{2\gamma}{R_p} \tag{54c}$$

The last step is justified because $R_m \approx R_p \gg R$. A negative p_{asp} means that the pressure is higher inside the pipet.

4.2.4. Active Microrheology. The interfacial tension of a protein droplet can also be measured using a dual-trap optical-tweezers instrument (OT).[312,313] Two optically trapped beads (of radius a) are positioned at the opposite poles of the protein droplet (of radius R) to deform it (Figure 19c top panel). OT uses a focused laser beam to trap micronsized dielectric beads.[314] The force exerted on the bead is approximately like a spring:

$$F_t = -\kappa_t(X - X_t) \tag{55}$$

where X_t and X denote the x coordinates of the center of the laser beam and the center of the bead, respectively, and κ_t denotes the stiffness of the trap (Figure 19c middle panel).

Deformation of the droplet is also similar to stretching a spring, with the extent of deformation, ΔX_0, proportional to the trapping forces. The effective spring constant of the droplet is

$$\chi_0 \equiv \frac{(F_{t1} - F_{t2})/2}{\Delta X_0} \tag{56}$$

By solving the Young−Laplace equation for a droplet under external forces, χ_0 is found to be (Supporting Information eq S74b)[313]

$$\chi_0 = \frac{\pi\gamma(1 - \cos^2\theta_0)/2}{\sum_{l\geq 2; l \text{ even}} \frac{P_{l-1}(\cos\theta_0) - P_{l+1}(\cos\theta_0)}{(l-1)(l+2)}} \tag{57a}$$

where $\theta_0 = a/(R\text{-}a)$ is the polar angle spanned by a bead at the pole, and $P_{l+1}(x)$ are Legendre polynomials. We assume that each bead is buried just beneath the droplet surface, as is usually observed.[311] For $a/R < 0.3$, which is the range of practical interest, eq 57a can be well approximated by[313]

$$\gamma = \frac{1}{\pi}\left[\ln\left(\frac{R}{a} - 1\right) + 0.68\right]\chi_0 \tag{57b}$$

Usually OT does not directly monitor the extent of the droplet deformation. Instead, trap 2 is fixed in place and the displacement of trap 1, ΔX_{t0}, is monitored (Figure 19c middle panel). The resulting spring constant,

$$\chi_{sys} \equiv \frac{(F_{t1} - F_{t2})/2}{\Delta X_{t0}} \tag{58}$$

is that of the system comprising the droplet and two optical traps in series (Figure 19c bottom panel). Using the fact that the forces are balanced for the entire system,

$$F_{t1} + F_{t2} = 0 \tag{59}$$

as well as for each spring, one can easily find the well-known result for springs in series:

$$\frac{1}{\chi_{sys}} = \frac{1}{\chi_0} + \frac{1}{\kappa_{t1}} + \frac{1}{\kappa_{t2}} \tag{60}$$

where κ_{t1} and κ_{t1} are the stiffnesses of the two optical traps.

Interfacial tension has also been estimated based on the rupture force, i.e., the force that is required when a trapped microbead, pulled from inside a protein droplet, ruptures the interface and leaves the droplet.[311] A related method is based on using an atomic force microscope instead of OT to pull a microbead that is glued to the tip of a cantilever.[315,316]

4.2.5. Experimental Data and Interpretations. Interfacial tension has been implicated in the proper organization of nucleolar subcompartments.[11] In general, interfacial tension drives the fusion and hence affects the size distribution of condensates.[317] Interfacial tension has been measured for a relatively small number of condensates (Table 3 and Figure 20). The measured values range from ~1 pN/μm for droplets of nucleophosimin[11] and PGL-3[312,318] to ~250 pN/μm for droplets formed by mixing the recombinant mussel adhesive protein fp-151 (carrying a net positive charge) with hyaluronic acid (a polysaccharide)[315] and droplets of synthetic proteins with a triblock construct F-L-F, where F = a folded domain such as human γD-Crystallin or human fibronectin III domain10, and L = disordered linker.[316]

Compared to the surface tension of ~7×10^4 pN/μm at the water−air interface, the interfacial tensions of biomolecular condensates are two to five orders of magnitude lower. A simple reason for this enormous contrast in γ lies in the disparity in across-interface concentration changes (see eqs 41 and 49b): at

https://doi.org/10.1021/acs.chemrev.4c00138
Chem. Rev. XXXX, XXX, XXX−XXX

Table 3. List of Measured Interfacial Tensions

System	Value (pN/μm)	Method	Refs
NPM1	0.8	Shape analysis	11
PGL-3; 180 mM NaCl	1.1	OT	Data from ref 312 reanalyzed in ref 318
150 mM NaCl	2.1		
115 mM NaCl	2.7		
75 mM NaCl	4.9		
Bik1	7	Shape analysis	319
Urease; pH > 8.2	23	Shape analysis	320
pH < 7.6	40		
Ddx4 1-231	38	Shape analysis	321
Ddx4 1-229	82		
Protamine + 10.2 mM ATP	24	OT	135
Protamine + 5 mM ATP	24		
pK + 100 mM ATP	27		
pK + 10.2 mM ATP	44		
pK + 5 mM ATP	66		
pK + 100 mM ATP; 150 mM KCl	21		
pK + 10.2 mM ATP; 150 mM KCl	49		
pK + 5 mM ATP; 150 mM KCl	50		
pK + heparin	57	OT	311
PolyPRM + heparin	67		
PolySH3 + polyPRM	73		
PolySH3 + lysozyme	106		
PolyPRM + heparin; 300 mM KCl	40		unpublished
400 mM KCl	35		unpublished
pK + heparin; 100 mg/mL Ficoll	95	OT	322
200 mg/mL Ficoll	126		
MMssMM	38	OT	269
LLssLL	109		
FFssFF	96		
Endocytic condensate	70	Pressure difference estimate	323
FUS 1−267	90	Shape analysis	319
LAF-1 RGG domain	170	Micropipette aspiration	188
Crys-ADF3-Crys	162	Atomic force microscope	316
CBM-ADF3-CBM	213		
SC-ADF3-SC	234		
FN-ADF3-FN	284		
fp-151 + HA; 250 mM NaHCOO	236	Atomic force microscope	315
250 mM NaCl	256		
250 mM $NaNO_3$	287		

the water−air interface, the change in water concentration is ~55 M; at the interphase interfaces of condensates, the changes in macromolecular concentration are of the order of 10 mM.

As indicated by eq 41, another determinant of interfacial tension is the strength of intermolecular interactions. For example, the interfacial tension of PGL-3 droplets decreased from 4.9 to 1.1 pN/μm as the KCl concentration increased from 75 to 180 mM, by screening electrostatic attraction.[312,318] Similarly, for polyPRM:heparin (P:H) droplets, as the KCl concentration decreased from 150 mM to 300 mM and 400 mM,

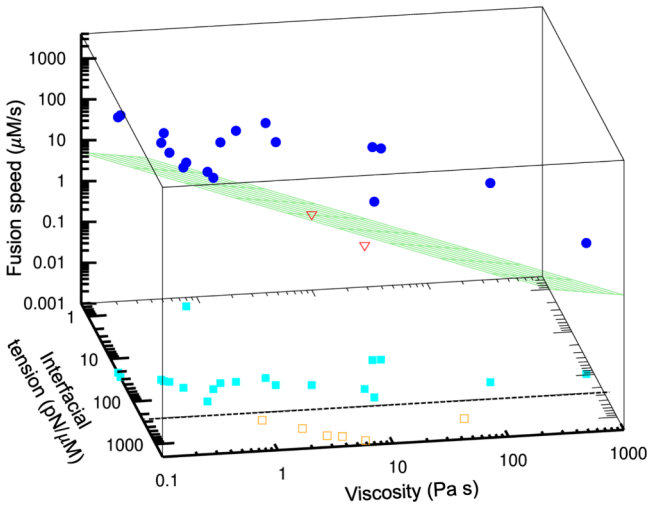

Figure 20. Condensates for which all three of the material properties, interfacial tension, viscosity, and fusion speed, have been measured. The green plane represents the viscocapillary model; blue circles display data points above the plane, implicating shear thinning; red triangles display data points below the plane, implicating shear thickening. Data from refs 11, 135, 188, 269, 300, 310, 311, and 322. Cyan squares display the data on the interfacial tension−viscosity plane; also included are points, shown as orange squares, where interfacial tension was deduced from viscosity and fusion speed by applying the viscocapillary model.[324,325]

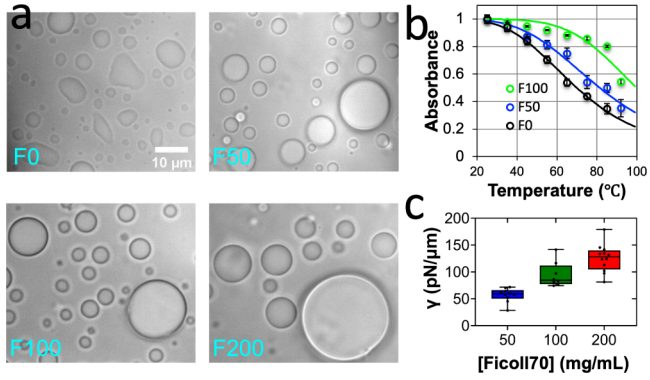

Figure 21. Parallel increases in the melting temperature and interfacial tension of pK:H droplets by Ficoll70. (a) Brightfield images of pK:H droplets at the indicated Ficoll70 concentrations in mg/mL. (b) Increase in melting temperature. (c) Increase in interfacial tension. Reproduced from ref 322. Copyright 2022 American Chemical Society.

the interfacial tension decreased from 67 pN/μm to 40 pN/μm and 35 pN/μm, respectively (ref 311 and unpublished). In the latter study, the two determinants, macromolecular density and interaction strength, were pitted against each other. The authors measured the interfacial tensions of droplets formed by binary components that differed in the relative contents of disordered chains and folded domains, from disordered only (P:H) to a folded-disordered mixture (S:P) to folded only (S:L) (S = polySH3; L = lysozyme). Among them, macromolecular densities in the dense phase appeared to increase with higher folded contents, as indicated by the fluorescence intensity of thioflavin T.[300] On the other hand, the strengths of intermolecular interactions had the opposite order, as shown by the shapes of phase boundaries of ternary mixtures (Figure 15).[146] The interfacial tensions increased, from 67 pN/μm to 106 pN/μm, with increasing folded content, suggesting that in

https://doi.org/10.1021/acs.chemrev.4c00138
Chem. Rev. XXXX, XXX, XXX−XXX

some cases macromolecular density may be the dominant factor. A fourth binary mixture, pK:H (pK = polylysine), with disordered only components, expanded the range of interfacial tensions in this series of binary mixtures down to 57 pN/μm.

Kota and Zhou[322] used the pK:H mixture to test the computational prediction that regulators have matching effects on T_c and γ (Subsection 4.2.1; Figure 18).[213] When the Ficoll70 concentration increased from 50 to 100 and 200 mg/mL, the melting temperature (a proxy for T_c) increased from 70 to 81 °C and 100 °C, respectively, as can be expected for a volume-exclusion promotor (Figure 15). At the same time, the interfacial tension also increased, from 57 pN/μm to 95 pN/μm and 126 pN/μm, respectively, therefore qualitatively validating the computational prediction. Lim et al.[315] reported matching effects of three anions, $HCOO^-$, Cl^-, and NO_3^-, on the phase separation equilibrium and interfacial tension of the fp-151:hyaluronic acid mixture. The interfacial tension values were 236, 256, and 287 at 250 mM sodium salts of the three anions.

Instead of direct measurements, interfacial tension has frequently been deduced from viscosity and fusion speed by applying the viscocapillary model.[9,81,127,177,310,317,324−327] As will be demonstrated in Subsection 4.4.3, biomolecular condensates are viscoelastic and therefore the viscocapillary model, treating condensates as purely viscous, are not applicable. As an indication of its fallacy, the viscocapillary model has led to interfacial tension values, including one at 1600 pN/μm, that are far outside the measured range of ∼1 to ∼250 pN/μm (Figure 20).

4.3. Viscoelasticity

4.3.1. Viscous and Elastic Moduli. Strong bonds (e.g., covalent) between atoms allow solids to maintain their shape. When a solid is deformed, a "restoring" force arises to resist the deformation. For a small deformation (denoted by X; Figure 2b), a linear relation is followed:

$$F_1 = -\kappa_m X \tag{61}$$

This relation is known as Hooke's law; the subscript "m" refers to the material under study. A spring is an idealized model that obeys Hooke's law; κ_m is thus called the spring constant. The larger the spring constant κ_m, the stiffer the solid; κ_m is thus also known as the stiffness. When the external stress is removed, the restoring force returns the solid to its original shape; solids are hence said to be elastic. By contrast, interactions between neighboring molecules are much weaker in liquids and so they do not have a defined shape. Hence a spherical bead can penetrate through a liquid. In so doing, the bead encounters resistance. This resistance is proportional to its velocity (Supporting Information eq S31)

$$F_2 = -\xi_m U \tag{62}$$

The friction coefficient ξ_m is proportional to the liquid viscosity η:

$$\xi_m = 6\pi\eta a \tag{63}$$

where a is the radius of the bead. This result is obtained by solving the Navier−Stokes equations for a bead moving in a quiescent liquid (Supporting Information Section S2). Our interest here is bimolecular condensates, which, similar to dense polymer solutions, straddle between elastic solids and viscous liquids, and will be referred to as viscoelastic materials in this section.

Let us first consider a viscous liquid. When the liquid is subject to a shear flow between two plates (Figure 2a), with a velocity gradient $\partial v_x/\partial y$ (which can also be interpreted as the shear strain rate; see eq 83 below), the liquid resists the shear motion and hence exerts a stress (force per unit area) on the top plate. Conversely, the top plate exerts an equal but opposite stress on the liquid. Viscosity is introduced to quantify a linear relation between the shear stress and the strain rate:

$$\tau_{yx} = \eta\frac{\partial v_x}{\partial y} \tag{64}$$

This relation is known as Newton's law of viscosity; materials that obey this relation, with a constant (shear) viscosity η, are called Newtonian fluids. Of the two indices of τ_{yx}, the first refers to the normal direction of the area on which the stress is exerted, and the second refers to the direction of the stress. The shear stress, $\tilde{\tau}$, is thus a (symmetric) second-rank tensor. Equation 64 applies not only to an area in contact with the top plate but to any area in the viscous liquid; now the stress is exerted by the liquid above the area.

In analogy to the parallel between eqs 61 and 62, a linear relation exists between the shear stress and shear strain, $\partial u_x/\partial y$, in an elastic material:

$$\tau_{yx} = G_0\frac{\partial u_x}{\partial y} \tag{65}$$

which defines the shear modulus, G_0. Extending the analogy, whereas the velocity field, $\mathbf{v} = (v_x, v_y, v_z)$, of a viscous liquid is governed by the Navier−Stokes equations, the displacement field, $\mathbf{u} = (u_x, u_y, u_z)$, of an elastic material is governed by nearly identical equations, with the shear modulus G_0 taking the place of the viscosity η (see also Supporting Information Section S5.2).[328] Consequently, a bead embedded in an elastic material experiences a restoring force given by eq 61, with the spring constant κ_m, in analogy to eq 63, related to the shear modulus via

$$\kappa_m = 6\pi G_0 a \tag{66}$$

A bead in a viscoelastic material experiences both a restoring force and a viscous drag, similar to a bead attached to a spring while immersed in a liquid (Figure 22a). If the bead is pulled by an external force F_{ex}, then force balance leads to[329]

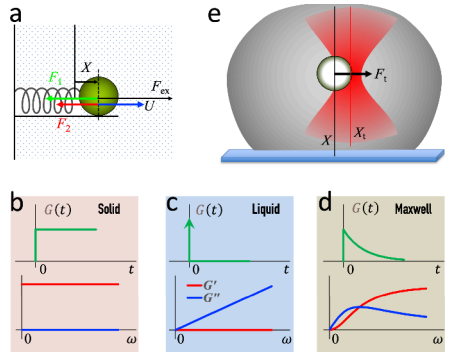

Figure 22. Illustration of viscoelasticity and its measurement. (a) Model for the motion of a bead in a viscoelastic material. F_1 and F_2 denote the elastic force and viscous force, respectively. (b) Shear relaxation modulus and complex shear modulus for an elastic solid. (c) Corresponding results for a viscous liquid. (d) Corresponding results for a Maxwell model. (e) OT-based active microrheology. Panels (b−e) adapted from ref 311. Copyright 2021 the original authors.

https://doi.org/10.1021/acs.chemrev.4c00138
Chem. Rev. XXXX, XXX, XXX−XXX

$$-\kappa_m X - \xi_m U + F_{ex} = 0 \tag{67}$$

While eq 67 is strictly valid only when the bead is moving at constant velocity (i.e., 0 acceleration), it is also valid at high viscosity, where the acceleration (i.e., inertial) term can be neglected. Now consider the situation where the external force varies sinusoidally with time,

$$F_{ex}(t) = F_{ex0}e^{i\omega t} \tag{68}$$

where ω is the angular frequency. The bead position must have the following form:

$$X(t) = X_0 e^{i(\omega t-\delta)} \tag{69}$$

where δ denotes a phase shift. Solving eq 67, we find

$$\kappa_m + i\omega\xi_m = \frac{F_{ex0}}{X_0}e^{i\delta} \tag{70}$$

If the material were purely elastic (i.e., $\eta = 0$), we would have

$$F_{ex}(t) = \kappa_m X(t) = 6\pi a G_0 X(t) \tag{71}$$

For a viscoelastic material, we can generalize the last relation to

$$F_{ex}(t) = 6\pi a G^*(\omega)X(t) \tag{72}$$

and thereby define a complex shear modulus

$$G^*(\omega) = G'(\omega) + iG''(\omega) \tag{73}$$

Substituting eqs 68 and 69 into eq 72 and comparing against eq 70, we find

$$6\pi a G^*(\omega) = \kappa_m + i\omega\xi_m \tag{74a}$$

$$= \frac{F_{ex0}}{X_0}e^{i\delta} \tag{74b}$$

Equation 74a allows us to identify the real part of $G^*(\omega)$ with κ_m and the imaginary part with $\omega\xi_m$. If κ_m is given by eq 66 and ξ_m is given by eq 63, then

$$G'(\omega) = \frac{\kappa_m}{6\pi a} = G_0 \tag{75a}$$

$$G''(\omega) = \frac{\omega\xi_m}{6\pi a} = \omega\eta \tag{75b}$$

These relations explain why $G'(\omega)$ is called the elastic (or storage) modulus whereas $G''(\omega)$ the viscous (or loss) modulus. For an elastic solid, $G'(\omega) = G_0$ and $G''(\omega) = 0$ (Figure 22b). For a viscous liquid (i.e., Newtonian fluid), $G'(\omega) = 0$ and $G''(\omega)$ is a linear function of ω with η as the slope (Figure 22c).

Equation 74b allows the real and imaginary parts of $G^*(\omega)$ to be expressed in terms of the amplitude ratio F_{ex0}/X_0 and the phase shift δ:

$$G'(\omega) = \frac{F_{ex0}}{6\pi a X_0}\cos\delta \tag{76a}$$

$$G''(\omega) = \frac{F_{ex0}}{6\pi a X_0}\sin\delta \tag{76b}$$

Relations similar to eqs 76a and 76b can be used to determine $G^*(\omega)$ (Subsection 4.3.6).

4.3.2. Shear Relaxation Modulus. Equation 64 presents only the yx element of the stress tensor, when a gradient of v_x exists along the y direction (Figure 2a). In a general velocity field $\mathbf{v}$, the symmetrized strain-rate tensor is

$$\tilde{\varepsilon} = \nabla\mathbf{v} + (\nabla\mathbf{v})^T \tag{77}$$

where ∇ denotes the gradient operator, and the subscript "T" denotes transpose. For a Newtonian fluid, eq 64 now becomes

$$\tilde{\tau}_d = \eta\tilde{\varepsilon} \tag{78}$$

where the subscript "d" signifies deviatoric. When a pressure, p, exists in the fluid, it also makes a contribution to the stress tensor:

$$\tilde{\tau}_h = -p\tilde{I} \tag{79}$$

where $\tilde{I}$ is the unit tensor, the negative sign arises from the convention that the outward normal of the area under stress is taken as positive, and the subscript "h" signifies hydrostatic. The total stress tensor of the Newtonian fluid is thus

$$\tilde{\tau} = \tilde{\tau}_h + \tilde{\tau}_d \tag{80a}$$

$$= -p\tilde{I} + \eta\tilde{\varepsilon} \tag{80b}$$

Our interest is materials that have a more complex relation between $\tilde{\tau}_d$ and $\tilde{\varepsilon}$ than for a Newtonian fluid. We want to confine to small strain rates so that the relation between $\tilde{\tau}_d$ and $\tilde{\varepsilon}$ is still linear but, at any given moment t, $\tilde{\tau}_d(t)$ depends not only on the value of $\tilde{\varepsilon}$ at the same moment but its entire history. Hence

$$\tilde{\tau}_d = \int_{-\infty}^{t} dt' G(t-t')\tilde{\varepsilon}(t') \tag{81a}$$

The function $G(t)$ introduced in the above equation is called the shear relaxation modulus. Note that $\tilde{\tau}_d(t)$ should not depend on $\tilde{\varepsilon}(t')$ for $t' > t$. That means that we have to stipulate that

$$G(t) = 0 \text{ for } t < 0 \tag{81b}$$

With this stipulation, we can change the upper limit of the integral in eq 81a to $+\infty$,

$$\tilde{\tau}_d = \int_{-\infty}^{+\infty} dt' G(t-t')\tilde{\varepsilon}(t') \tag{81c}$$

Analogous to eq 77, the shear-strain tensor can be defined as

$$\tilde{\sigma} = \nabla\mathbf{u} + (\nabla\mathbf{u})^T \tag{82}$$

in terms of the displacement field $\mathbf{u}$. It is obvious that

$$\tilde{\varepsilon} = \frac{\partial}{\partial t}\tilde{\sigma} \tag{83}$$

Now consider a velocity field due to a sinusoidal change of the shear strain over time,

$$\tilde{\sigma} = \tilde{\sigma}_0 e^{i\omega t} \tag{84a}$$

According to eq 83, the corresponding strain-rate tensor is

$$\tilde{\varepsilon} = i\omega\tilde{\sigma}_0 e^{i\omega t} \tag{84b}$$

Substituting eq 84b into eq 81c, we find

$$\tilde{\tau}_d = i\omega\tilde{\sigma}_0 e^{i\omega t}\int_{-\infty}^{+\infty} dt' e^{-i\omega t'}G(t') \tag{85a}$$

$$= \hat{G}(\omega)\tilde{\varepsilon} \tag{85b}$$

$$\equiv G^*(\omega)\tilde{\sigma} \tag{85c}$$

In the second line, $\hat{G}(\omega)$ denotes the Fourier transform of $G(t)$; the third line generalizes eq 65 and formally defines the complex

https://doi.org/10.1021/acs.chemrev.4c00138
Chem. Rev. XXXX, XXX, XXX−XXX

shear modulus. We find the following relation between the shear relaxation modulus and the complex shear modulus,

$$G^*(\omega) = i\omega \int_{-\infty}^{+\infty} dt e^{-i\omega t} G(t) \tag{86a}$$

$$= i\omega \hat{G}(\omega) \tag{86b}$$

By comparing eq 85b with eq 78, we see that $\hat{G}(\omega)$ plays the same role under an oscillatory shear at angular frequency ω as the viscosity η under a steady shear. (Sometimes $\hat{G}(\omega)$ is referred to as the frequency-dependent viscosity.) This analogy between η and $\hat{G}(\omega)$ will be used in Subsection 4.3.3 to obtain a microscopic formulation of viscoelasticity. A steady shear can be seen as an oscillatory shear with $\omega = 0$. We thus have

$$\eta = \hat{G}(0) \tag{87a}$$

$$= \int_0^\infty dt G(t) \tag{87b}$$

η as defined by eq 78 is the viscosity measured at a small, constant shear rate, and will be referred to as the zero-shear viscosity when it is necessary to be specific. For viscoelastic materials like polymer solutions, as the (constant) shear rate is increased in value, the shear stress typically no longer grows linearly as modeled by eq 78. At high shear rates, the effective viscosity, defined as the ratio of $\tilde{\tau}_d$ over $\tilde{\varepsilon}$, can be much lower than the zero-shear viscosity; this phenomenon is known as shear thinning. The opposite could occur at intermediate shear rates, where the effective viscosity is higher than the zero-shear viscosity, corresponding to shear thickening.

For a Newtonian fluid, the constitutive relation eq 78 corresponds to a delta function for the shear relaxation modulus (Figure 22c):

$$G(t) = \eta\delta(t) \tag{88}$$

So in a Newtonian fluid, $G(t)$ decays to 0 instantaneously; we say then that shear relaxation occurs infinitely fast. In contrast, for an elastic solid, using its complex shear modulus $G^*(\omega) = G_0$ in eq 86a, we find its shear relaxation modulus to be a step function (Figure 22b):

$$G(t) = G_0 \text{ for } t > 0 \tag{89}$$

That is, $G(t)$ does not decay over time and hence shear relaxation is infinitely slow.

In the so-called Maxwell model, shear relaxation is an exponential function of time, with a time constant τ_1 (Figure 22d),

$$G(t) = \frac{\eta}{\tau_1} e^{-t/\tau_1} \text{ for } t > 0 \tag{90}$$

The complex shear modulus is

$$G^*(\omega) = \frac{i\omega\eta}{1 + i\omega\tau_1} \tag{91a}$$

In the limit $\tau_1 \to 0$, the Maxwell model reduces to a Newtonian fluid, consistent with the fact that shear relaxation there occurs instantaneously. The real and imaginary parts of the Maxwell $G^*(\omega)$ are

$$G'(\omega) = \frac{\omega^2\tau_1\eta}{1 + \omega^2\tau_1^2} \tag{91b}$$

$$G''(\omega) = \frac{\omega\eta}{1 + \omega^2\tau_1^2} \tag{91c}$$

In this case, $G'(\omega)$ is a monotonically increasing function of ω; in contrast, $G''(\omega)$ reaches maximum at $\omega\tau_1 = 1$ (Figure 22d). $G''(\omega)$ is larger than $G'(\omega)$ at $\omega\tau_1 < 1$ whereas the opposite is true at $\omega\tau_1 > 1$. Thus the Maxwell model behaves as a viscous fluid at low frequencies (or for slow motions) but as an elastic solid at high frequencies (or for fast motions).

No liquids can be purely viscous, where shear relaxation occurs instantaneously and $G''(\omega)$ grows in proportion to ω indefinitely. For example, glycerol and water are generally thought of as viscous liquids, but their shear relaxation moduli are actually qualitatively Maxwellian at very high frequencies (GHz to THz), corresponding to shear relaxation times on the ns and ps time scales, respectively.[330,331] In general, materials appear purely viscous on time scales much longer than that of shear relaxation.

An arbitrary shear relaxation modulus can be written as a finite or infinite sum of exponentials and, correspondingly, the complex shear modulus can be written as a sum of terms like eq 91a. In particular, the Jeffreys model is a linear combination of a Newtonian fluid and a Maxwell model, with the complex shear modulus given by

$$G^*(\omega) = i\omega\eta_0 + \frac{i\omega\eta_1}{1 + i\omega\tau_1} \tag{92a}$$

One can expect this model to represent well a dilute polymer solution, where the first term represents the viscous solvent, and the second term represents the contribution of the polymer solute. Another model is to replace the Newtonian component by another Maxwell component:

$$G^*(\omega) = \frac{i\omega\eta_0}{1 + i\omega\tau_0} + \frac{i\omega\eta_1}{1 + i\omega\tau_1} \tag{92b}$$

leading to the Burgers model; the two terms are ordered such that $\tau_0 < \tau_1$. In both the Jeffreys and Burgers models, the zero-shear viscosity is given by $\eta = \eta_0 + \eta_1$. These models have been used to analyze viscoelasticity data for biomolecular condensates.[135,311,313,318,322,332]

4.3.3. Microscopic Formulations of Viscosity and Viscoelasticity. So far we have presented only a mechanical view of viscoelasticity. In theory, all properties, viscoelasticity included, of a molecular system are fully determined by the equations of motion of and forces acting on the constituent molecules. By simulating the molecular motions, one should be able to compute such properties. Below we present formulations for viscoelastic properties to illustrate how such computation can be done. These expressions should not be taken as algorithms for actual computation, but as a vehicle for understanding how viscoelasticity is determined by microscopic properties, to aid in the physical interpretation of experimental data (see Subsection 4.3.8). As such, we consider only the simplest molecular system already introduced in Subsection 4.2.1 for calculating the interfacial tension, comprising N point particles with mass m, positions $\mathbf{x}_n$, and velocities $\mathbf{v}_n$, and obeying Newton's equation of motion with forces $\mathbf{F}_n$.

As illustrated by eq 32, the viscosity, defined through eq 64, is a transport coefficient, much like the diffusion constant. Microscopically, transport coefficients can be expressed as time integrals of time-correlation functions, known as Green–

https://doi.org/10.1021/acs.chemrev.4c00138
Chem. Rev. XXXX, XXX, XXX−XXX

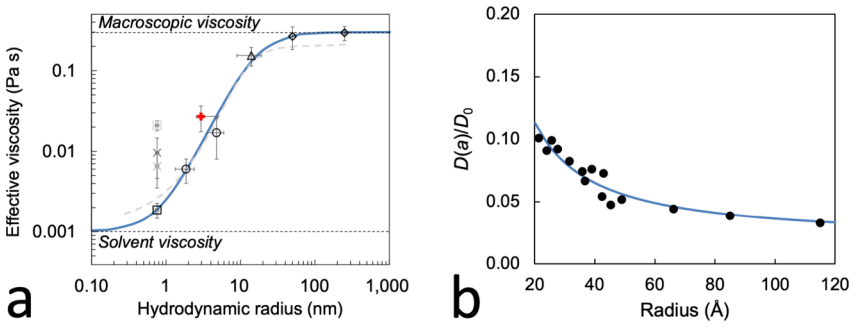

Figure 23. Dependence of effective viscosity on probe radius. (a) Data of Galvanetto et al. in condensates formed by histone 1 and prothymosin-α. This panel was adapted from ref 177 with a fit to eq 102 added as a blue curve. (b) Data from Ando and Skolnick,[340] after adding a correction $2.84\eta_0/\eta_m L$ for the finite system size[342] (L: side length of simulation box = 710 Å). A fit to eq 102 is shown as a blue curve, with $\alpha_0 = 1.1$ and d set to the mean interparticle distance of 90 Å in the simulations.

Kubo relations.[333,334] The viscosity is given by (Supporting Information eq S158)

$$\eta = \frac{V}{k_B T}\int_0^\infty \mathrm{d}t \langle \mathbb{P}_{yx}(t)\mathbb{P}_{yx}(0)\rangle_{eq} \tag{93}$$

where $\mathbb{P}_{yx}$ is the yx component of the instantaneous pressure tensor given by eq 46, and $\langle\cdots\rangle_{eq}$, as in Subsection 4.2.1, signifies an equilibrium average. The pressure tensor thus determines both the interfacial tension (eqs 44−46) and the viscosity. However, it is important to emphasize that, whereas interfacial tension is a thermodynamic property, viscosity is a dynamic, i.e., time-dependent, property. While the part of the pressure tensor related to the kinetic energy makes no contribution to the interfacial tension (see eq 48), the effect of the kinetic energy on η cannot be eliminated. More importantly, the time interval over which $\mathbb{P}_{yx}$ becomes uncorrelated with itself is crucial to the magnitude of η. For a general review of calculating viscosity using the Green−Kubo relation, see ref 335. Calculated results for coarse-grained models of IDPs have been reported in some studies.[217,225,336]

Comparing eq 93 with eq 87b, we can recognize that the autocorrelation function of $\mathbb{P}_{yx}$ as the microscopic version of the shear relaxation modulus:[337,338]

$$G(t) = \frac{V}{k_B T}\langle \mathbb{P}_{yx}(t)\mathbb{P}_{yx}(0)\rangle_{eq} \tag{94}$$

Its Fourier transform

$$\hat{G}(\omega) = \frac{V}{k_B T}\int_0^\infty \mathrm{d}t e^{-i\omega t}\langle \mathbb{P}_{yx}(t)\mathbb{P}_{yx}(0)\rangle_{eq} \tag{95}$$

generalizes viscosity into viscoelasticity; the corresponding complex shear modulus is (eq 86b)

$$G^*(\omega) = \frac{i\omega V}{k_B T}\int_0^\infty \mathrm{d}t e^{-i\omega t}\mathbb{P}_{yx}(t)\mathbb{P}_{yx}(0)_{eq} \tag{96}$$

The above formulations of viscosity and viscoelasticity rely on the simulation of a molecular system at equilibrium. One can also subject the molecular system to a steady shear and then uses eq 64 to determine the zero-shear viscosity,[246] or an oscillatory shear as represented by eq 84a and then uses eq 85c to determine $G^*(\omega)$.[336] Specifically, in the latter case, the simulation box is deformed as depicted in Figure 2b, with the strain varying as a sinusoidal function of time

$$\sigma_{yx} = \sigma_{yx0}e^{i\omega t} \tag{97}$$

to drive the system. The stress tensor is exactly the negative of the pressure tensor (Supporting Information eq S106):

$$\tilde{\tau} = -\tilde{p} \tag{98}$$

The average of $\tilde{\tau}$ over all positions in the simulation box is then given by, analogous to eq 45, an average of the instantaneous pressure tensor,

$$\bar{\tilde{\tau}} = -\tilde{\mathbb{P}}_{ne} \tag{99}$$

Here the subscript "ne" (for nonequilibrium) signifies that the average is done by summing not over all time frames but only over frames that have the same time shift from the peak strains in different periods (of interval $2\pi/\omega$). Also, the particle velocities that appear in eq 46 for $\tilde{\mathcal{P}}$ should have the local fluid velocity subtracted out. Finally the yx component of $\bar{\tilde{\tau}}$ is fit to a sinusoidal function,

$$\bar{\tau}_{yx} = \tau_{yx0}e^{i(\omega t+\delta)} \tag{100}$$

and the complex shear modulus can be identified as

$$G^*(\omega) = \frac{\tau_{yx0}}{\sigma_{yx0}}e^{i\delta} \tag{101}$$

4.3.4. Viscosity at Different Length Scales. As commented in Subsection 4.3.2 (text between eqs 86b and 87a), (linear) viscoelasticity measures the change of viscosity over different frequencies, or equivalently, over different time scales. For any macromolecular solution, viscosity also changes over different length scales. Specifically, probes of different sizes sense different viscosities. At one limit, the translational diffusion of a probe much larger than the solute macromolecules senses the high macroscopic viscosity. At the other limit, a probe that is of a size comparable to solvent molecules measures the much lower solvent viscosity. Probe sizes in between then report intermediate viscosities.

Galvanetto et al.[177] used fluorescently labeled molecules and beads to measure the probe size-dependent viscosity inside H1-ProTα condensates. The effective viscosities ranged from a macroscopic value of 0.3 Pa s as measured using mean-square-displacements (MSDs) of fluorescent beads (250 nm radius) to 0.002 Pa s as measured on a fluorophore Cy3B (0.76 nm radius) using fluorescence correlation spectroscopy. They fit the dependence on probe size to an expression derived by Tuinier et al.[339] The latter authors solved the Stokes equations for a solid bead (Supporting Information Section S2), assuming that the viscosity takes the value of the solvent (η_0) in the surface region

https://doi.org/10.1021/acs.chemrev.4c00138
Chem. Rev. XXXX, XXX, XXX−XXX

not accessible to the center of any macromolecule due to steric repulsion and the macroscopic value (η_m) farther away from the probe.

A serious omission in the model of Tuinier et al. is hydrodynamic interactions, which arise from the interference between the flow fields caused by the motions of the probe and the macromolecules. Ando and Skolnick have shown that hydrodynamic interactions make a substantial contribution to the diffusional slowdown of a probe in dense macromolecular solutions like the cytoplasm,[340] in essence, by coupling the probe to nearby macromolecules. The effect of hydrodynamic interactions depends on the dimensionless parameter $q = a/d$, where a is the probe radius and d is a length scale of the macromolecules. Petit et al.[341] suggested that the appropriate choice for d is the mean distance between macromolecules in the solution, which scales with concentration as $d \approx C^{-1/3}$. We propose the following empirical formula for the dependence of the effective viscosity, η_{eff}, on probe size:

$$\frac{\eta_{eff}(a)}{\eta_0} \equiv \frac{D_0}{D(a)} = \frac{1 + (\eta_m/\eta_0)(a/d)^{\alpha_0}}{1 + (a/d)^{\alpha_0}} \tag{102}$$

where α_0 is a fitting parameter. The data of Galvanetto et al. are represented well by this formula, with d = 16.3 nm and α_0 = 1.9 (Figure 23a). For comparison, the mean distance between IDP molecules in the dense phase estimated according to their concentrations (~15 mM for the two IDPs) is 4.8 nm; perhaps this estimate is more relevant for folded proteins than for IDPs. Hydrodynamic interactions may be different for IDP chains and folded proteins.

Brady et al.[174] measured diffusion constants for probes up to 30 Å in radius in concentrated protein solutions and in Ddx4 condensates, and fit their data to a different empirical formula: $D_0/D = \exp(Aa^{\alpha})$. When applied to large probes, this formula predicts a vanishing diffusion constant and hence an infinite effective viscosity, rather than the finite macroscopic viscosity. Equation 102 can fit the small-probe data of Brady et al. and, by design, goes to the correct limit for large probes. Equation 102 also models well the probe diffusion constants of Ando and Skolnick obtained from Brownian dynamics simulations of dense spheres with hydrodynamic interactions (Figure 23b). Note that, outside the present subsection, viscosity generally refers to macroscopic viscosity, typically measured at the μm scale.

4.3.5. Viscosity Measurement by Micropipette Aspiration. In the setup of micropipette aspiration presented in Subsection 4.2.3, the aspiration pressure (p_{asp}) exactly balances interfacial tension (equivalent to a pressure p_γ; eq 54b) so that the spontaneous flow of the dense phase is stopped (Figure 19b). When p_{asp} is higher than p_γ, the dense phase will keep flowing into the pipet. The rate of the resulting Poiseuille flow can be used to measure the (zero-shear) viscosity.[188]

The mean velocity, $\bar{v}_z$, of the Poiseuille flow is given by eq 36b of Subsection 2.6.3. $\bar{v}_z$ can be recognized as $\frac{dL_p}{dt}$, i.e., the rate at which the length, L_p, of the dense phase in the pipet increases; the pressure difference Δp can be recognized as p_{asp} - p_γ. Equation 36b now becomes

$$\frac{dL_p}{dt} = \frac{{R_p}^2}{8\eta}\frac{p_{asp} - p_\gamma}{L_p} \tag{103}$$

which can be solved to yield a relation between p_{asp} and the flow rate

$$p_{asp} = \eta Q - 2\gamma\left(\frac{1}{R_m} + \frac{1}{R}\right) \tag{104}$$

where the nominal flow rate is defined as

$$Q = \frac{4}{{R_p}^2}\frac{d{L_p}^2}{dt} \tag{105}$$

p_{asp} is thus a linear function of Q, with the intercept yielding the interfacial tension and the slope yielding the viscosity.

4.3.6. Active Microrheology for Viscoelasticity. In addition to interfacial tension, OT also provides a convenient means for probing viscoelastic properties of materials at the microscale. When a single optically trapped bead is inside a viscoelastic material such as a protein droplet (Figure 22e), eq 67, with the trapping force F_t of eq 55 as the external force, becomes[329,343]

$$-\kappa_m X - \xi_m U - \kappa_t(X - X_t) = 0 \tag{106a}$$

After some rearrangement, we have

$$(\kappa_m + \kappa_t)X + \xi_m U = \kappa_t X_t \tag{106b}$$

In Subsection 4.3.1, we solved the toy model of Figure 22a by treating the external force as the drive and the bead position as the response (see eqs 68 and 69). In OT, it may be more convenient to set the trap position as drive. That is, the trap position is given as a sinusoidal function of time

$$X_t = X_{t0}e^{i\omega t} \tag{107}$$

with a known amplitude X_{t0}. If the bead position is monitored as the response, with amplitude X_0 and phase shift -δ (X again given by eq 69, but now the phase shift is relative to X_t), then eqs 76a and 76b for the elastic and viscous moduli change to

$$G'(\omega) = \frac{\kappa_t}{6\pi a}\left(\frac{X_{t0}}{X_0}\cos\delta - 1\right) \tag{108a}$$

$$G''(\omega) = \frac{\kappa_t}{6\pi a}\frac{X_{t0}}{X_0}\sin\delta \tag{108b}$$

where a as before denotes the radius of the bead.

Usually OT monitors the trapping force F_t instead of the bead position. Let the trapping force be

$$F_t = F_{t0}e^{i(\omega t + \Delta)} \tag{109}$$

where F_{t0} denotes the force amplitude and Δdenotes the phase shift of the trapping force from the trap position. According to eq 55, we have

$$F_{t0}e^{i\Delta} = \kappa_t(X_{t0} - X_0 e^{-i\delta}) \tag{110a}$$

Or, in terms of real and imaginary parts of both sides,

$$F_{t0}\cos\Delta = \kappa_t(X_{t0} - X_0\cos\delta) \tag{110b}$$

$$F_{t0}\sin\Delta = \kappa_t X_0\sin\delta \tag{110c}$$

These relations allow us to use the amplitude and phase angle of the trapping force to express X_0 and δ. In terms of F_{t0} and Δ, the elastic and viscous moduli are now

$$G'(\omega) = \frac{F_{t0}}{6\pi a X_{t0}}\frac{\cos\Delta - \Upsilon}{(\cos\Delta - \Upsilon)^2 + \sin^2\Delta} \tag{111a}$$

https://doi.org/10.1021/acs.chemrev.4c00138
Chem. Rev. XXXX, XXX, XXX−XXX

$$G''(\omega) = \frac{F_{t0}}{6\pi a X_{t0}} \frac{\sin \Delta}{(\cos \Delta - \Upsilon)^2 + \sin^2 \Delta} \tag{111b}$$

where $\Upsilon = F_{t0}/\kappa_t X_{t0}$. When $\Upsilon \ll 1$, eqs 111a and 111b simplify to

$$G'(\omega) \approx \frac{F_{t0}(\cos \Delta - \Upsilon)}{6\pi a X_{t0}} \tag{112a}$$

$$G''(\omega) \approx \frac{F_{t0} \sin \Delta}{6\pi a X_{t0}} \tag{112b}$$

Another way to determine viscoelastic properties of biomolecular condensates was introduced by Jawerth et al.,[312] requiring two optical traps (Figure 19c). This setup is the oscillatory version of the static experiment for determining interfacial tension presented in Subsection 4.2.44.2.4. Let the bead position, trap position, and trap stiffness be X_j, X_{tj}, and κ_{tj}, respectively, for trap j, $j = 1$ or 2. The force exerted by trap j is

$$F_{tj} = -\kappa_{tj}(X_j - X_{tj}) \tag{113}$$

In the experiment, trap 2 is fixed at the origin,

$$X_{t2}(t) = 0 \tag{114}$$

while trap 1's position is set as a sinusoidal function of time,

$$X_{t1}(t) = 2R + \Delta X_{t0} e^{i\omega t} \tag{115}$$

where R is the radius of the undeformed droplet. Then the bead positions X_j and the forces F_{tj} are all sinusoidal functions of time,

$$X_j(t) = 2R\delta_{j1} + \hat{X}_j(\omega)e^{i\omega t} \tag{116}$$

$$F_{tj}(t) = \hat{F}_{tj}(\omega)e^{i\omega t} \tag{117}$$

where δ_{j1} equals 1 for $j = 1$ and equals 0 for $j = 2$. Any phase shifts have been absorbed into the nominal amplitudes $\hat{X}_j(\omega)$ and $\hat{F}_{tj}(\omega)$, which can thus be complex. Equation 113 now becomes

$$\hat{X}_j(\omega) + \frac{\hat{F}_{tj}(\omega)}{k_{tj}} = \delta_{j1}\Delta X_{t0} \tag{118}$$

The deformation of the droplet is

$$\Delta\hat{X}(\omega) = \hat{X}_1(\omega) - \hat{X}_2(\omega) \tag{119}$$

The "dynamic" spring constant of the droplet is thus

$$\chi(\omega) \equiv \frac{[\hat{F}_{t1}(\omega) - \hat{F}_{t2}(\omega)]/2}{\Delta\hat{X}(\omega)} \tag{120}$$

This parameter is complex and is determined by the viscoelastic properties and the interfacial tension of the droplet, as further explained below; for now let us continue with its experimental measurement. If the droplet deformation is replaced by the amplitude, ΔX_{t0}, of the separation between the two traps, we obtain the spring constant of the entire system, i.e., the droplet plus two optical traps:

$$\chi_{sys}(\omega) \equiv \frac{[\hat{F}_{t1}(\omega) - \hat{F}_{t2}(\omega)]/2}{\Delta X_{t0}} \tag{121}$$

As ΔX_{t0} is the drive and $\hat{F}_{tj}(\omega)$ are monitored as the response, $\chi_{sys}(\omega)$ is easily obtained. Using eq 118, we can relate $\chi_{sys}(\omega)$ to $\chi(\omega)$:

$$\frac{1}{\chi_{sys}(\omega)} = \frac{1}{\chi(\omega)} + \frac{\frac{\hat{F}_{t1}(\omega)}{\kappa_{t1}} - \frac{\hat{F}_{t2}(\omega)}{\kappa_{t2}}}{[\hat{F}_{t1}(\omega) - \hat{F}_{t2}(\omega)]/2} \tag{122}$$

If the net force on the system is set to zero,

$$\hat{F}_{t1}(\omega) + \hat{F}_{t2}(\omega) \to 0 \tag{123a}$$

then eq 122 reduces to

$$\frac{1}{\chi_{sys}(\omega)} \to \frac{1}{\chi(\omega)} + \frac{1}{\kappa_{t1}} + \frac{1}{\kappa_{t2}} \tag{123b}$$

These last two equations are the same as eqs 59 and 60 for the static experiment derived in Subsection 4.2.4.

A nonzero net force will drive the translational motion of the droplet. That motion can be tracked by the displacement of the center of the droplet, given by

$$\Delta\hat{X}_c(\omega) = \frac{1}{2}[\hat{X}_1(\omega) + \hat{X}_2(\omega)] \tag{124}$$

Its velocity is $i\omega\cdot\Delta\hat{X}_c(\omega)$. We treat the bulk phase, in which the droplet moves, as a Newtonian fluid; therefore, following eq 63, the friction coefficient ξ_b is $6\pi\eta_b R$, with η_b denoting the viscosity of the bulk phase. The corresponding equation of motion is

$$\hat{F}_{t1}(\omega) + \hat{F}_{t2}(\omega) = i\omega\xi_b\cdot\Delta\hat{X}_c(\omega) = \frac{i\omega\xi_b}{2}[\hat{X}_1(\omega) + \hat{X}_2(\omega)] \tag{125}$$

The static case corresponds to $\omega = 0$; in that case, the net force is 0. For $\omega > 0$, using eqs 118, 121, and 125, we can find $\hat{X}_j(\omega)$ and $\hat{F}_{tj}(\omega)$ in terms of ΔX_{t0} and $\chi_{sys}(\omega)$. The final result for the dynamic spring constant of the droplet is

$$\frac{1}{\chi(\omega)} = \frac{1}{\chi_{sys}(\omega)} \frac{4\kappa_{t1}\kappa_{t2} + 2i\omega\xi_b\kappa_{t1}}{4\kappa_{t1}\kappa_{t2} + i\omega\xi_b(\kappa_{t1} + \kappa_{t2})} - \frac{4(\kappa_{t1} + \kappa_{t2}) + 4i\omega\xi_b}{4\kappa_{t1}\kappa_{t2} + i\omega\xi_b(\kappa_{t1} + \kappa_{t2})} \tag{126}$$

In Supporting Information Subsection S5.2, we derive the dynamic spring constant $\chi(\omega)$ for a droplet modeled with complex shear modulus $G^*(\omega)$ and interfacial tension γ. The result is

$$\chi(\omega) = \frac{\pi R(1 - \cos^2\theta_0)/2}{\sum_{l\geq 2; l \text{ even}} \frac{P_{l-1}(\cos\theta_0) - P_{l+1}(\cos\theta_0)}{2G^*(\omega)\frac{(l-1)(2l^2+4l+3)}{l(2l+1)} + \frac{\gamma}{R}(l-1)(l+2)}} \tag{127}$$

where θ_0 as stated in the static case is the polar angle spanned by a bead at the pole of the droplet. Note that, at $\omega = 0$, $G^*(\omega) \to 0$ and we recover eq 57a of the static case. Jawerth et al.[312] derived only an incomplete expression for $\chi(\omega)$, terminating the infinite sum at $l = 10$. This sum turns out to be notoriously slow to converge for $\theta_0 \leq 0.1$, the range of practical interest; the truncation at $l = 10$ thus leads to serious errors. Eq 127 for $\chi(\omega)$ with the full summation was derived by Zhou.[313]

Even with $\chi(\omega)$ measured experimentally, one still has the task of extracting $G^*(\omega)$ and γ. Both $\chi(\omega)$ and $G^*(\omega)$ have real and imaginary parts, and thus $\chi(\omega)$, with only two knowns, is sufficient to extract three quantities, $G'(\omega)$, $G''(\omega)$, and γ. If γ is determined independently (see Subsection 4.2), a procedure has been developed to extract $G'(\omega)$ and $G''(\omega)$ by "inverting" eq 127.[313] Alternatively, one can assume a model for $G^*(\omega)$ and vary model parameters and γ to maximize the agreement

https://doi.org/10.1021/acs.chemrev.4c00138
Chem. Rev. XXXX, XXX, XXX−XXX

Table 4. List of Measured Viscosities

System	Value (Pa s)	Method	Ref
PGL-3; 180 mM NaCl	0.16	OT	Data from ref 312 reanalyzed in ref 318
150 mM NaCl	0.30		
115 mM NaCl	0.88		
75 mM NaCl	2.1		
UTP + pK10	0.1	MSD	81
UTP + pK50	0.2		
UTP + pK100	0.6		
pU10 + pK10	0.5		
pU10 + pK50	3		
pU10 + pK100	5		
pU50 + pK10	2		
pU50 + pK50	11		
pU50 + pK100	20		
UDP + pR10	6.5		
UDP + pR50	13		
UDP + pR100	41		
UTP + pR10	36		
UTP + pR50	65		
pU10 + pR10	53		
pU10 + pR50	118		
pU10 + pR100	235		
pU50 + pR10	198		
pU50 + pR50	>280		
pU50 + pR100	>280		
MaSp2; pH 8	0.16	Creep compliance	350
pH 7	0.11		
pH 6	13		
pH 5.5	410		
FUS LC	0.106	MSD	351
ProTα + H1	0.3	MSD	177
pK + heparin	0.30	OT	311
PolyPRM + heparin	0.53		
PolySH3 + polyPRM	3.7		
PolySH3 + lysozyme	10.1		
PolyPRM + heparin; 300 mM KCl	0.25		
400 mM KCl	0.21		
pK + heparin; 200 mg/mL Ficoll	0.42	OT	322
pK + 5 mM ATP	1.9	OT	135
pK + 10.2 mM ATP	1.7		
pK + 5 mM ATP; 150 mM KCl	0.65		
pK + 10.2 mM ATP; 150 mM KCl	0.89		
Protamine + 5 mM ATP	15.7		
Protamine + 10.2 mM ATP	18.6		
pU40 + $[RGPGG]_5$	0.19	OT	353
$[KGKGG]_5$	0.26		
$[RGSGG]_5$	0.4		
$[RPRPP]_5$	1.3		
$[RQRQQ]_5$	2.7		
$[RGRGG]_5$ or RG0Y	5		
$[RARAA]_5$	6		
RG1Y	8		
$[RGFGG]_5$	10		
RG3Y	13		
$[RGYGG]_5$ or RG5Y	40		
P granule	1	FRAP	9
$[RGRGG]_5$-dT40; 425 mM NaCl	0.89	MSD	325
325 mM NaCl	1.6		
175 mM NaCl	3		
100 mM NaCl	4		
25 mM NaCl	6		
PGL-3	5.4	MSD	317
PGL-3 + MEG-3	5.6		
MAP65 1 h	4.7	FRAP	326
2 h	5.8		
3 h	8.1		
4 h	7.8		
4.5 h	9.5		
FUS 1−267	1.2	MSD	319
Bik1	18.2		
LAF-1 RGG domain	11.1	Micropipette aspiration	188
NPM1	0.74	MSD	11
FIB1ΔC	11		
FIB1-GFP	100		
LAF-1 + 15/30 nt poly (A)	16.1	MSD	175
LAF-1 + 3000 nt poly (A)	60.9		
Whi3	6	MSD	65
Whi3 + BLN1 mRNA	17		
Whi3 + CLN3 mRNA	28		
Whi3 + BNI1 mRNA	34		
LAF-1; 250 mM NaCl	13	MSD	324
125 mM NaCl	51		
GAR-1ΔN	198		
DNA-sticky ends; 250 mM NaCl	24	MSD	127
500 mM NaCl	45		
1 M NaCl	88		
MMssMM	0.2	MSD	269
LLssLL	123		
FFssFF	856		

between the measured $\chi(\omega)$ and that predicted by eq 127.[318] It turns out that the Jeffreys model (eq 92a) for $G^*(\omega)$ works very well in reproducing the $\chi(\omega)$ data obtained by Jawerth et al.[312] for PGL-3 protein droplets.[318]

4.3.7. Other Experimental Methods. We briefly mention a few other methods for measuring viscosity or viscoelasticity. For a recent review, see ref 344. A straightforward method is to track the Brownian motion of a single microbead inside a protein droplet under an optical microscope. Because one can only record the lateral (x-y) position of the bead, the mean square displacement (MSD) of the two-dimensional Brownian motion

https://doi.org/10.1021/acs.chemrev.4c00138
Chem. Rev. XXXX, XXX, XXX−XXX

as a function of time is given by (see Supporting Information eq S140)

$$\mathrm{MSD}(t) = 4Dt \tag{128}$$

where D is the diffusion constant. After obtaining D from a linear fit, one can then find the viscosity from the Stokes−Einstein relation

$$D = \frac{k_B T}{6\pi\eta a} \tag{129}$$

where a is the radius of the bead. The direct relation between $\mathrm{MSD}(t)$ and η is

$$\eta = \frac{1}{6\pi a}\frac{4k_B T}{\mathrm{MSD}(t)/t} \tag{130}$$

A somewhat related method is fluorescence correlation spectroscopy.[345] Here one uses a confocal microscope and tracks the fluorescence intensity I of fluorescent microbeads in the small confocal volume. Because the beads diffuse in and out of the confocal volume, I fluctuates over time. In the simplest case, its normalized autocorrelation function is

$$\frac{\overline{I(t)I(0)}}{\overline{I^2}} = \frac{1}{1 + 4Dt/w^2} \tag{131}$$

where w is the radius of the Gaussian laser beam. (More sophisticated forms of this equation can be found in ref 346.) Again, one can find the viscosity from D using eq 129. Another similar method is fluorescence recovery after photobleaching (FRAP). From the radius of the bleached region and the recovery time, one can estimate the diffusion constant of the fluorescently labeled species, which typically is a macromolecule. The derived viscosity then represents the viscosity at the macromolecular scale instead of the macroscopic one (see Subsection 4.3.4).

For viscoelastic fluids, $\mathrm{MSD}(t)$ may deviate from a linear dependence on time. The time dependence can be used to determine the shear relaxation modulus:[347]

$$\hat{G}(s) \equiv \hat{G}(\omega)|_{s=i\omega} = \frac{1}{6\pi a}\frac{4k_B T}{s^2\widehat{\mathrm{MSD}}(s)} \tag{132}$$

where $\hat{G}(s)$ can be recognized as the Laplace transform of the shear relaxation modulus, and $\widehat{\mathrm{MSD}}(s)$ denotes the Laplace transform of the MSD. Instead of letting the bead undergo free Brownian motion, one can also trap it with an optical trap. The MSD will no longer grow indefinitely over time but reach an equilibrium value:

$$\mathrm{MSD}(\infty) = \frac{4k_B T}{\kappa_t} \tag{133}$$

where κ_t is the stiffness of the trap. Then[348,349]

$$\hat{G}(s) = \frac{\kappa_t}{6\pi a}\left[\frac{1}{s^2\widehat{\mathrm{msd}}(s)} - \frac{1}{s}\right] \tag{134a}$$

$$= \frac{\kappa_t}{6\pi a}\frac{\hat{A}(s)}{1 - s\hat{A}(s)} \tag{134b}$$

where $\widehat{\mathrm{msd}}(s)$ is the Laplace transform of the MSD after normalization by $\mathrm{MSD}(\infty)$, and $\hat{A}(s)$ is the Laplace transform of the normalized autocorrelation function of the bead position.

4.3.8. Experimental Data and Interpretations. Zero-shear viscosities have been measured for many condensates (Table 4 and Figure 20). The measured values range from ∼0.1 Pa s, for condensates of PGL-3,[312,318] 10-residue polylysine mixed with UTP,[81] silk protein MaSp2,[350] and FUS low-complexity domain,[351] to >280 Pa s or higher for condensates of 50- or 100-residue polyarginine mixed with 50-nucleotide polyuridine.[81] Zhang et al.[269] have obtained a viscosity as high as 856 Pa s for FFssFF droplets.

Recently Shen et al.[352] used super-resolution imaging to track the diffusion of a protein inside postsynaptic condensates, and found the diffusion to be anomalous [with $\mathrm{MSD}(t) \propto t^{\upsilon}$, where $\upsilon < 1$], due to the switching between a mobile state and a confined state. Such anomalous diffusion is also seen in molecular dynamics simulations of tetrapeptide condensates.[269]

The same two determinants, interaction strength and macromolecular density, noted for interfacial tension (Subsection 4.2.5) seem to apply to viscosity as well. For example, arginine is known to form much stronger cation-π and other interactions than lysine; the viscosities of polyarginine:polyuridine condensates are 2 orders of magnitude higher than those of polylysine:polyuridine condensates.[81] Similarly, the viscosities of protamine-ATP droplets are 10-fold higher than those of polylysine-ATP droplets.[135] On the other hand, for the series of binary condensates, pK:H, P:H, S:P, and S:L, that differed in the relative contents of disordered chains and folded domains, the order of viscosity followed that of macromolecular density, increasing from 0.3 Pa s to 10.1 Pa s, instead of the order of interaction strength. For this series, the interfacial tensions differ by only 2-fold but the viscosities differ by 30-fold, illustrating the tendency that viscosity often shows much greater variability than interfacial tension.

That both interaction strength and macromolecular density are determinants is also illustrated by viscosity differences between dense protein solutions and protein condensates. For example, lysozyme at 480 mg/mL has a relative viscosity of 153 (in reference to water) at 25 °C. In comparison, the relative viscosity of the S:L droplet is 11300. Clearly, the interactions between S and L molecules play a major part in this very high relative viscosity. Similarly, the self-diffusion constant of Ddx4 in the condensed phase is significantly slower than an inert probe of the same size.[174]

We now turn to viscoelasticity, which can manifest itself in many ways. As illustrated in Figure 22, viscoelastic materials have a finite shear relaxation time (τ_1). The shear relaxation times of a number of condensates have been reported.[135,311,318,322,332,353] For the pK:H, P:H, S:P, and S:L series, τ_1 ranged from 45 ms for pK:H to 396 ms for S:L, but did not seem to follow any order.[311] Alshareedah et al.[353] reported a 60 ms relaxation time for droplets formed by mixing an RG-repeat peptide ($[\mathrm{RGRGG}]_5$) with polyuridine, and an increase to 900 ms upon substituting the middle R with a Y. For PGL-3 protein droplets, the relaxation time of fresh samples was <10 ms.[318,332] Interestingly, over the course of 45 h the relaxation time increased to 11 min, suggesting that a possible characteristic of condensate aging is a significant slowdown in shear relaxation.[332]

The determinants for the shear relaxation time are much less well understood. According to models for associative polymers, τ_1 is dictated by the kinetics of macromolecular transient association and dissociation.[354,355] Accordingly, salt, by screening macromolecular electrostatic attraction, can be expected to decrease the shear relaxation time. Indeed, τ_1 of the P:H

https://doi.org/10.1021/acs.chemrev.4c00138
Chem. Rev. XXXX, XXX, XXX−XXX

condensate decreased from 125 to 56 ms and 36 ms, respectively, when the KCl concentration was raised from 150 mM to 300 and 400 mM.[311] A similar explanation can be given for the 10- to 20-fold longer shear relaxation times of protamine-ATP condensates than those of pK-ATP condensates, due to the stronger interactions of arginine over lysine.[135] We will cover another important aspect of viscoelasticity, namely shear thickening and shear thinning, in Subsection 4.4.3.

4.4. Droplet Fusion Dynamics

Similar to water droplets, biomolecular droplets have a tendency to fuse into a single larger droplet, driven by interfacial tension to reduce interfacial area. Fusion has been observed for various membraneless organelles, including P granules,[9] Cajal bodies,[356] nucleoli,[357] germline messenger RNP processing bodies,[358] stress granules,[296] and nuclear speckles.[359] Coalescence, merging, and joining are other terms used for fusion.

4.4.1. Viscocapillary Model of Droplet Fusion. The viscocapillary model has long been used for the fusion process between two viscous liquid droplets (Figure 24a). The model

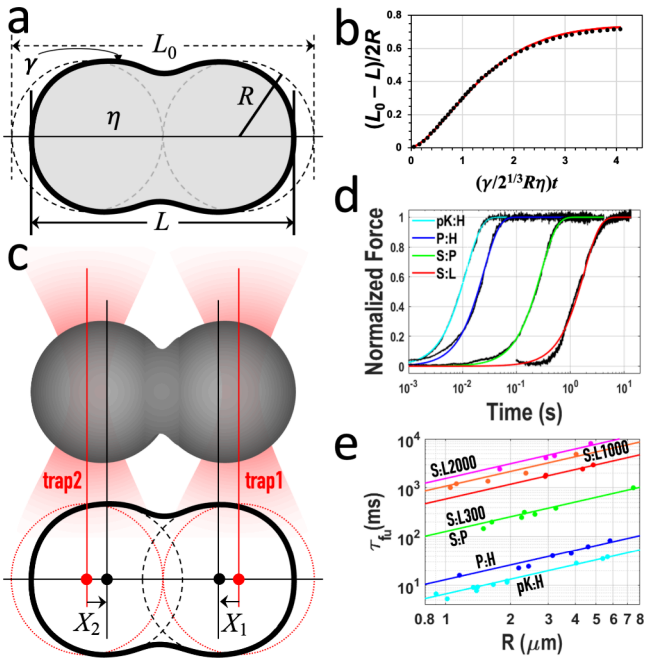

Figure 24. Measurement and analysis of droplet fusion data. (a) Viscocapillary model. (b) Fit of the numerical solution (circles) to a stretched exponential function (eq 135; curve). (c) Illustration of OT-directed fusion. (d) Fitting of OT-monitored fusion progress curves of four kinds of condensates to the stretched exponential function. (e) Proportional relation between fusion time and droplet radius, corresponding to lines with a slope of 1 in a log−log plot. Reproduced from ref 300 with permission. Copyright 2020 John Wiley and Sons.

assumes the Stokes equations (Supporting Information Section S1) for the viscous flow inside the fusion droplets and boundary conditions involving the interfacial tension (or capillarity; Supporting Information Section S3). Based on dimensional consideration, the viscocapillary ratio, η/γ, also known as the inverse capillary velocity, should provide a measure for the ratio, τ_{fu}/R, of the fusion time over the droplet radius. Fusion time has also been referred to as relaxation time.

The viscocapillary model has been solved numerically.[360,361] Ghosh and Zhou[300] found that the numerical result for the reduction in the edge-to-edge distance, L, over time can be fit to a stretched exponential function (Figure 24b):

$$\frac{L_0 - L}{L_0 - L_\infty} = 1 - e^{-(t/\tau_{fu})^\alpha} \tag{135}$$

where L_0 and L_∞ are the values of L at 0 and infinite times, the exponent $\alpha = 1.5$, and the fusion time is

$$\tau_{fu} = \frac{1.97R\eta}{\gamma} \tag{136}$$

The dependence of τ_{fu} on η and γ is what is expected from the just mentioned dimensional consideration. Here τ_{fu} is defined as the time at which the reduction in the edge-to-edge distance has reached a fraction of $1 - 1/e = 0.63$ of the full extent, and the coefficient 1.97 is simply based on fitting to the numerical result. We will refer to the ratio $1.97R/\tau_{fu}$ as the fusion speed and its inverse as the inverse fusion speed. Qualitatively, eq 136 indicates that fusion is driven by interfacial tension and retarded by condensate viscosity.

4.4.2. Measurement and Interpretation of Condensate Fusion Speed Data. The fusion process of biomolecular condensates can be monitored by time-lapse imaging.[9,11,65,74,81,93,177,310,326,327,357−359,362−364] Another way is to use dual-trap OT, which can directly trap two droplets and bring them into contact for fusion (Figure 24c).[63,73,135,287,300,322,325,365,366] The laser power needs to be turned to a minimal level as not to impede the fusion process. The force signal can then be fit to a stretched exponential like in eq 135 to determine the fusion time for droplets of a particular size (Figure 24d).

To further obtain the fusion speed, one needs to determine the fusion times for a range of droplet sizes. The relation between τ_{fu} and R is generally found to be linear (actually proportional;Figure 24e) (refs 9, 11, 65, 81, 93, 135, 177, 300, 310, 316, 317, 322, 325−327, 357−359, and 362−364). Inverse fusion speeds have been measured for many condensates (Table 5 and Figure 20). They span at least 6 orders of magnitude, from 4×10^{-4} s/μm for droplets formed polylysine and ATP[135] to 584 s/μm for nucleoli under ATP depletion.[357]

For FUS, a disease-associated mutation (G156E) slowed the fusion by ~3-fold; aging slowed the fusion of both wild-type and G156E droplets and also increased the fraction of droplets that did not fuse; after four hours of aging, no G156E droplets fused at all.[63] Very little is known about why sometimes fusion does not start; a recent study[251] suggested that a high condensate surface net charge could be a factor. When fusion does start, it appears that an increase in intermolecular interaction strength and/or extensiveness, e.g., by a mutation or aging, slows down fusion. This conclusion is in line with the observation that the fusion times of droplets formed by mixing arginine- or lysine-containing peptides with purine or pyrimidine homopolymeric RNAs follow the order of cation-π interaction strengths.[73,74] The strengthening of intermolecular interactions is expected to increase both interfacial tension and viscosity. If interfacial tension is the dominant factor over viscosity, then eq 136 predicts a speedup in fusion; conversely, a slowdown in fusion is predicted. Since the strengthening of intermolecular interaction appears to produce a slowdown in fusion, it looks like viscosity is the dominant factor over interfacial tension. This idea is also supported by the fact both viscosity and fusion speed show greater variability than interfacial tension.

https://doi.org/10.1021/acs.chemrev.4c00138
Chem. Rev. XXXX, XXX, XXX−XXX

Table 5. List of Inverse Fusion Speeds

System	Value (ms/μm)	Method	refs
pK + 100 mM ATP	0.4	OT	135
pK + 10.2 mM ATP	0.6		
pK + 5 mM ATP	1.1		
pK + 100 mM ATP; 150 mM KCl	0.6		
pK + 10.2 mM ATP; 150 mM KCl	0.7		
pK + 5 mM ATP; 150 mM KCl	1.3		
Protamine + 10.2 mM ATP	6.0		
Protamine + 5 mM ATP	6.7		
ProTα + H1	2.4	Imaging	177
$[RGRGG]_5$-dT40; 425 mM NaCl	2	OT	325
325 mM NaCl	2.4		
175 mM NaCl	2.9		
100 mM NaCl	3.2		
25 mM NaCl	3.4		
LAF-1 RGG domain	16	Imaging	310
SC-ADF3-SC	26	Imaging	316
FN-ADF3-FN	38		
Crys-ADF3-Crys	53		
CBM-ADF3-CBM	72		
LAF-1	120	Imaging	362
pK + UTP	12	Imaging	81
pR + UTP	144		
FUS	42	OT	63
FUS G156E	110		
FUS 2 h	94		
FUS G156E 2 h	260		
FUS 4 h	92		
MAP65	380	Imaging	326
pK + heparin	4.0	OT	322
PolySH3 + heparin	6.6	OT	300
PolySH3 + polyPRM	65		
PolySH3 + lysozyme (0.3 mM)	300		
PolySH3 + lysozyme (1 mM)	550		
PolySH3 + lysozyme (2 mM)	790		
PolySH3 + heparin; 300 mM KCl	2.4		unpublished
400 mM KCl	1.6		unpublished
pK + heparin; 100 mg/mL Ficoll	3.4	OT	322
200 mg/mL Ficoll	2.4		
MMssMM	0.8	OT	269
LLssLL	13		
FFssFF	618		
Poly(A) + PEG 55 °C	20	Imaging	363
35 °C	80		
25 °C	500		
Bubble fusing with dilute phase	80		
Bubbles 35 °C	140		
20 °C	830		
BTB-FUS IDR	1080	Imaging	364
PGL-3	250	Imaging	317
PGL-3 + MEG-3	1200		
poly(U) + $[KGKGG]_5$	2.8	OT	73
poly(U) + $[RGRGG]_5$	60		
poly(A) + $[KGKGG]_5$	200		
poly(A) + $[RGRGG]_5$	350		
poly(U) + FUS LCD	85		
poly(A) + FUS LCD	915		
poly(U) + FUS RGG3	130		
poly(A) + FUS RGG3	1950		
FUS	190	OT and imaging	366
FUS; 25 mg/mL PEG	2122		
Whi3 + BLN1 RNA	8000	Imaging	65
Whi3 + CLN3 RNA	14000		
hnRNPA1	8300	OT	365
hnRNPA1 ΔRAC1	6400		
hnRNPA1 D214V	16000		
DNA-sticky ends; 250 mM NaCl	9800	Imaging	127
500 mM NaCl	9900		
1 M NaCl	11900		
DNA-4 nt sticky ends	900	Imaging	327
DNA-12 nt sticky ends	26300		
FUS WT	93	OT	287
FUS G $\rightarrow$ A	32900		
RNA + $(KGG)_9$	57	Imaging	93
RNA + $(RGG)_4$	840		
RNA + K_9	6900		
RNA + R_9	220000		
P granule	2000	Imaging	9
NPM1	300	Imaging	11
NPM1-labeled GC	30000		
FIB1ΔC	500		
FIB1	16000		
FIB1-labeled DFC	80000		
Nuclear speckle	100800	Imaging	359
grP-body	125000	Imaging	358
Nucleolus + ATP	46100	Imaging	357
Nucleolus − ATP	584000		

However, the determinants of fusion speed are much more complex. For example, when a subset of glycine residues in the prion-like domain of FUS was mutated into alanines (G→A), fusion was slowed by 350-fold.[287] Interaction strength is unlikely affected significantly by the mutations, since the threshold concentration for phase separation changed very little. To uncover additional determinants, Ghosh and Zhou[300] used OT to measure the fusion speeds of the series of binary condensates, p*K*:H, P:H, S:P, and S:L, that differed in the relative contents of disordered chains and folded domains (Figure 24e). As the content of folded domains increased, the inverse fusion speeds rose by two orders of magnitude, from 4×10^{-3} s/μm to 0.3 s/μm. So it seems that folded domains significantly slow down droplet fusion. Indeed, when the level of the folded protein, L, was increased in preparing the S:L droplets, from a molar ratio of 300:20 to 2000:20, the inverse fusion speed was further increased to 0.8 s/μm.

Why do folded domains tend to slow down fusion relative to IDPs? Ghosh and Zhou provided the following explanation. As noted in Subsection 3.2.3, compared with IDPs, folded domains are much harder to form contact clusters. Conversely, the folded domains break up contact clusters less easily and hence more

https://doi.org/10.1021/acs.chemrev.4c00138
Chem. Rev. XXXX, XXX, XXX−XXX

slowly. In essence, IDPs can form and break a cluster of contacts one contact at a time, whereas folded domains may have to do so all at once. In the fusion process, protein molecules have to break and reform contacts constantly. For folded domains, these events are harder and thus occur more slowly, thereby leading to slower fusion. This explanation also accounts for the slowdown in fusion by the FUS G→A mutations, as the flexible glycine residue more easily allows intermolecular contacts to break and reform.

4.4.3. Simultaneous Measurement of Interfacial Tension, Viscosity, and Fusion Speed Reveals Shear Thickening and Shear Thinning. The viscocapillary model, as captured by a relation similar to eq 136, has been widely used to deduce interfacial tension from viscosity and fusion speed[9,81,177,310,317,324−327] as already noted in Subsection 4.2.5 or otherwise interpret fusion speed data.[357−359] Given the preponderance of evidence indicating that biomolecular condensates are viscoelastic, the applicability of the viscocapillary model is questionable. Testing it requires the measurement of three properties: interfacial tension, viscosity, and fusion speed on the same condensate. Before 2020, there was only one such set of data that we are aware of, measured by Feric et al.[11] on nucleophosmin droplets. The results were: $\gamma = 0.8$ pN/μm, $\eta = 0.74$ Pa s, and inverse fusion speed = 0.3 s/μm. The viscocapillary model predicts an inverse fusion speed of 0.9 s/μm, which is three times higher than the measured.

To systematically test the viscocapillary model, Ghosh et al.[311] used OT to complete the measurements of interfacial tension (Subsection 4.2.5) and viscoelasticity (Subsection 4.3.8) along with fusion speed (Figure 24e) for the series of binary condensates that differed in the relative contents of disordered chains and folded domains. By comparing the measured fusion time against that (τ_{fu}^{N}) predicted by eq 136 using the measured interfacial tension and zero-shear viscosity, they found significant discrepancies, in both directions (Figure 25a). The fusion speed is overpredicted for condensates formed by a folded protein or proteins with folded proteins; the converse is true for condensates formed by disordered chains only (see also Figure 20). Correspondingly, the effective viscosity operating in the fusion process is either higher or lower than the zero-shear viscosity, implicating shear thickening and shear thinning, respectively.

To explain the apparent shear thickening and shear thinning behaviors, Ghosh et al. took hints from associative polymers.[355,367,368] Under steady shear, polymers generally exhibit shear thinning at high shear rates, but some associative polymers also exhibit shear thickening at intermediate shear rates. While droplet fusion is a dynamic process as opposed to being at a steady state, Ghosh et al. defined $1/\tau_{fu}^{*}$, where $\equiv (\tau_{fu}\tau_{fu}^{N})^{1/2}$, as an effective steady shear rate. The shear-thickening droplets fall on the side with $\tau_1/\tau_{fu}^{*} < 1$ whereas the shear-thinning droplets fall on the side with $\tau_1/\tau_{fu}^{*} > 1$ (Figure 25a). It looks as if that, in the former droplets, the shear generated during fusion strengthens the interaction networks and thereby increases the effective viscosity. In contrast, in the latter droplets, the shear induces the alignment of protein chains and hence decreases the effective viscosity.

Interfacial tension, viscosity, and fusion speed data are now also available for the LAF-1 RGG domain: $\gamma = 170$ pN/μm, $\eta = 11.1$ Pa s, and inverse fusion speed = 0.016 s/μm.[188,310] The latter is to be compared with a value of 0.065 s/μm predicted by the viscocapillary model, implicating 4-fold shear thinning.

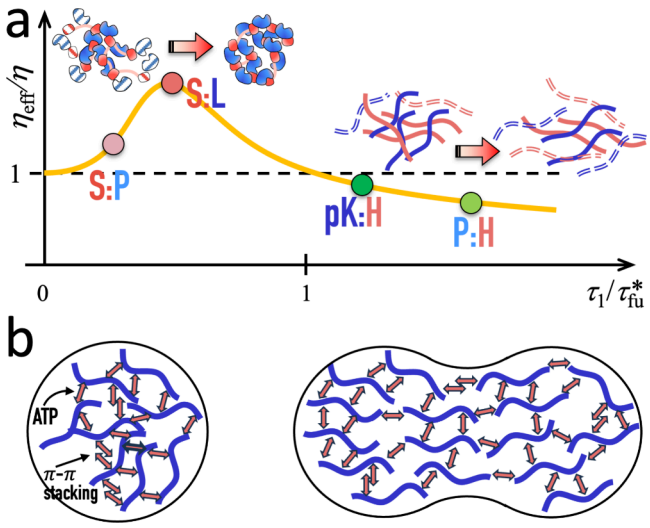

Figure 25. Shear thickening and shear thinning exhibited during condensate fusion. (a) A tentative model for explaining how shear thickening arises for some condensates and shear thinning arises for many other condensates. $\eta_{eff}/\eta \equiv \tau_{fu}/\tau_{fu}^{N}$; $\tau_{fu}^{N} \equiv 1.97R\eta/\gamma$ is predicted fusion time by eq 136, which assumes the condensate as a Newtonian fluid; and $\tau_{fu}^{*} \equiv (\tau_{fu}\ \tau_{fu}^{N})^{1/2}$. Reproduced from ref 311. Copyright 2021 the original authors. (b) Model illustrating how extreme shear thinning arises in bIDP-ATP droplets. Reproduced from ref 135. Copyright 2024 American Chemical Society.

Recently, data from droplets formed by mixing bIDPs with ATP revealed extreme shear thinning, with the effective viscosity manifested in droplet fusion over 100-fold lower than the measured zero-shear viscosity.[135] The explanation is that ATP mediates condensate formation by bridging between IDP chains, and these bridges quickly break and reform during droplet fusion (Figure 25b).

The foregoing results clearly demonstrate the inapplicability of the viscocapillary model to condensate fusion. As noted in Subsection 4.2.5, using the viscocapillary model has produced interfacial tensions, including one at 1600 pN/μm, that are far outside the range, 1 to 250 pN/μm, of measured values. In addition, interfacial tensions deduced from the viscocapillary model led Taylor et al.[324] to attribute interfacial tension instead of viscosity as the dominant factor for a 75-fold difference in fusion speed between Whi3 and LAF-1, contradicting the conclusion drawn in Subsection 4.4.2 based on the observation that strengthening of intermolecular interactions typically leads to an increase in viscosity along with a slowdown in fusion.

4.4.4. Shear Thinning Allows Condensates to Remain Dynamic Despite High Viscosity. It thus appears that shear thinning may be very common in the fusion processes of IDP condensates. For bIDP-ATP condensates, it has been suggested that their shear thinning has physiological implications.[135] It allows these condensates to undergo rapid fusion and thus remain extremely dynamic despite the high macroscopic viscosity inside the condensates. The fusion of nucleoli was slowed by 10-fold upon ATP depletion.[357] Similarly, normal stress granules readily fused but granules in ATP-depleted cells did not.[296] An active (i.e., energy-driven) process may be involved, but ATP-mediated shear thinning could well play a role.

https://doi.org/10.1021/acs.chemrev.4c00138
Chem. Rev. XXXX, XXX, XXX−XXX

5. CONCLUDING REMARKS

Biomolecular condensates are where basic physics meets rich biology. Theoretical models, molecular simulations, *in vitro* reconstitutions, and direct *in vivo* observations together have helped in dissecting the complex behaviors of biomolecular condensates and reaching physical understanding of their properties. The first quarter of the 20th century laid the foundation of what is now called modern physics. It looks like the first quarter of the 21st century is destined to usher in modern biology. We close this review by making the following remarks.

All Attractive Interactions Contribute to Phase Separation

As we emphasized throughout this review, phase separation is driven by intermolecular attraction, and all attractive interactions contribute to phase separation. In biomolecular systems, attraction comes in the form of hydrophobic interactions, $\pi-\pi$, cation$-\pi$, and amino$-\pi$ interactions, hydrogen bonds, and interactions between opposite charges. To keep condensates in a liquid-like state, intermolecular attraction needs to be in a moderate range of strengths; if it is weak, phase separation would not occur, but if it is too strong, condensates would turn solid-like.

Different amino acids and nucleotides can participate in different types of attractive interactions or do so at different strengths. By tuning sequences and compositions, condensates can achieve the desired material state. External factors such as salt and pH can also modulate interaction strengths, adding to the arsenal by which biomolecular condensates can modulate their phase-equilibrium and material properties.

All-Atom Molecular Dynamics Simulations Are Needed to Make Physically Realistic and Quantitatively Accurate Predictions of Condensate Properties

Theoretical models and coarse-grained simulations have greatly contributed to our conceptual and qualitative understanding of phase-equilibrium and material properties of biomolecular condensates. Recently, all-atom molecular dynamics simulations in explicit solvent are becoming capable of predicting thermodynamic and dynamic properties that can be directly compared with experimental measurements. In that regard coarse-grained simulations are limiting—e.g., they underpredict viscosities by several orders of magnitude, due to the smoothening of energy surfaces (which speeds up simulations).[217,225,246,305,336] Such predictions could result in misleading physical pictures. In contrast, all-atom molecular dynamics simulations have the potential to provide physical realism. It is now even possible to directly use experimental data for phase-equilibrium and material properties to refine all-atom force fields for higher quantitative accuracy. Theoretical models and coarse-grained simulations still have important roles in other understudied areas (see below).

IDPs and Folded Proteins or Folded Domains Behave Differently in Phase Separation

Folded domains and IDPs behave very differently in their drive of phase separation and in how they dictate condensate material properties, a point first raised a few years ago.[44] As we have noted, IDPs are more able than folded domains to drive phase separation because: (1) all residues of an IDP, as opposed to only surface residues of a folded domain, can participate in interprotein interactions; (2) an IDP molecule can more easily reach its neighbors due to its extended conformations; (3) IDP molecules can readily adapt to each other to form contact clusters. On the other hand, electrostatic effects on the surface of a folded domain may be amplified compared to an IDP. For the same reason, the effect of a surface residue on a folded domain may more depend on what its neighbors are and hence be more context-dependent. Not only thermodynamic but also dynamic properties may be different between folded domains and IDPs. In particular, IDPs can more easily break and reform intermolecular contacts and therefore may have the tendency to exhibit shear thinning during condensate fusion.

We emphasize these differences partly because we feel that while IDPs deserve overwhelming attention in the study of condensates, it should not be to the exclusion of folded domains, as many phase-separating proteins contain folded domains.

Biomolecular Condensates Are Viscoelastic, and the Viscocapillary Model Should Be Abandoned for Interpreting Fusion Data

We emphasize that the viscocapillary model treats condensates as purely viscous. It is now widely recognized that biomolecular condensates are viscoelastic. Viscoelasticity manifests itself in many ways. In particular, during the fusion process, condensates can exhibit enormous shear thinning (and possibly shear thickening).

Ironically, while acknowledging viscoelasticity, many still use the viscocapillary model to interpret data on fusion speed, specifically to deduce interfacial tension. This practice has led to interfacial tension values that are far outside the measured range, and to misleading mechanistic interpretations. So stop interpreting the inverse fusion speed as the ratio of viscosity to interfacial tension!

Theoretical Models Are Needed to Provide Foundational Understanding of Multiphase Organization, Gelation, And Aging of Condensates

Rather than a single homogeneous dense phase, multicomponent condensates, both inside cells and in *in vitro* reconstitutions, often show multiphase organization.[11,74,77,80,95,125,146,239,248,296,369−379] Multiphase coexistence has also been studied by coarse-grained simulations[11,74,80,84,211,213,227,228,244,248,370,372,380,381] and theoretically.[381−383] For a recent review of simulations and theoretical models, see ref 384. Multiphase organization has been referred to as a second phase transition, occurring inside condensates formed by the first phase transition, i.e., phase separation.[146,381] Whereas the first phase transition is driven by the overall attraction among all the molecular components, the second phase transition, i.e., demixing among the components in the dense phase, can be driven by a disparity in the attractive strengths among the components.[381] Disparities in other properties, including incompatibility between disordered chains and folded domains[146] and mismatch in charge patterns along IDP chains,[383] may also drive demixing. More theoretical studies will help further delineate the general principles.

Instead of liquid-like droplets, many condensates appear immediately as amorphous aggregates (Figure 2c) or gels.[18,103,114,135,146,268,300,385−387] Over time many liquid-like condensates turn into solid-like gels, a process referred as aging or maturation.[10,62−64,72,82,260,261,326,332,365,376,379,388] Gelation and aging have been studied by coarse-grained simulations[147,225,226,336,389] Theoretical models will be very useful for providing a conceptual framework. Lastly we take note of growing efforts in engineering biomolecular condensates.[101,128,238,245,288,390−393]

https://doi.org/10.1021/acs.chemrev.4c00138
Chem. Rev. XXXX, XXX, XXX−XXX

ASSOCIATED CONTENT

Supporting Information

The Supporting Information is available free of charge at https://pubs.acs.org/doi/10.1021/acs.chemrev.4c00138.

Additional mathematical equations that provide the background and derivation for some of the equations cited in the main text (PDF)

AUTHOR INFORMATION

Corresponding Author

Huan-Xiang Zhou − *Department of Chemistry and Department of Physics, University of Illinois Chicago, Chicago, Illinois 60607, United States;* orcid.org/0000-0001-9020-0302; Email: hzhou43@uic.edu

Authors

Divya Kota − *Department of Chemistry, University of Illinois Chicago, Chicago, Illinois 60607, United States*

Sanbo Qin − *Department of Chemistry, University of Illinois Chicago, Chicago, Illinois 60607, United States*

Ramesh Prasad − *Department of Chemistry, University of Illinois Chicago, Chicago, Illinois 60607, United States*

Complete contact information is available at: https://pubs.acs.org/10.1021/acs.chemrev.4c00138

Author Contributions

CRediT: **Huan-Xiang Zhou** conceptualization, data curation, formal analysis, funding acquisition, investigation, methodology, project administration, supervision, visualization, writing-original draft, writing-review & editing; **Divya Kota** data curation, validation; **Sanbo Qin** data curation, validation, visualization; **Ramesh Prasad** data curation, validation.

Notes

The authors declare no competing financial interest.

Biographies

Huan-Xiang Zhou received his PhD from Drexel University in 1988. He did postdoctoral work at the National Institutes of Health with Attila Szabo. After faculty appointments at Hong Kong University of Science and Technology, Drexel University, and Florida State University, he moved in 2017 to the University of Illinois Chicago, where he is Professor of Chemistry and Physics and holds an LAS Science endowed chair. His group currently does theoretical, computational, and experimental research on thermodynamic and dynamic properties of phase-separated biomolecular condensates, on membrane association of intrinsically disordered proteins, on structures and pathways of the self-assemblies of amyloid-β and other amyloidogenic proteins, and on functional mechanisms of glutamate-receptor ion channels.

Divya Kota received her PhD from South Dakota School of Mines and Technology in 2020. After postdoctoral work, she is now a visiting research assistant professor at University of Illinois Chicago. Her experimental research focuses on thermodynamic and dynamic properties of biomolecular condensates.

Sanbo Qin received his PhD from University of Chinese Academy of Sciences in 2006. He did postdoctoral work at Florida State University and is now a research assistant professor at University of Illinois Chicago developing computational methods for biomolecular interactions.

Ramesh Prasad received his PhD from Jadavpur University, India, in 2018. He has been a postdoctoral researcher at University of Illinois Chicago since 2019, working on a range of computational biophysics problems including phase separation, ionotropic glutamate receptors, and structural biology of mycobacterial proteins.

ACKNOWLEDGMENTS

We thank Hue Sun Chan, Kresten Lindorff-Larsen, Tanja Mittag, Rohit Pappu, Ben Schuler, Giulio Tesei, and Shi Zheng for reading the manuscript. This work was supported in part by Grant GM118091 from the National Institutes of Health.

REFERENCES

(1) Hyman, A. A.; Weber, C. A.; Julicher, F. Liquid-Liquid Phase Separation in Biology. *Annu. Rev. Cell Dev. Biol.* **2014**, *30*, 39−58.

(2) Banani, S. F.; Lee, H. O.; Hyman, A. A.; Rosen, M. K. Biomolecular Condensates: Organizers of Cellular Biochemistry. *Nat. Rev. Mol. Cell Biol.* **2017**, *18*, 285−298.

(3) Shin, Y.; Brangwynne, C. P. Liquid Phase Condensation in Cell Physiology and Disease. *Science* **2017**, *357*, No. eaaf4382.

(4) Boeynaems, S.; Alberti, S.; Fawzi, N. L.; Mittag, T.; Polymenidou, M.; Rousseau, F.; Schymkowitz, J.; Shorter, J.; Wolozin, B.; Van Den Bosch, L.; et al. Protein Phase Separation: A New Phase in Cell Biology. *Trends Cell. Biol.* **2018**, *28*, 420−435.

(5) Alberti, S.; Gladfelter, A.; Mittag, T. Considerations and Challenges in Studying Liquid-Liquid Phase Separation and Biomolecular Condensates. *Cell* **2019**, *176*, 419−434.

(6) Ghosh, R. P.; Meyer, B. J. Spatial Organization of Chromatin: Emergence of Chromatin Structure During Development. *Annu. Rev. Cell Dev. Biol.* **2021**, *37*, 199−232.

(7) Lyon, A. S.; Peeples, W. B.; Rosen, M. K. A Framework for Understanding the Functions of Biomolecular Condensates across Scales. *Nat. Rev. Mol. Cell Biol.* **2021**, *22*, 215−235.

(8) Ripin, N.; Parker, R. Formation, Function, and Pathology of RNP Granules. *Cell* **2023**, *186*, 4737−4756.

(9) Brangwynne, C. P.; Eckmann, C. R.; Courson, D. S.; Rybarska, A.; Hoege, C.; Gharakhani, J.; Julicher, F.; Hyman, A. A. Germline P Granules Are Liquid Droplets That Localize by Controlled Dissolution/Condensation. *Science* **2009**, *324*, 1729−1732.

(10) Molliex, A.; Temirov, J.; Lee, J.; Coughlin, M.; Kanagaraj, A. P.; Kim, H. J.; Mittag, T.; Taylor, J. P. Phase Separation by Low Complexity Domains Promotes Stress Granule Assembly and Drives Pathological Fibrillization. *Cell* **2015**, *163*, 123−133.

(11) Feric, M.; Vaidya, N.; Harmon, T. S.; Mitrea, D. M.; Zhu, L.; Richardson, T. M.; Kriwacki, R. W.; Pappu, R. V.; Brangwynne, C. P. Coexisting Liquid Phases Underlie Nucleolar Subcompartments. *Cell* **2016**, *165*, 1686−1697.

(12) Strom, A. R.; Emelyanov, A. V.; Mir, M.; Fyodorov, D. V.; Darzacq, X.; Karpen, G. H. Phase Separation Drives Heterochromatin Domain Formation. *Nature* **2017**, *547*, 241−245.

(13) Larson, A. G.; Elnatan, D.; Keenen, M. M.; Trnka, M. J.; Johnston, J. B.; Burlingame, A. L.; Agard, D. A.; Redding, S.; Narlikar, G. J. Liquid Droplet Formation By HP1alpha Suggests a Role for Phase Separation in Heterochromatin. *Nature* **2017**, *547*, 236−240.

(14) Cho, W. K.; Spille, J. H.; Hecht, M.; Lee, C.; Li, C.; Grube, V.; Cisse, I. I. Mediator and RNA Polymerase II Clusters Associate in Transcription-Dependent Condensates. *Science* **2018**, *361*, 412−415.

(15) Hondele, M.; Sachdev, R.; Heinrich, S.; Wang, J.; Vallotton, P.; Fontoura, B. M. A.; Weis, K. DEAD-Box ATPases Are Global Regulators of Phase-Separated Organelles. *Nature* **2019**, *573*, 144−148.

(16) Belott, C.; Janis, B.; Menze, M. A. Liquid-Liquid Phase Separation Promotes Animal Desiccation Tolerance. *Proc. Natl. Acad. Sci. U.S.A.* **2020**, *117*, 27676−27684.

(17) Daneshvar, K.; Ardehali, M. B.; Klein, I. A.; Hsieh, F. K.; Kratkiewicz, A. J.; Mahpour, A.; Cancelliere, S. O. L.; Zhou, C.; Cook, B. M.; Li, W.; et al. lncRNA DIGIT and BRD3 Protein Form Phase-

Separated Condensates to Regulate Endoderm Differentiation. *Nat. Cell Biol.* **2020**, *22*, 1211−1222.
(18) Fuller, G. G.; Han, T.; Freeberg, M. A.; Moresco, J. J.; Ghanbari Niaki, A.; Roach, N. P.; Yates, J. R., 3rd; Myong, S.; Kim, J. K. RNA Promotes Phase Separation of Glycolysis Enzymes into Yeast G Bodies in Hypoxia. *eLife* **2020**, *9*, No. e48480.
(19) Gallego, L. D.; Schneider, M.; Mittal, C.; Romanauska, A.; Gudino Carrillo, R. M.; Schubert, T.; Pugh, B. F.; Köhler, A. Phase Separation Directs Ubiquitination of Gene-Body Nucleosomes. *Nature* **2020**, *579*, 592−597.
(20) Guseva, S.; Milles, S.; Jensen, M. R.; Salvi, N.; Kleman, J. P.; Maurin, D.; Ruigrok, R. W. H.; Blackledge, M. Measles Virus Nucleo- and Phosphoproteins Form Liquid-like Phase-Separated Compartments that Promote Nucleocapsid Assembly. *Sci. Adv.* **2020**, *6*, No. eaaz7095.
(21) Ladouceur, A. M.; Parmar, B. S.; Biedzinski, S.; Wall, J.; Tope, S. G.; Cohn, D.; Kim, A.; Soubry, N.; Reyes-Lamothe, R.; Weber, S. C. Clusters of Bacterial RNA Polymerase Are Biomolecular Condensates That Assemble Through Liquid-Liquid Phase Separation. *Proc. Natl. Acad. Sci. U.S.A.* **2020**, *117*, 18540−18549.
(22) Oshidari, R.; Huang, R.; Medghalchi, M.; Tse, E. Y. W.; Ashgriz, N.; Lee, H. O.; Wyatt, H.; Mekhail, K. DNA Repair by Rad52 Liquid Droplets. *Nat. Commun.* **2020**, *11*, 695.
(23) Claeys Bouuaert, C.; Pu, S.; Wang, J.; Oger, C.; Daccache, D.; Xie, W.; Patel, D. J.; Keeney, S. DNA-Driven Condensation Assembles The Meiotic DNA Break Machinery. *Nature* **2021**, *592*, 144−149.
(24) Feric, M.; Demarest, T. G.; Tian, J.; Croteau, D. L.; Bohr, V. A.; Misteli, T. Self-Assembly of Multi-Component Mitochondrial Nucleoids via Phase Separation. *EMBO J.* **2021**, *40*, No. e107165.
(25) Liu, X. M.; Ma, L.; Schekman, R. Selective Sorting of MicroRNAs into Exosomes by Phase-Separated YBX1 Condensates. *eLife* **2021**, *10*, No. e71982.
(26) Shen, C.; Li, R.; Negro, R.; Cheng, J.; Vora, S. M.; Fu, T. M.; Wang, A.; He, K.; Andreeva, L.; Gao, P.; et al. Phase Separation Drives RNA Virus-Induced Activation of the NLRP6 Inflammasome. *Cell* **2021**, *184*, 5759−5774.
(27) Tibble, R. W.; Depaix, A.; Kowalska, J.; Jemielity, J.; Gross, J. D. Biomolecular Condensates Amplify mRNA Decapping by Biasing Enzyme Conformation. *Nat. Chem. Biol.* **2021**, *17*, 615−623.
(28) Boyd-Shiwarski, C. R.; Shiwarski, D. J.; Griffiths, S. E.; Beacham, R. T.; Norrell, L.; Morrison, D. E.; Wang, J.; Mann, J.; Tennant, W.; Anderson, E. N.; et al. WNK Kinases Sense Molecular Crowding and Rescue Cell Volume via Phase Separation. *Cell* **2022**, *185*, 4488−4506.
(29) Goldberger, O.; Szoke, T.; Nussbaum-Shochat, A.; Amster-Choder, O. Heterotypic Phase Separation of Hfq Is Linked to Its Roles as an RNA Chaperone. *Cell Rep.* **2022**, *41*, 111881.
(30) Jack, A.; Kim, Y.; Strom, A. R.; Lee, D. S. W.; Williams, B.; Schaub, J. M.; Kellogg, E. H.; Finkelstein, I. J.; Ferro, L. S.; Yildiz, A.; et al. Compartmentalization of Telomeres Through DNA-Scaffolded Phase Separation. *Dev. Cell* **2022**, *57*, 277−290.
(31) Jeong, J.; Lee, J. H.; Carcamo, C. C.; Parker, M. W.; Berger, J. M. DNA-Stimulated Liquid-Liquid Phase Separation by Eukaryotic Topoisomerase II Modulates Catalytic Function. *eLife* **2022**, *11*, No. e81786.
(32) Kang, J. Y.; Wen, Z.; Pan, D.; Zhang, Y.; Li, Q.; Zhong, A.; Yu, X.; Wu, Y. C.; Chen, Y.; Zhang, X.; et al. LLPS of FXR1 Drives Spermiogenesis By Activating Translation Of Stored mRNAs. *Science* **2022**, *377*, No. eabj6647.
(33) Mondal, S.; Narayan, K.; Botterbusch, S.; Powers, I.; Zheng, J.; James, H. P.; Jin, R.; Baumgart, T. Multivalent Interactions between Molecular Components Involved in Fast Endophilin Mediated Endocytosis Drive Protein Phase Separation. *Nat. Commun.* **2022**, *13*, 5017.
(34) Shao, W.; Bi, X.; Pan, Y.; Gao, B.; Wu, J.; Yin, Y.; Liu, Z.; Peng, M.; Zhang, W.; Jiang, X.; et al. Phase Separation of RNA-Binding Protein Promotes Polymerase Binding and Transcription. *Nat. Chem. Biol.* **2022**, *18*, 70−80.
(35) Shi, B.; Heng, J.; Zhou, J.-Y.; Yang, Y.; Zhang, W.-Y.; Koziol, M. J.; Zhao, Y.-L.; Li, P.; Liu, F.; Yang, Y.-G. Phase Separation of Ddx3xb Helicase Regulates Maternal-to-Zygotic Transition in Zebrafish. *Cell Res.* **2022**, *32*, 715−728.
(36) Gallo, R.; Rai, A. K.; McIntyre, A. B. R.; Meyer, K.; Pelkmans, L. DYRK3 Enables Secretory Trafficking by Maintaining the Liquid-Like State of ER Exit Sites. *Dev. Cell* **2023**, *58*, 1880−1897.
(37) Ji, D.; Shao, C.; Yu, J.; Hou, Y.; Gao, X.; Wu, Y.; Wang, L.; Chen, P. FOXA1 Forms Biomolecular Condensates That Unpack Condensed Chromatin to Function as a Pioneer Factor. *Mol. Cell* **2024**, *84*, 244−260.
(38) Li, Z.; Shen, Q.; Dai, Y.; Anderson, A. P.; Iburg, M.; Lin, R.; Zimmer, B.; Meyer, M. D.; You, L.; Chilkoti, A.; et al. Spatial Organization of Gas Vesicles is Governed by Phase-separable GvpU. *bioRxiv* **2023**, DOI: 10.1101/2023.06.01.543273, (acccessed 2024−02−15).
(39) Ye, S.; Latham, A. P.; Tang, Y.; Hsiung, C.-H.; Chen, J.; Luo, F.; Liu, Y.; Zhang, B.; Zhang, X. Micropolarity Governs the Structural Organization of Biomolecular Condensates. *Nat. Chem. Biol.* **2024**, *20*, 443−451.
(40) Alberti, S.; Dormann, D. Liquid-Liquid Phase Separation in Disease. *Annu. Rev. Genet.* **2019**, *53*, 171−194.
(41) Zbinden, A.; Pérez-Berlanga, M.; De Rossi, P.; Polymenidou, M. Phase Separation and Neurodegenerative Diseases: A Disturbance in the Force. *Dev. Cell* **2020**, *55*, 45−68.
(42) Gao, G.; Sumrall, E. S.; Pitchiaya, S.; Bitzer, M.; Alberti, S.; Walter, N. G. Biomolecular Condensates in Kidney Physiology and Disease. *Nat. Rev. Nephrol.* **2023**, *19*, 756−770.
(43) Brangwynne, C. P.; Tompa, P.; Pappu, R. V. Polymer Physics of Intracellular Phase Transitions. *Nat. Phys.* **2015**, *11*, 899−904.
(44) Zhou, H. X.; Nguemaha, V.; Mazarakos, K.; Qin, S. Why Do Disordered and Structured Proteins Behave Differently in Phase Separation? *Trends Biochem. Sci.* **2018**, *43*, 499−516.
(45) Choi, J.-M.; Holehouse, A. S.; Pappu, R. V. Physical Principles Underlying the Complex Biology of Intracellular Phase Transitions. *Annu. Rev. Biophys.* **2020**, *49*, 107−133.
(46) Pappu, R. V.; Cohen, S. R.; Dar, F.; Farag, M.; Kar, M. Phase Transitions of Associative Biomacromolecules. *Chem. Rev.* **2023**, *123*, 8945−8987.
(47) Jülicher, F.; Weber, C. A. Droplet Physics and Intracellular Phase Separation. *Annu. Rev. Condens. Matter Phys.* **2024**, *15*, 237−261.
(48) Ghosh, A.; Mazarakos, K.; Zhou, H. X. Three Archetypical Classes of Macromolecular Regulators of Protein Liquid-Liquid Phase Separation. *Proc. Natl. Acad. Sci. U.S.A.* **2019**, *116*, 19474−19483.
(49) Flory, P. J. Thermodynamics of High Polymer Solutions. *J. Chem. Phys.* **1942**, *10*, 51−61.
(50) Tanaka, T.; Ishimoto, C.; Chylack, L. T., Jr Phase Separation of a Protein-Water Mixture in Cold Cataract in the Young Rat Lens. *Science* **1977**, *197*, 1010−1012.
(51) Tombs, M. P.; Newsom, B. G.; Wilding, P. Protein Solubility: Phase Separation in Arachin-Salt-Water Systems. *Int. J. Pept. Protein Res.* **1974**, *6*, 253−277.
(52) Siezen, R. J.; Fisch, M. R.; Slingsby, C.; Benedek, G. B. Opacification of gamma-Crystallin Solutions from Calf Lens in Relation to Cold Cataract Formation. *Proc. Natl. Acad. Sci. U.S.A.* **1985**, *82*, 1701−1705.
(53) Thomson, J. A.; Schurtenberger, P.; Thurston, G. M.; Benedek, G. B. Binary Liquid Phase Separation and Critical Phenomena in a Protein/Water Solution. *Proc. Natl. Acad. Sci. U.S.A.* **1987**, *84*, 7079−7083.
(54) Siezen, R. J.; Wu, E.; Kaplan, E. D.; Thomson, J. A.; Benedek, G. B. Rat Lens gamma-Crystallins. Characterization of the Six Gene Products and Their Spatial and Temporal Distribution Resulting from Differential Synthesis. *J. Mol. Biol.* **1988**, *199*, 475−490.
(55) Broide, M. L.; Berland, C. R.; Pande, J.; Ogun, O. O.; Benedek, G. B. Binary-Liquid Phase Separation of Lens Protein Solutions. *Proc. Natl. Acad. Sci. U.S.A.* **1991**, *88*, 5660−5664.
(56) Pande, A.; Pande, J.; Asherie, N.; Lomakin, A.; Ogun, O.; King, J. A.; Lubsen, N. H.; Walton, D.; Benedek, G. B. Molecular Basis of a Progressive Juvenile-Onset Hereditary Cataract. *Proc. Natl. Acad. Sci. U.S.A.* **2000**, *97*, 1993−1998.

https://doi.org/10.1021/acs.chemrev.4c00138
Chem. Rev. XXXX, XXX, XXX−XXX

(57) Wang, Y.; Lomakin, A.; McManus, J. J.; Ogun, O.; Benedek, G. B. Phase Behavior of Mixtures of Human Lens Proteins gamma D and beta B1. *Proc. Natl. Acad. Sci. U.S.A.* **2010**, *107*, 13282−13287.
(58) Li, P.; Banjade, S.; Cheng, H. C.; Kim, S.; Chen, B.; Guo, L.; Llaguno, M.; Hollingsworth, J. V.; King, D. S.; Banani, S. F.; et al. Phase Transitions in the Assembly of Multivalent Signalling Proteins. *Nature* **2012**, *483*, 336−340.
(59) Weber, S. C.; Brangwynne, C. P. Getting RNA and Protein in Phase. *Cell* **2012**, *149*, 1188−1191.
(60) Berry, J.; Weber, S. C.; Vaidya, N.; Haataja, M.; Brangwynne, C. P. RNA Transcription Modulates Phase Transition-Driven Nuclear Body Assembly. *Proc. Natl. Acad. Sci. U.S.A.* **2015**, *112*, 5237−5425.
(61) Burke, K. A.; Janke, A. M.; Rhine, C. L.; Fawzi, N. L. Residue-by-Residue View of in vitro FUS Granules That Bind the C-Terminal Domain of RNA Polymerase II. *Mol. Cell* **2015**, *60*, 231−241.
(62) Lin, Y.; Protter, D. S. W.; Rosen, M. K.; Parker, R. Formation and Maturation of Phase-Separated Liquid Droplets by RNA-Binding Proteins. *Mol. Cell* **2015**, *60*, 208−219.
(63) Patel, A.; Lee, H. O.; Jawerth, L.; Maharana, S.; Jahnel, M.; Hein, M. Y.; Stoynov, S.; Mahamid, J.; Saha, S.; Franzmann, T. M.; et al. A Liquid-to-Solid Phase Transition of the ALS Protein FUS Accelerated by Disease Mutation. *Cell* **2015**, *162*, 1066−1077.
(64) Xiang, S.; Kato, M.; Wu, L. C.; Lin, Y.; Ding, M.; Zhang, Y.; Yu, Y.; McKnight, S. L. The LC Domain of hnRNPA2 Adopts Similar Conformations in Hydrogel Polymers, Liquid-like Droplets, and Nuclei. *Cell* **2015**, *163*, 829−839.
(65) Zhang, H.; Elbaum-Garfinkle, S.; Langdon, E. M.; Taylor, N.; Occhipinti, P.; Bridges, A. A.; Brangwynne, C. P.; Gladfelter, A. S. RNA Controls PolyQ Protein Phase Transitions. *Mol. Cell* **2015**, *60*, 220−230.
(66) Aumiller, W. M., Jr; Keating, C. D. Phosphorylation-Mediated RNA/Peptide Complex Coacervation as a Model for Intracellular Liquid Organelles. *Nat. Chem.* **2016**, *8*, 129−137.
(67) Conicella, A. E.; Zerze, G. H.; Mittal, J.; Fawzi, N. L. ALS Mutations Disrupt Phase Separation Mediated by Alpha-Helical Structure in the TDP-43 Low-Complexity C-Terminal Domain. *Structure* **2016**, *24*, 1537−1549.
(68) Saha, S.; Weber, C. A.; Nousch, M.; Adame-Arana, O.; Hoege, C.; Hein, M. Y.; Osborne-Nishimura, E.; Mahamid, J.; Jahnel, M.; Jawerth, L.; et al. Polar Positioning of Phase-Separated Liquid Compartments in Cells Regulated by an mRNA Competition Mechanism. *Cell* **2016**, *166*, 1572−1584.
(69) Smith, J.; Calidas, D.; Schmidt, H.; Lu, T.; Rasoloson, D.; Seydoux, G. Spatial Patterning of P Granules by RNA-Induced Phase Separation of the Intrinsically-Disordered Protein MEG-3. *eLife* **2016**, *5*, No. e21337.
(70) Banerjee, P. R.; Milin, A. N.; Moosa, M. M.; Onuchic, P. L.; Deniz, A. A. Reentrant Phase Transition Drives Dynamic Substructure Formation in Ribonucleoprotein Droplets. *Angew. Chem., Int. Ed. Engl.* **2017**, *56*, 11354−11359.
(71) Maharana, S.; Wang, J.; Papadopoulos, D. K.; Richter, D.; Pozniakovsky, A.; Poser, I.; Bickle, M.; Rizk, S.; Guillen-Boixet, J.; Franzmann, T. M.; et al. RNA Buffers the Phase Separation Behavior of Prion-Like RNA Binding Proteins. *Science* **2018**, *360*, 918−921.
(72) Wegmann, S.; Eftekharzadeh, B.; Tepper, K.; Zoltowska, K. M.; Bennett, R. E.; Dujardin, S.; Laskowski, P. R.; MacKenzie, D.; Kamath, T.; Commins, C.; et al. Tau Protein Liquid-Liquid Phase Separation Can Initiate Tau Aggregation. *EMBO J.* **2018**, *37*, No. e98049.
(73) Alshareedah, I.; Kaur, T.; Ngo, J.; Seppala, H.; Kounatse, L.-A. D.; Wang, W.; Moosa, M. M.; Banerjee, P. R. Interplay between Short-Range Attraction and Long-Range Repulsion Controls Reentrant Liquid Condensation of Ribonucleoprotein-RNA Complexes. *J. Am. Chem. Soc.* **2019**, *141*, 14593−14602.
(74) Boeynaems, S.; Holehouse, A. S.; Weinhardt, V.; Kovacs, D.; Van Lindt, J.; Larabell, C.; Van Den Bosch, L.; Das, R.; Tompa, P. S.; Pappu, R. V.; et al. Spontaneous Driving Forces Give Rise to Protein-RNA Condensates with Coexisting Phases and Complex Material Properties. *Proc. Natl. Acad. Sci. U.S.A.* **2019**, *116*, 7889−7898.
(75) Garcia-Jove Navarro, M.; Kashida, S.; Chouaib, R.; Souquere, S.; Pierron, G.; Weil, D.; Gueroui, Z. RNA Is a Critical Element for the Sizing and the Composition of Phase-Separated RNA-Protein Condensates. *Nat. Commun.* **2019**, *10*, 3230.
(76) Kang, J.; Lim, L.; Lu, Y.; Song, J. A Unified Mechanism for LLPS of ALS/FTLD-Causing FUS as well as Its Modulation by ATP and Oligonucleic Acids. *PLoS Biol.* **2019**, *17*, No. e3000327.
(77) Putnam, A.; Cassani, M.; Smith, J.; Seydoux, G. A Gel Phase Promotes Condensation of Liquid P Granules in *Caenorhabditis elegans* Embryos. *Nat. Struct. Mol. Biol.* **2019**, *26*, 220−226.
(78) Tsang, B.; Arsenault, J.; Vernon, R. M.; Lin, H.; Sonenberg, N.; Wang, L.-Y.; Bah, A.; Forman-Kay, J. D. Phosphoregulated FMRP Phase Separation Models Activity-Dependent Translation through Bidirectional Control of mRNA Granule Formation. *Proc. Natl. Acad. Sci. U.S.A.* **2019**, *116*, 4218−4227.
(79) Ukmar-Godec, T.; Hutten, S.; Grieshop, M. P.; Rezaei-Ghaleh, N.; Cima-Omori, M. S.; Biernat, J.; Mandelkow, E.; Soding, J.; Dormann, D.; Zweckstetter, M. Lysine/RNA-Interactions Drive and Regulate Biomolecular Condensation. *Nat. Commun.* **2019**, *10*, 2909.
(80) Alshareedah, I.; Moosa, M. M.; Raju, M.; Potoyan, D. A.; Banerjee, P. R. Phase Transition Of RNA-Protein Complexes into Ordered Hollow Condensates. *Proc. Natl. Acad. Sci. U.S.A.* **2020**, *117*, 15650−15658.
(81) Fisher, R. S.; Elbaum-Garfinkle, S. Tunable Multiphase Dynamics of Arginine and Lysine Liquid Condensates. *Nat. Commun.* **2020**, *11*, 4628.
(82) Guillen-Boixet, J.; Kopach, A.; Holehouse, A. S.; Wittmann, S.; Jahnel, M.; Schlussler, R.; Kim, K.; Trussina, I.; Wang, J.; Mateju, D.; et al. RNA-Induced Conformational Switching and Clustering of G3BP Drive Stress Granule Assembly by Condensation. *Cell* **2020**, *181*, 346−361.
(83) Perdikari, T. M.; Murthy, A. C.; Ryan, V. H.; Watters, S.; Naik, M. T.; Fawzi, N. L. SARS-CoV-2 Nucleocapsid Protein Phase-Separates with RNA and with Human hnRNPs. *EMBO J.* **2020**, *39*, No. e106478.
(84) Regy, R. M.; Dignon, G. L.; Zheng, W.; Kim, Y. C.; Mittal, J. Sequence Dependent Phase Separation of Protein-Polynucleotide Mixtures Elucidated Using Molecular Simulations. *Nucleic Acids Res.* **2020**, *48*, 12593−12603.
(85) Joseph, J. A.; Reinhardt, A.; Aguirre, A.; Chew, P. Y.; Russell, K. O.; Espinosa, J. R.; Garaizar, A.; Collepardo-Guevara, R. Physics-Driven Coarse-Grained Model for Biomolecular Phase Separation with Near-Quantitative Accuracy. *Nat. Comput. Sci.* **2021**, *1*, 732−743.
(86) Grese, Z. R.; Bastos, A. C.; Mamede, L. D.; French, R. L.; Miller, T. M.; Ayala, Y. M. Specific RNA interactions Promote TDP-43 Multivalent Phase Separation and Maintain Liquid Properties. *EMBO Rep.* **2021**, *22*, No. e53632.
(87) Le Vay, K.; Song, E. Y.; Ghosh, B.; Tang, T. D.; Mutschler, H. Enhanced Ribozyme-Catalyzed Recombination and Oligonucleotide Assembly in Peptide-RNA Condensates. *Angew. Chem., Int. Ed. Engl.* **2021**, *60*, 26096−26104.
(88) Loughlin, F. E.; West, D. L.; Gunzburg, M. J.; Waris, S.; Crawford, S. A.; Wilce, M. C. J.; Wilce, J. A. Tandem RNA Binding Sites Induce Self-Association of the Stress Granule Marker Protein TIA-1. *Nucleic Acids Res.* **2021**, *49*, 2403−2417.
(89) Ma, W.; Zhen, G.; Xie, W.; Mayr, C. In vivo Reconstitution Finds Multivalent RNA-RNA Interactions as Drivers of Mesh-Like Condensates. *eLife* **2021**, *10*, No. e64252.
(90) Neil, C. R.; Jeschonek, S. P.; Cabral, S. E.; O'Connell, L. C.; Powrie, E. A.; Otis, J. P.; Wood, T. R.; Mowry, K. L. L-Bodies Are RNA-Protein Condensates Driving RNA Localization in Xenopus Oocytes. *Mol. Biol. Cell* **2021**, *32*, ar37.
(91) Schmidt, H.; Putnam, A.; Rasoloson, D.; Seydoux, G. Protein-Based Condensation Mechanisms Drive the Assembly Of RNA-Rich P Granules. *eLife* **2021**, *10*, No. e63698.
(92) Zhou, Q.; Usluer, S.; Zhang, F.; Lenard, A. J.; Bourgeois, B. M. R.; Madl, T. ATP Regulates RNA-Driven Cold Inducible RNA Binding Protein Phase Separation. *Protein Sci.* **2021**, *30*, 1438−1453.
(93) Iglesias-Artola, J. M.; Drobot, B.; Kar, M.; Fritsch, A. W.; Mutschler, H.; Dora Tang, T. Y.; Kreysing, M. Charge-Density

https://doi.org/10.1021/acs.chemrev.4c00138
Chem. Rev. XXXX, XXX, XXX−XXX

Reduction Promotes Ribozyme Activity in RNA-Peptide Coacervates via RNA Fluidization and Magnesium Partitioning. *Nat. Chem.* **2022**, *14*, 407−416.
(94) Niu, J.; Qiu, C.; Abbott, N. L.; Gellman, S. H. Formation of versus Recruitment to RNA-Rich Condensates: Controlling Effects Exerted by Peptide Side Chain Identity. *J. Am. Chem. Soc.* **2022**, *144*, 10386−10395.
(95) Cardona, A. H.; Ecsedi, S.; Khier, M.; Yi, Z.; Bahri, A.; Ouertani, A.; Valero, F.; Labrosse, M.; Rouquet, S.; Robert, S.; et al. Self-Demixing of mRNA Copies Buffers mRNA:mRNA and mRNA:Regulator Stoichiometries. *Cell* **2023**, *186*, 4310−4324.
(96) Chen, S.; Rong, M.; Lv, Y.; Zhu, D.; Xiang, Y. Regulation of cGAS Activity by RNA-Modulated Phase Separation. *EMBO Rep.* **2023**, *24*, No. e51800.
(97) Zheng, H.; Peng, K.; Gou, X.; Ju, C.; Zhang, H. RNA recruitment Switches the Fate of Protein Condensates from Autophagic Degradation to Accumulation. *J. Cell Biol.* **2023**, *222*, No. e202210104.
(98) Rhine, K.; Vidaurre, V.; Myong, S. RNA Droplets. *Annu. Rev. Biophys.* **2020**, *49*, 247−265.
(99) Roden, C.; Gladfelter, A. S. RNA Contributions to the Form and Function of Biomolecular Condensates. *Nat. Rev. Mol. Cell Biol.* **2021**, *22*, 183−195.
(100) Forman-Kay, J. D.; Ditlev, J. A.; Nosella, M. L.; Lee, H. O. What Are the Distinguishing Features and Size Requirements of Biomolecular Condensates and Their Implications for RNA-Containing Condensates? *RNA* **2022**, *28*, 36−47.
(101) Roden, C. A.; Gladfelter, A. S. Design Considerations for Analyzing Protein Translation Regulation by Condensates. *RNA* **2022**, *28*, 88−96.
(102) Sharp, P. A.; Chakraborty, A. K.; Henninger, J. E.; Young, R. A. RNA in formation and Regulation of Transcriptional Condensates. *RNA* **2022**, *28*, 52−57.
(103) Jain, A.; Vale, R. D. RNA Phase Transitions in Repeat Expansion Disorders. *Nature* **2017**, *546*, 243−247.
(104) Van Treeck, B.; Protter, D. S. W.; Matheny, T.; Khong, A.; Link, C. D.; Parker, R. RNA Self-Assembly Contributes to Stress Granule Formation and Defining the Stress Granule Transcriptome. *Proc. Natl. Acad. Sci. U.S.A.* **2018**, *115*, 2734−2739.
(105) Onuchic, P. L.; Milin, A. N.; Alshareedah, I.; Deniz, A. A.; Banerjee, P. R. Divalent Cations Can Control a Switch-Like Behavior in Heterotypic and Homotypic RNA Coacervates. *Sci. Rep.* **2019**, *9*, 12161.
(106) Tauber, D.; Tauber, G.; Khong, A.; Van Treeck, B.; Pelletier, J.; Parker, R. Modulation of RNA Condensation by the DEAD-Box Protein eIF4A. *Cell* **2020**, *180*, 411−426.
(107) Poudyal, R. R.; Sieg, J. P.; Portz, B.; Keating, C. D.; Bevilacqua, P. C. RNA Sequence and Structure Control Assembly and Function of RNA Condensates. *RNA* **2021**, *27*, 1589−1601.
(108) Ma, Y.; Li, H.; Gong, Z.; Yang, S.; Wang, P.; Tang, C. Nucleobase Clustering Contributes to the Formation and Hollowing of Repeat-Expansion RNA Condensate. *J. Am. Chem. Soc.* **2022**, *144*, 4716−4720.
(109) Tom, J. K. A.; Onuchic, P. L.; Deniz, A. A. Short PolyA RNA Homopolymers Undergo Mg^{2+}-Mediated Kinetically Arrested Condensation. *J. Phys. Chem. B* **2022**, *126*, 9715−9725.
(110) Wadsworth, G. M.; Zahurancik, W. J.; Zeng, X.; Pullara, P.; Lai, L. B.; Sidharthan, V.; Pappu, R. V.; Gopalan, V.; Banerjee, P. R. RNAs Undergo Phase Transitions with Lower Critical Solution Temperatures. *Nat. Chem.* **2023**, *15*, 1693−1704.
(111) Du, M.; Chen, Z. J. DNA-Induced Liquid Phase Condensation of cGAS Activates Innate Immune Signaling. *Science* **2018**, *361*, 704−709.
(112) Turner, A. L.; Watson, M.; Wilkins, O. G.; Cato, L.; Travers, A.; Thomas, J. O.; Stott, K. Highly Disordered Histone H1-DNA Model Complexes and Their Condensates. *Proc. Natl. Acad. Sci. U.S.A.* **2018**, *115*, 11964−11969.
(113) Gibson, B. A.; Doolittle, L. K.; Schneider, M. W. G.; Jensen, L. E.; Gamarra, N.; Henry, L.; Gerlich, D. W.; Redding, S.; Rosen, M. K. Organization of Chromatin by Intrinsic and Regulated Phase Separation. *Cell* **2019**, *179*, 470−484.
(114) Zhou, H.; Song, Z.; Zhong, S.; Zuo, L.; Qi, Z.; Qu, L. J.; Lai, L. Mechanism of DNA-Induced Phase Separation for Transcriptional Repressor VRN1. *Angew. Chem., Int. Ed. Engl.* **2019**, *58*, 4858−4862.
(115) Harami, G. M.; Kovacs, Z. J.; Pancsa, R.; Palinkas, J.; Barath, V.; Tarnok, K.; Malnasi-Csizmadia, A.; Kovacs, M. Phase Separation by ssDNA Binding Protein Controlled via Protein-Protein and Protein-DNA Interactions. *Proc. Natl. Acad. Sci. U.S.A.* **2020**, *117*, 26206−26217.
(116) Shakya, A.; Park, S.; Rana, N.; King, J. T. Liquid-Liquid Phase Separation of Histone Proteins in Cells: Role in Chromatin Organization. *Biophys. J.* **2020**, *118*, 753−764.
(117) Lawrimore, J.; Kolbin, D.; Stanton, J.; Khan, M.; de Larminat, S. C.; Lawrimore, C.; Yeh, E.; Bloom, K. The rDNA Is Biomolecular Condensate Formed by Polymer-Polymer Phase Separation and Is Sequestered in the Nucleolus by Transcription and R-Loops. *Nucleic Acids Res.* **2021**, *49*, 4586−4598.
(118) Liu, X.; Xiong, Y.; Zhang, C.; Lai, R.; Liu, H.; Peng, R.; Fu, T.; Liu, Q.; Fang, X.; Mann, S.; et al. G-Quadruplex-Induced Liquid-Liquid Phase Separation in Biomimetic Protocells. *J. Am. Chem. Soc.* **2021**, *143*, 11036−11043.
(119) Muzzopappa, F.; Hertzog, M.; Erdel, F. DNA Length Tunes the Fluidity of DNA-Based Condensates. *Biophys. J.* **2021**, *120*, 1288−1300.
(120) Quail, T.; Golfier, S.; Elsner, M.; Ishihara, K.; Murugesan, V.; Renger, R.; Julicher, F.; Brugués, J. Force Generation by Protein-DNA Co-Condensation. *Nat. Phys.* **2021**, *17*, 1007.
(121) Ryu, J.-K.; Bouchoux, C.; Liu, H. W.; Kim, E.; Minamino, M.; de Groot, R.; Katan, A. J.; Bonato, A.; Marenduzzo, D.; Michieletto, D.; Uhlmann, F.; Dekker, C.; et al. Bridging-Induced Phase Separation Induced by Cohesin SMC Protein Complexes. *Sci. Adv.* **2021**, *7*, No. eabe5905.
(122) Sharma, R.; Choi, K.-J.; Quan, M. D.; Sharma, S.; Sankaran, B.; Park, H.; LaGrone, A.; Kim, J. J.; MacKenzie, K. R.; Ferreon, A. C. M.; Kim, C.; Ferreon, J. C.; et al. Liquid Condensation of Reprogramming Factor KLF4 with DNA Provides a Mechanism for Chromatin Organization. *Nat. Commun.* **2021**, *12*, 5579.
(123) Renger, R.; Morin, J. A.; Lemaitre, R.; Ruer-Gruss, M.; Julicher, F.; Hermann, A.; Grill, S. W. Co-Condensation of Proteins with Single- and Double-Stranded DNA. *Proc. Natl. Acad. Sci. U.S.A.* **2022**, *119*, No. e2107871119.
(124) Spegg, V.; Panagopoulos, A.; Stout, M.; Krishnan, A.; Reginato, G.; Imhof, R.; Roschitzki, B.; Cejka, P.; Altmeyer, M. Phase Separation Properties of RPA Combine High-Affinity ssDNA Binding with Dynamic Condensate Functions at Telomeres. *Nat. Struct. Mol. Biol.* **2023**, *30*, 451−462.
(125) Gupta, A.; Joshi, A.; Arora, K.; Mukhopadhyay, S.; Guptasarma, P. The Bacterial Nucleoid-Associated Proteins, HU and Dps, Condense DNA into Context-Dependent Biphasic or Multiphasic Complex Coacervates. *J. Biol. Chem.* **2023**, *299*, 104637.
(126) King, J. T.; Shakya, A. Phase Separation Of DNA: From Past To Present. *Biophys. J.* **2021**, *120*, 1139−1149.
(127) Jeon, B.-j.; Nguyen, D. T.; Abraham, G. R.; Conrad, N.; Fygenson, D. K.; Saleh, O. A. Salt-Dependent Properties of a Coacervate-Like, Self-Assembled DNA Liquid. *Soft Matter* **2018**, *14*, 7009−7015.
(128) Sato, Y.; Sakamoto, T.; Takinoue, M. Sequence-Based Engineering of Dynamic Functions of Micrometer-Sized DNA Droplets. *Sci. Adv.* **2020**, *6*, No. eaba3471.
(129) Jia, T. Z.; Hentrich, C.; Szostak, J. W. Rapid RNA Exchange in Aqueous Two-Phase System and Coacervate Droplets. *Orig. Life Evol. Biosph.* **2014**, *44*, 1−12.
(130) Kang, J.; Lim, L.; Song, J. ATP Enhances at Low Concentrations but Dissolves at High Concentrations Liquid-Liquid Phase Separation (LLPS) of ALS/FTD-Causing FUS. *Biochem. Biophys. Res. Commun.* **2018**, *504*, 545−551.

https://doi.org/10.1021/acs.chemrev.4c00138
Chem. Rev. XXXX, XXX, XXX−XXX

(131) Nakashima, K. K.; Baaij, J. F.; Spruijt, E. Reversible Generation of Coacervate Droplets in an Enzymatic Network. *Soft Matter* **2018**, *14*, 361−367.
(132) Babinchak, W. M.; Dumm, B. K.; Venus, S.; Boyko, S.; Putnam, A. A.; Jankowsky, E.; Surewicz, W. K. Small Molecules as Potent Biphasic Modulators of Protein Liquid-Liquid Phase Separation. *Nat. Commun.* **2020**, *11*, 5574.
(133) Dang, M.; Lim, L.; Kang, J.; Song, J. ATP Biphasically Modulates LLPS of TDP-43 PLD by Specifically Binding Arginine Residues. *Commun. Biol.* **2021**, *4*, 714.
(134) Toyama, Y.; Rangadurai, A. K.; Forman-Kay, J. D.; Kay, L. E. Mapping the Per-Residue Surface Electrostatic Potential of CAPRIN1 along Its Phase-Separation Trajectory. *Proc. Natl. Acad. Sci. U.S.A.* **2022**, *119*, No. e2210492119.
(135) Kota, D.; Prasad, R.; Zhou, H. X. Adenosine Triphosphate Mediates Phase Separation of Disordered Basic Proteins by Bridging Intermolecular Interaction Networks. *J. Am. Chem. Soc.* **2024**, *146*, 1326−1336.
(136) Choi, K. J.; Tsoi, P. S.; Moosa, M. M.; Paulucci-Holthauzen, A.; Liao, S. J.; Ferreon, J. C.; Ferreon, A. C. M. A Chemical Chaperone Decouples TDP-43 Disordered Domain Phase Separation from Fibrillation. *Biochemistry* **2018**, *57*, 6822−6826.
(137) Das, B.; Roychowdhury, S.; Mohanty, P.; Rizuan, A.; Chakraborty, J.; Mittal, J.; Chattopadhyay, K. A Zn-Dependent Structural Transition of SOD1Modulates Its Ability to Undergo Phase Separation. *EMBO J.* **2023**, *42*, No. e111185.
(138) Zhang, J. Z.; Lu, T. W.; Stolerman, L. M.; Tenner, B.; Yang, J. R.; Zhang, J. F.; Falcke, M.; Rangamani, P.; Taylor, S. S.; Mehta, S.; et al. Phase Separation of a PKA Regulatory Subunit Controls cAMP Compartmentation and Oncogenic Signaling. *Cell* **2020**, *182*, 1531−1544.
(139) Ahn, S. H.; Qin, S.; Zhang, J. Z.; McCammon, J. A.; Zhang, J.; Zhou, H. X. Characterizing Protein Kinase A (PKA) Subunits as Macromolecular Regulators of PKA RIalpha Liquid-Liquid Phase Separation. *J. Chem. Phys.* **2021**, *154*, 221101.
(140) Li, S.; Wang, Y.; Lai, L. Small Molecules in Regulating Protein Phase Separation. *Acta Biochim. Biophys. Sin. (Shanghai)* **2023**, *55*, 1075−1083.
(141) Kedersha, N. L.; Gupta, M.; Li, W.; Miller, I.; Anderson, P. RNA-Binding Proteins Tia-1 and Tiar Link the Phosphorylation of Eif-2α to the Assembly of Mammalian Stress Granules. *J. Cell Biol.* **1999**, *147*, 1431−1442.
(142) Hnisz, D.; Shrinivas, K.; Young, R. A.; Chakraborty, A. K.; Sharp, P. A. A Phase Separation Model for Transcriptional Control. *Cell* **2017**, *169*, 13−23.
(143) Riback, J. A.; Zhu, L.; Ferrolino, M. C.; Tolbert, M.; Mitrea, D. M.; Sanders, D. W.; Wei, M.-T.; Kriwacki, R. W.; Brangwynne, C. P. Composition-Dependent Thermodynamics of Intracellular Phase Separation. *Nature* **2020**, *581*, 209−214.
(144) Bracha, D.; Walls, M. T.; Wei, M. T.; Zhu, L.; Kurian, M.; Avalos, J. L.; Toettcher, J. E.; Brangwynne, C. P. Mapping Local and Global Liquid Phase Behavior in Living Cells Using Photo-Oligomerizable Seeds. *Cell* **2018**, *175*, 1467−1480.
(145) Ambadipudi, S.; Biernat, J.; Riedel, D.; Mandelkow, E.; Zweckstetter, M. Liquid-Liquid Phase Separation of the Microtubule-Binding Repeats of the Alzheimer-Related Protein Tau. *Nat. Commun.* **2017**, *8*, 275.
(146) Ghosh, A.; Zhang, X.; Zhou, H. X. Tug of War between Condensate Phases in a Minimal Macromolecular System. *J. Am. Chem. Soc.* **2020**, *142*, 8848−8861.
(147) Mazarakos, K.; Prasad, R.; Zhou, H. X. SpiDec: Computing binodals and interfacial tension of biomolecular condensates from simulations of spinodal decomposition. *Front. Mol. Biosci.* **2022**, *9*, 1021939.
(148) Urry, D. W. Entropic Elastic Processes in Protein Mechanisms. I. Elastic Structure due to an Inverse Temperature Transition and Elasticity due to Internal Chain Dynamics. *J. Protein Chem.* **1988**, *7*, 1−34.
(149) Lin, Y.; McCarty, J.; Rauch, J. N.; Delaney, K. T.; Kosik, K. S.; Fredrickson, G. H.; Shea, J.-E.; Han, S. Narrow Equilibrium Window for Complex Coacervation of Tau and RNA under Cellular Conditions. *eLife* **2019**, *8*, No. e42571.
(150) Ng, S. C.; Görlich, D. A Simple Thermodynamic Description of Phase Separation Of Nup98 FG Domains. *Nat. Commun.* **2022**, *13*, 6172.
(151) McMillan, W. G., Jr; Mayer, J. E. The Statistical Thermodynamics of Multicomponent Systems. *J. Chem. Phys.* **1945**, *13*, 276−305.
(152) Klosin, A.; Oltsch, F.; Harmon, T.; Honigmann, A.; Jülicher, F.; Hyman, A. A.; Zechner, C. Phase Separation Provides a Mechanism to Reduce Noise in Cells. *Science* **2020**, *367*, 464−468.
(153) Riback, J. A.; Brangwynne, C. P. Can Phase Separation Buffer Cellular Noise? *Science* **2020**, *367*, 364−365.
(154) Deviri, D.; Safran, S. A. Physical Theory of Biological Noise Buffering by Multicomponent Phase Separation. *Proc. Natl. Acad. Sci. U.S.A.* **2021**, *118*, No. e2100099118.
(155) Van der Waals, J. D. On the Continuity of the Gaseous and Liquid States. *PhD Thesis*, University of Leiden: Leiden, 1873.
(156) Clerk-Maxwell, J. On the Dynamical Evidence of the Molecular Constitution of Bodies. *Nature* **1875**, *11*, 357−359.
(157) Qin, S.; Zhou, H. X. Fast Method for Computing Chemical Potentials and Liquid-Liquid Phase Equilibria of Macromolecular Solutions. *J. Phys. Chem. B* **2016**, *120*, 8164−8174.
(158) Gibbs, J. W. *The Scientific Papers of J. Willard Gibbs*; Dover Publications: New York, 1961.
(159) Oxtoby, D. W. Nucleation of First-Order Phase Transitions. *Acc. Chem. Res.* **1998**, *31*, 91−97.
(160) Boire, A.; Sanchez, C.; Morel, M. H.; Lettinga, M. P.; Menut, P. Dynamics of Liquid-Liquid Phase Separation of Wheat Gliadins. *Sci. Rep.* **2018**, *8*, 14441.
(161) Narayanan, A.; Meriin, A.; Andrews, J. O.; Spille, J.-H.; Sherman, M. Y.; Cisse, I. I. A First Order Phase Transition Mechanism Underlies Protein Aggregation in Mammalian Cells. *eLife* **2019**, *8*, No. e39695.
(162) Kasinsky, H. E.; Gowen, B. E.; Ausio, J. Spermiogenic Chromatin Condensation Patterning in Several Hexapods May Involve Phase Separation Dynamics by Spinodal Decomposition or Microemulsion Inversion (Nucleation). *Tissue Cell* **2021**, *73*, 101648.
(163) Martin, E. W.; Harmon, T. S.; Hopkins, J. B.; Chakravarthy, S.; Incicco, J. J.; Schuck, P.; Soranno, A.; Mittag, T. A Multi-Step Nucleation Process Determines the Kinetics of Prion-Like Domain Phase Separation. *Nat. Commun.* **2021**, *12*, 4513.
(164) Shimobayashi, S. F.; Ronceray, P.; Sanders, D. W.; Haataja, M. P.; Brangwynne, C. P. Nucleation Landscape of Biomolecular Condensates. *Nature* **2021**, *599*, 503−506.
(165) Kar, M.; Dar, F.; Welsh, T. J.; Vogel, L. T.; Kuhnemuth, R.; Majumdar, A.; Krainer, G.; Franzmann, T. M.; Alberti, S.; Seidel, C. A. M.; et al. Phase-Separating RNA-Binding Proteins Form Heterogeneous Distributions of Clusters in Subsaturated Solutions. *Proc. Natl. Acad. Sci. U.S.A.* **2022**, *119*, No. e2202222119.
(166) Lan, C.; Kim, J.; Ulferts, S.; Aprile-Garcia, F.; Weyrauch, S.; Anandamurugan, A.; Grosse, R.; Sawarkar, R.; Reinhardt, A.; Hugel, T. Quantitative Real-Time In-Cell Imaging Reveals Heterogeneous Clusters of Proteins prior to Condensation. *Nat. Commun.* **2023**, *14*, 4831.
(167) Ray, S.; Mason, T. O.; Boyens-Thiele, L.; Farzadfard, A.; Larsen, J. A.; Norrild, R. K.; Jahnke, N.; Buell, A. K. Mass Photometric Detection and Quantification Of Nanoscale alpha-Synuclein Phase Separation. *Nat. Chem.* **2023**, *15*, 1306−1316.
(168) Valverde, J. M.; Dubra, G.; Phillips, M.; Haider, A.; Elena-Real, C.; Fournet, A.; Alghoul, E.; Chahar, D.; Andres-Sanchez, N.; Paloni, M.; et al. A Cyclin-Dependent Kinase-Mediated Phosphorylation Switch of Disordered Protein Condensation. *Nat. Commun.* **2023**, *14*, 6316.
(169) Zeng, X.; Holehouse, A. S.; Chilkoti, A.; Mittag, T.; Pappu, R. V. Connecting Coil-to-Globule Transitions to Full Phase Diagrams for Intrinsically Disordered Proteins. *Biophys. J.* **2020**, *119*, 402−418.

https://doi.org/10.1021/acs.chemrev.4c00138
Chem. Rev. XXXX, XXX, XXX−XXX

(170) Mayer, J. E.; Mayer, M. G. *Statistical Mechanics*; John Wiley And Sons Inc.: New York, 1940.
(171) Hill, T. L. *An Introduction to Statistical Thermodynamics*; Dover Publications, Inc.: New York, 1986.
(172) Dignon, G. L.; Zheng, W.; Best, R. B.; Kim, Y. C.; Mittal, J. Relation between Single-Molecule Properties and Phase Behavior of Intrinsically Disordered Proteins. *Proc. Natl. Acad. Sci. U.S.A.* **2018**, *115*, 9929−9934.
(173) Qian, D.; Michaels, T. C. T.; Knowles, T. P. J. Analytical Solution to the Flory-Huggins Model. *J. Phys. Chem. Lett.* **2022**, *13*, 7853−7860.
(174) Brady, J. P.; Farber, P. J.; Sekhar, A.; Lin, Y.-H.; Huang, R.; Bah, A.; Nott, T. J.; Chan, H. S.; Baldwin, A. J.; Forman-Kay, J. D.; et al. Structural and Hydrodynamic Properties of an Intrinsically Disordered Region of a Germ Cell-Specific Protein on Phase Separation. *Proc. Natl. Acad. Sci. U.S.A.* **2017**, *114*, No. E8194-E8203.
(175) Wei, M. T.; Elbaum-Garfinkle, S.; Holehouse, A. S.; Chen, C. C.; Feric, M.; Arnold, C. B.; Priestley, R. D.; Pappu, R. V.; Brangwynne, C. P. Phase Behaviour of Disordered Proteins Underlying Low Density and High Permeability of Liquid Organelles. *Nat. Chem.* **2017**, *9*, 1118−1125.
(176) Martin, E. W.; Holehouse, A. S.; Peran, I.; Farag, M.; Incicco, J. J.; Bremer, A.; Grace, C. R.; Soranno, A.; Pappu, R. V.; Mittag, T. Valence and Patterning of Aromatic Residues Determine the Phase Behavior of Prion-Like Domains. *Science* **2020**, *367*, 694−699.
(177) Galvanetto, N.; Ivanović, M. T.; Chowdhury, A.; Sottini, A.; Nüesch, M. F.; Nettels, D.; Best, R. B.; Schuler, B. Extreme Dynamics in a Biomolecular Condensate. *Nature* **2023**, *619*, 876−883.
(178) Zwicker, D.; Laan, L. Evolved Interactions Stabilize Many Coexisting Phases in Multicomponent Liquids. *Proc. Natl. Acad. Sci. U.S.A.* **2022**, *119*, No. e2201250119.
(179) de Gennes, P. G. Theory of X-Ray Scattering by Liquid Macromolecules with Heavy Atom Labels. *J. Phys. (Paris)* **1970**, *31*, 235−238.
(180) Leibler, L. Theory of Microphase Separation in Block Copolymers. *Macromolecules* **1980**, *13*, 1602−1617.
(181) Bohm, D.; Pines, D. A Collective Description of Electron Interactions. I. Magnetic Interactions. *Phys. Rev.* **1951**, *82*, 625−634.
(182) Gell-Mann, M.; Brueckner, K. A. Correlation Energy of an Electron Gas at High Density. *Phys. Rev.* **1957**, *106*, 364−368.
(183) Lin, Y.-H.; Forman-Kay, J. D.; Chan, H. S. Sequence-Specific Polyampholyte Phase Separation in Membraneless Organelles. *Phys. Rev. Lett.* **2016**, *117*, 178101.
(184) Lin, Y.-H.; Chan, H. S. Phase Separation and Single-Chain Compactness of Charged Disordered Proteins Are Strongly Correlated. *Biophys. J.* **2017**, *112*, 2043−2046.
(185) Das, S.; Eisen, A.; Lin, Y.-H.; Chan, H. S. A Lattice Model of Charge-Pattern-Dependent Polyampholyte Phase Separation. *J. Phys. Chem. B* **2018**, *122*, 5418−5431.
(186) McCarty, J.; Delaney, K. T.; Danielsen, S. P. O.; Fredrickson, G. H.; Shea, J. E. Complete Phase Diagram for Liquid-Liquid Phase Separation of Intrinsically Disordered Proteins. *J. Phys. Chem. Lett.* **2019**, *10*, 1644−1652.
(187) Chang, L.-W.; Lytle, T. K.; Radhakrishna, M.; Madinya, J. J.; Vélez, J.; Sing, C. E.; Perry, S. L. Sequence and Entropy-Based Control of Complex Coacervates. *Nat. Commun.* **2017**, *8*, 1273.
(188) Roggeveen, J. V.; Wang, H.; Shi, Z.; Stone, H. A. A Calibration-Free Model of Micropipette Aspiration for Measuring Properties of Protein Condensates. *Biophys. J.* **2023**, DOI: 10.1016/j.bpj.2023.09.018.
(189) Mazarakos, K.; Qin, S.; Zhou, H. X. Calculating Binodals and Interfacial Tension of Phase-Separated Condensates from Molecular Simulations with Finite-Size Corrections. *Methods Mol. Biol.* **2023**, *2563*, 1−35.
(190) Widom, B. Some Topics in the Theory of Fluids. *J. Chem. Phys.* **1963**, *39*, 2808−2812.
(191) Fredrickson, G. H. *The Equilibrium Theory of Inhomogeneous Polymers*; Oxford University Press: Oxford, U.K., 2006.
(192) Guggenheim, E. A. The Principle of Corresponding States. *J. Chem. Phys.* **1945**, *13*, 253−261.
(193) Qin, S.; Zhou, H. X. Calculation of Second Virial Coefficients of Atomistic Proteins Using Fast Fourier Transform. *J. Phys. Chem. B* **2019**, *123*, 8203−8215.
(194) Qin, S.; Zhou, H. X. Atomistic Modeling of Liquid-Liquid Phase Equilibrium Explains Dependence of Critical Temperature on gamma-Crystallin Sequence. *Commun. Biol.* **2023**, *6*, 886.
(195) Panagiotopoulos, A. Z. Direct Determination of Phase Coexistence Properties of Fluids by Monte Carlo Simulations in a New Ensemble. *Mol. Phys.* **1987**, *61*, 813−826.
(196) Riggleman, R. A.; Fredrickson, G. H. Field-Theoretic Simulations in the Gibbs Ensemble. *J. Chem. Phys.* **2010**, *132*, 024104.
(197) Lytle, T. K.; Radhakrishna, M.; Sing, C. E. High Charge Density Coacervate Assembly via Hybrid Monte Carlo Single Chain in Mean Field Theory. *Macromolecules* **2016**, *49*, 9693−9705.
(198) Li, L.; Srivastava, S.; Andreev, M.; Marciel, A. B.; de Pablo, J. J.; Tirrell, M. V. Phase Behavior and Salt Partitioning in Polyelectrolyte Complex Coacervates. *Macromolecules* **2018**, *51*, 2988−2995.
(199) Rao, M.; Levesque, D. Surface-Structure of a Liquid-Film. *J. Chem. Phys.* **1976**, *65*, 3233−3236.
(200) Binder, K.; Block, B. J.; Virnau, P.; Tröster, A. Beyond the Van Der Waals Loop: What Can Be Learned from Simulating Lennard-Jones Fluids Inside the Region of Phase Coexistence. *Am. J. Phys.* **2012**, *80*, 1099−1109.
(201) Das, S.; Amin, A. N.; Lin, Y. H.; Chan, H. S. Coarse-Grained Residue-Based Models of Disordered Protein Condensates: Utility and Limitations of Simple Charge Pattern Parameters. *Phys. Chem. Chem. Phys.* **2018**, *20*, 28558−28574.
(202) Dignon, G. L.; Zheng, W.; Kim, Y. C.; Best, R. B.; Mittal, J. Sequence Determinants of Protein Phase Behavior from a Coarse-Grained Model. *PLoS Comput. Biol.* **2018**, *14*, No. e1005941.
(203) Dignon, G. L.; Zheng, W.; Kim, Y. C.; Mittal, J. Temperature-Controlled Liquid-Liquid Phase Separation of Disordered Proteins. *ACS Cent. Sci.* **2019**, *5*, 821−830.
(204) Chou, H. Y.; Aksimentiev, A. Single-Protein Collapse Determines Phase Equilibria of a Biological Condensate. *J. Phys. Chem. Lett.* **2020**, *11*, 4923−4929.
(205) Conicella, A. E.; Dignon, G. L.; Zerze, G. H.; Schmidt, H. B.; D'Ordine, A. M.; Kim, Y. C.; Rohatgi, R.; Ayala, Y. M.; Mittal, J.; Fawzi, N. L. TDP-43 Alpha-Helical Structure Tunes Liquid-Liquid Phase Separation and Function. *Proc. Natl. Acad. Sci. U.S.A.* **2020**, *117*, 5883−5894.
(206) Das, S.; Lin, Y. H.; Vernon, R. M.; Forman-Kay, J. D.; Chan, H. S. Comparative Roles of Charge, Pi, and Hydrophobic Interactions in Sequence-Dependent Phase Separation of Intrinsically Disordered Proteins. *Proc. Natl. Acad. Sci. U.S.A.* **2020**, *117*, 28795−28805.
(207) Espinosa, J. R.; Joseph, J. A.; Sanchez-Burgos, I.; Garaizar, A.; Frenkel, D.; Collepardo-Guevara, R. Liquid Network Connectivity Regulates the Stability and Composition of Biomolecular Condensates with Many Components. *Proc. Natl. Acad. Sci. U.S.A.* **2020**, *117*, 13238−13247.
(208) Bari, K. J.; Prakashchand, D. D. Fundamental Challenges and Outlook in Simulating Liquid-Liquid Phase Separation of Intrinsically Disordered Proteins. *J. Phys. Chem. Lett.* **2021**, *12*, 1644−1656.
(209) Farr, S. E.; Woods, E. J.; Joseph, J. A.; Garaizar, A.; Collepardo-Guevara, R. Nucleosome Plasticity Is a Critical Element of Chromatin Liquid-Liquid Phase Separation and Multivalent Nucleosome Interactions. *Nat. Commun.* **2021**, *12*, 2883.
(210) Garaizar, A.; Espinosa, J. R. Salt Dependent Phase Behavior of Intrinsically Disordered Proteins from a Coarse-Grained Model with Explicit Water and Ions. *J. Chem. Phys.* **2021**, *155*, 125103.
(211) Joseph, J. A.; Espinosa, J. R.; Sanchez-Burgos, I.; Garaizar, A.; Frenkel, D.; Collepardo-Guevara, R. Thermodynamics and Kinetics of Phase Separation of Protein-RNA Mixtures by a Minimal Model. *Biophys. J.* **2021**, *120*, 1219−1230.
(212) Lichtinger, S. M.; Garaizar, A.; Collepardo-Guevara, R.; Reinhardt, A. Targeted Modulation of Protein Liquid-Liquid Phase

https://doi.org/10.1021/acs.chemrev.4c00138
Chem. Rev. XXXX, XXX, XXX−XXX

Separation by Evolution of Amino-Acid Sequence. *PLoS Comput. Biol.* **2021**, *17*, No. e1009328.
(213) Mazarakos, K.; Zhou, H. X. Macromolecular Regulators Have Matching Effects on the Phase Equilibrium and Interfacial Tension of Biomolecular Condensates. *Protein Sci.* **2021**, *30*, 1360−1370.
(214) Nilsson, D.; Irback, A. Finite-Size Shifts in Simulated Protein Droplet Phase Diagrams. *J. Chem. Phys.* **2021**, *154*, 235101.
(215) Perdikari, T. M.; Jovic, N.; Dignon, G. L.; Kim, Y. C.; Fawzi, N. L.; Mittal, J. A Predictive Coarse-Grained Model for Position-Specific Effects of Post-Translational Modifications. *Biophys. J.* **2021**, *120*, 1187−1197.
(216) Regy, R. M.; Thompson, J.; Kim, Y. C.; Mittal, J. Improved Coarse-Grained Model for Studying Sequence Dependent Phase Separation of Disordered Proteins. *Protein Sci.* **2021**, *30*, 1371−1379.
(217) Tejedor, A. R.; Garaizar, A.; Ramirez, J.; Espinosa, J. R. Rna Modulation of Transport Properties and Stability in Phase-Separated Condensates. *Biophys. J.* **2021**, *120*, 5169−5186.
(218) Tesei, G.; Schulze, T. K.; Crehuet, R.; Lindorff-Larsen, K. Accurate Model of Liquid-Liquid Phase Behavior of Intrinsically Disordered Proteins from Optimization of Single-Chain Properties. *Proc. Natl. Acad. Sci. U.S.A.* **2021**, *118*, No. e2111696118.
(219) Wessen, J.; Pal, T.; Das, S.; Lin, Y. H.; Chan, H. S. A Simple Explicit-Solvent Model of Polyampholyte Phase Behaviors and Its Ramifications for Dielectric Effects in Biomolecular Condensates. *J. Phys. Chem. B* **2021**, *125*, 4337−4358.
(220) Bauer, D. J.; Stelzl, L. S.; Nikoubashman, A. Single-Chain and Condensed-State Behavior of hnRNPA1 from Molecular Simulations. *J. Chem. Phys.* **2022**, *157*, 154903.
(221) Her, C.; Phan, T. M.; Jovic, N.; Kapoor, U.; Ackermann, B. E.; Rizuan, A.; Kim, Y. C.; Mittal, J.; Debelouchina, G. T. Molecular Interactions Underlying the Phase Separation of HP1alpha: Role of Phosphorylation, Ligand and Nucleic Acid Binding. *Nucleic Acids Res.* **2022**, *50*, 12702−12722.
(222) Laghmach, R.; Alshareedah, I.; Pham, M.; Raju, M.; Banerjee, P. R.; Potoyan, D. A. RNA Chain Length and Stoichiometry Govern Surface Tension and Stability of Protein-RNA Condensates. *iScience* **2022**, *25*, 104105.
(223) Murata, Y.; Niina, T.; Takada, S. The Stoichiometric Interaction Model for Mesoscopic MD Simulations of Liquid-Liquid Phase Separation. *Biophys. J.* **2022**, *121*, 4382−4393.
(224) Sanchez-Burgos, I.; Espinosa, J. R.; Joseph, J. A.; Collepardo-Guevara, R. RNA Length Has a Non-Trivial Effect in the Stability of Biomolecular Condensates Formed by RNA-Binding Proteins. *PLoS Comput. Biol.* **2022**, *18*, No. e1009810.
(225) Tejedor, A. R.; Sanchez-Burgos, I.; Estevez-Espinosa, M.; Garaizar, A.; Collepardo-Guevara, R.; Ramirez, J.; Espinosa, J. R. Protein Structural Transitions Critically Transform the Network Connectivity and Viscoelasticity of RNA-Binding Protein Condensates but RNA Can Prevent It. *Nat. Commun.* **2022**, *13*, 5717.
(226) Blazquez, S.; Sanchez-Burgos, I.; Ramirez, J.; Higginbotham, T.; Conde, M. M.; Collepardo-Guevara, R.; Tejedor, A. R.; Espinosa, J. R. Location and Concentration of Aromatic-Rich Segments Dictates the Percolating Inter-Molecular Network and Viscoelastic Properties of Ageing Condensates. *Adv. Sci.* **2023**, *10*, No. e2207742.
(227) Chew, P. Y.; Joseph, J. A.; Collepardo-Guevara, R.; Reinhardt, A. Aromatic and Arginine Content Drives Multiphasic Condensation of Protein-RNA Mixtures. *Biophys. J.* **2023**, DOI: 10.1016/j.bpj.2023.06.024.
(228) Chew, P. Y.; Joseph, J. A.; Collepardo-Guevara, R.; Reinhardt, A. Thermodynamic Origins of Two-Component Multiphase Condensates of Proteins. *Chem. Sci.* **2023**, *14*, 1820−1836.
(229) Ingolfsson, H. I.; Rizuan, A.; Liu, X.; Mohanty, P.; Souza, P. C. T.; Marrink, S. J.; Bowers, M. T.; Mittal, J.; Berry, J. Multiscale Simulations Reveal TDP-43 Molecular-Level Interactions Driving Condensation. *Biophys. J.* **2023**, *122*, 4370−4381.
(230) Kapoor, U.; Kim, Y. C.; Mittal, J. Coarse-Grained Models to Study Protein-DNA Interactions and Liquid-Liquid Phase Separation. *J. Chem. Theory Comput.* **2024**, *20*, 1717−1731.
(231) Li, L.; Hou, Z. Crosslink-Induced Conformation Change of Intrinsically Disordered Proteins Have a Nontrivial Effect on Phase Separation Dynamics and Thermodynamics. *J. Phys. Chem. B* **2023**, *127*, 5018−5026.
(232) Li, L.; Paloni, M.; Finney, A. R.; Barducci, A.; Salvalaglio, M. Nucleation of Biomolecular Condensates from Finite-Sized Simulations. *J. Phys. Chem. Lett.* **2023**, *14*, 1748−1755.
(233) Liu, S.; Wang, C.; Latham, A. P.; Ding, X.; Zhang, B. OpenABC Enables Flexible, Simplified, and Efficient GPU Accelerated Simulations of Biomolecular Condensates. *PLoS Comput. Biol.* **2023**, *19*, No. e1011442.
(234) Maristany, M. J.; Gonzalez, A. A.; Collepardo-Guevara, R.; Joseph, J. A. Universal Predictive Scaling Laws of Phase Separation of Prion-Like Low Complexity Domains. *bioRxiv* **2023**, DOI: 10.1101/2023.06.14.543914, (acccessed 2024−02−15).
(235) Mohanty, P.; Shenoy, J.; Rizuan, A.; Mercado-Ortiz, J. F.; Fawzi, N. L.; Mittal, J. A Synergy between Site-Specific and Transient Interactions Drives the Phase Separation of a Disordered, Low-Complexity Domain. *Proc. Natl. Acad. Sci. U.S.A.* **2023**, *120*, No. e2305625120.
(236) Phan, T. M.; Kim, Y. C.; Debelouchina, G. T.; Mittal, J. Interplay between Charge Distribution and DNA in Shaping HP1 Paralog Phase Separation and Localization. *eLife* **2024**, *12*, RP90820.
(237) Ramirez, D. A.; Hough, L. E.; Shirts, M. R. Coiled-Coil Domains Are Sufficient to Drive Liquid-Liquid Phase Separation in Protein Models. *Biophys. J.* **2024**, *123*, 703−717.
(238) Ramsak, M.; Ramirez, D. A.; Hough, L. E.; Shirts, M. R.; Vidmar, S.; Elersic Filipic, K.; Anderluh, G.; Jerala, R. Programmable De Novo Designed Coiled Coil-Mediated Phase Separation in Mammalian Cells. *Nat. Commun.* **2023**, *14*, 7973.
(239) Rana, U.; Xu, K.; Narayanan, A.; Walls, M. T.; Panagiotopoulos, A. Z.; Avalos, J. L.; Brangwynne, C. P. Asymmetric Oligomerization State and Sequence Patterning Can Tune Multiphase Condensate Miscibility. *Nat. Chem.* **2024**, DOI: 10.1038/s41557-024-01456-6.
(240) Rekhi, S.; Sundaravadivelu Devarajan, D.; Howard, M. P.; Kim, Y. C.; Nikoubashman, A.; Mittal, J. Role of Strong Localized vs Weak Distributed Interactions in Disordered Protein Phase Separation. *J. Phys. Chem. B* **2023**, *127*, 3829−3838.
(241) Sanchez-Burgos, I.; Herriott, L.; Collepardo-Guevara, R.; Espinosa, J. R. Surfactants or Scaffolds? RNAs of Varying Lengths Control the Thermodynamic Stability of Condensates Differently. *Biophys. J.* **2023**, *122*, 2973−2987.
(242) Tesei, G.; Lindorff-Larsen, K. Improved Predictions of Phase Behaviour of Intrinsically Disordered Proteins by Tuning the Interaction Range. *Open Res. Eur.* **2022**, *2*, 94.
(243) Zhu, H.; Narita, M.; Joseph, J. A.; Krainer, G.; Arter, W. E.; Olan, I.; Saar, K. L.; Ermann, N.; Espinosa, J. R.; Shen, Y.; et al. The Chromatin Regulator HMGA1a Undergoes Phase Separation in the Nucleus. *Chembiochem* **2023**, *24*, No. e202200450.
(244) Adachi, K.; Kawaguchi, K. Predicting Heteropolymer Interactions: Demixing and Hypermixing of Disordered Protein Sequences. *arXiv* **2024**, DOI: 10.48550/arXiv.2401.07826, (acccessed 2024−02−15).
(245) An, Y.; Webb, M. A.; Jacobs, W. M. Active Learning of the Thermodynamics-Dynamics Trade-off in Protein Condensates. *Sci. Adv.* **2024**, *10*, No. eadj2448.
(246) Sundaravadivelu Devarajan, D.; Wang, J.; Szala-Mendyk, B.; Rekhi, S.; Nikoubashman, A.; Kim, Y. C.; Mittal, J. Sequence-Dependent Material Properties of Biomolecular Condensates and Their Relation to Dilute Phase Conformations. *Nat. Commun.* **2024**, *15*, 1912.
(247) Mohanty, P.; Rizuan, A.; Kim, Y. C.; Fawzi, N. L.; Mittal, J. A Complex Network of Interdomain Interactions Underlies the Conformational Ensemble of Monomeric TDP-43 and Modulates Its Phase Behavior. *Protein Sci.* **2024**, *33*, No. e4891.
(248) Welles, R. M.; Sojitra, K. A.; Garabedian, M. V.; Xia, B.; Wang, W.; Guan, M.; Regy, R. M.; Gallagher, E. R.; Hammer, D. A.; Mittal, J.; et al. Determinants That Enable Disordered Protein Assembly into

https://doi.org/10.1021/acs.chemrev.4c00138
Chem. Rev. XXXX, XXX, XXX−XXX

Discrete Condensed Phases. *Nat. Chem.* **2024**, DOI: 10.1038/s41557-023-01423-7.
(249) Zhang, Y.; Li, S.; Gong, X.; Chen, J. Toward Accurate Simulation of Coupling between Protein Secondary Structure and Phase Separation. *J. Am. Chem. Soc.* **2024**, *146*, 342−357.
(250) Zheng, W.; Dignon, G. L.; Jovic, N.; Xu, X.; Regy, R. M.; Fawzi, N. L.; Kim, Y. C.; Best, R. B.; Mittal, J. Molecular Details of Protein Condensates Probed by Microsecond Long Atomistic Simulations. *J. Phys. Chem. B* **2020**, *124*, 11671−11679.
(251) Welsh, T. J.; Krainer, G.; Espinosa, J. R.; Joseph, J. A.; Sridhar, A.; Jahnel, M.; Arter, W. E.; Saar, K. L.; Alberti, S.; Collepardo-Guevara, R.; et al. Surface Electrostatics Govern the Emulsion Stability of Biomolecular Condensates. *Nano Lett.* **2022**, *22*, 612−621.
(252) Saar, K. L.; Qian, D.; Good, L. L.; Morgunov, A. S.; Collepardo-Guevara, R.; Best, R. B.; Knowles, T. P. J. Theoretical and Data-Driven Approaches for Biomolecular Condensates. *Chem. Rev.* **2023**, *123*, 8988−9009.
(253) Abbas, M.; Lipiński, W. P.; Nakashima, K. K.; Huck, W. T. S.; Spruijt, E. A Short Peptide Synthon for Liquid-Liquid Phase Separation. *Nat. Chem.* **2021**, *13*, 1046−1054.
(254) De Sancho, D. Phase Separation in Amino Acid Mixtures Is Governed by Composition. *Biophys. J.* **2022**, *121*, 4119−4127.
(255) Polyansky, A. A.; Gallego, L. D.; Efremov, R. G.; Köhler, A.; Zagrovic, B. Protein Compactness and Interaction Valency Define the Architecture of a Biomolecular Condensate across Scales. *eLife* **2023**, *12*, No. e80038.
(256) Wang, J.; Wolf, R. M.; Caldwell, J. W.; Kollman, P. A.; Case, D. A. Development and Testing of a General Amber Force Field. *J. Comput. Chem.* **2004**, *25*, 1157−1174.
(257) Jorgensen, W. L.; Chandrasekhar, J.; Madura, J. D.; Impey, R. W.; Klein, M. L. Comparison of Simple Potential Functions for Simulating Liquid Water. *J. Chem. Phys.* **1983**, *79*, 926−935.
(258) Reed, E. H.; Hammer, D. A. Redox Sensitive Protein Droplets from Recombinant Oleosin. *Soft Matter* **2018**, *14*, 6506−6513.
(259) Martin, E. W; Thomasen, F E.; Milkovic, N. M; Cuneo, M. J; Grace, C. R; Nourse, A.; Lindorff-Larsen, K.; Mittag, T. Interplay of Folded Domains and the Disordered Low-Complexity Domain in Mediating hnRNPA1 Phase Separation. *Nucleic Acids Res.* **2021**, *49*, 2931−2945.
(260) Babinchak, W. M.; Haider, R.; Dumm, B. K.; Sarkar, P.; Surewicz, K.; Choi, J. K.; Surewicz, W. K. The Role of Liquid-Liquid Phase Separation in Aggregation of the TDP-43 Low-Complexity Domain. *J. Biol. Chem.* **2019**, *294*, 6306−6317.
(261) Agarwal, A.; Rai, S. K.; Avni, A.; Mukhopadhyay, S. An Intrinsically Disordered Pathological Prion Variant Y145stop Converts into Self-Seeding Amyloids via Liquid-Liquid Phase Separation. *Proc. Natl. Acad. Sci. U.S.A.* **2021**, *118*, No. e2100968118.
(262) Otis, J. B.; Sharpe, S. Sequence Context and Complex Hofmeister Salt Interactions Dictate Phase Separation Propensity of Resilin-like Polypeptides. *Biomacromolecules* **2022**, *23*, 5225−5238.
(263) Le Ferrand, H.; Duchamp, M.; Gabryelczyk, B.; Cai, H.; Miserez, A. Time-Resolved Observations of Liquid-Liquid Phase Separation at the Nanoscale Using in Situ Liquid Transmission Electron Microscopy. *J. Am. Chem. Soc.* **2019**, *141*, 7202−7210.
(264) Muschol, M.; Rosenberger, F. Liquid-Liquid Phase Separation in Supersaturated Lysozyme Solutions and Associated Precipitate Formation/Crystallization. *J. Chem. Phys.* **1997**, *107*, 1953−1962.
(265) Zhou, H. X.; Pang, X. Electrostatic Interactions in Protein Structure, Folding, Binding, and Condensation. *Chem. Rev.* **2018**, *118*, 1691−1741.
(266) Krainer, G.; Welsh, T. J.; Joseph, J. A.; Espinosa, J. R.; Wittmann, S.; de Csilléry, E.; Sridhar, A.; Toprakcioglu, Z.; Gudiškyte, G.; Czekalska, M. A.; et al. Reentrant Liquid Condensate Phase of Proteins Is Stabilized by Hydrophobic and Non-Ionic Interactions. *Nat. Commun.* **2021**, *12*, 1085.
(267) Sawner, A. S.; Ray, S.; Yadav, P.; Mukherjee, S.; Panigrahi, R.; Poudyal, M.; Patel, K.; Ghosh, D.; Kummerant, E.; Kumar, A.; et al. Modulating alpha-Synuclein Liquid-Liquid Phase Separation. *Biochemistry* **2021**, *60*, 3676−3696.
(268) Gabryelczyk, B.; Cai, H.; Shi, X.; Sun, Y.; Swinkels, P. J. M.; Salentinig, S.; Pervushin, K.; Miserez, A. Hydrogen Bond Guidance and Aromatic Stacking Drive Liquid-Liquid Phase Separation of Intrinsically Disordered Histidine-Rich Peptides. *Nat. Commun.* **2019**, *10*, 5465.
(269) Zhang, Y.; Prasad, R.; Su, S.; Lee, D.; Zhou, H.-X. Amino Acid-Dependent Material Properties of Tetrapeptide Condensates. *bioRxiv* **2024**, *123*, 358a.
(270) Hicks, A.; Escobar, C. A.; Cross, T. A.; Zhou, H. X. Sequence-Dependent Correlated Segments in the Intrinsically Disordered Region of ChiZ. *Biomolecules* **2020**, *10*, 946.
(271) Dey, S.; MacAinsh, M.; Zhou, H. X. Sequence-Dependent Backbone Dynamics of Intrinsically Disordered Proteins. *J. Chem. Theory Comput.* **2022**, *18*, 6310−6323.
(272) den Dunnen, J. T.; Moormann, R. J. M.; Lubsen, N. H.; Schoenmakers, J. G. G. Concerted and Divergent Evolution within the Rat γ-Crystallin Gene Family. *J. Mol. Biol.* **1986**, *189*, 37−46.
(273) Meakin, S. O.; Du, R. P.; Tsui, L.-C.; Breitman, M. L. γ-Crystallins of the Human Eye Lens: Expression Analysis of Five Members of the Gene Family. *Mol. Cell. Biol.* **1987**, *7*, 2671−2679.
(274) Norledge, B. V.; Hay, R. E.; Bateman, O. A.; Slingsby, C.; Driessen, H. P. Towards a Molecular Understanding of Phase Separation in the Lens: A Comparison of the X-Ray Structures of Two High Tc gamma-Crystallins, gammaE and gammaF, with Two Low Tc gamma-Crystallins, gammab and gammaD. *Exp. Eye Res.* **1997**, *65*, 609−630.
(275) Cinar, S.; Cinar, H.; Chan, H. S.; Winter, R. Pressure-Sensitive and Osmolyte-Modulated Liquid-Liquid Phase Separation of Eye-Lens gamma-Crystallins. *J. Am. Chem. Soc.* **2019**, *141*, 7347−7354.
(276) White, H. E.; Driessen, H. P.; Slingsby, C.; Moss, D. S.; Lindley, P. F. Packing Interactions in the Eye-Lens. Structural Analysis, Internal Symmetry and Lattice Interactions of Bovine gamma IVa-Crystallin. *J. Mol. Biol.* **1989**, *207*, 217−235.
(277) Taratuta, V. G.; Holschbach, A.; Thurston, G. M.; Blankschtein, D.; Benedek, G. B. Liquid-Liquid Phase Separation of Aqueous Lysozyme Solutions: Effects of pH and Salt Identity. *J. Phys. Chem.* **1990**, *94*, 2140−2144.
(278) Zhang, Y.; Cremer, P. S. The Inverse and Direct Hofmeister Series for Lysozyme. *Proc. Natl. Acad. Sci. U.S.A.* **2009**, *106*, 15249−15253.
(279) Kim, J.; Qin, S.; Zhou, H. X.; Rosen, M. K. Surface Charge Can Modulate Phase Separation of Multidomain Proteins. *J. Am. Chem. Soc.* **2024**, *146*, 3383−3395.
(280) Song, J.; Zhang, Z.; Hu, W.; Chen, Y. Small Ubiquitin-like Modifier (SUMO) Recognition of a SUMO Binding Motif: A Reversal of the Bound Orientation. *J. Biol. Chem.* **2005**, *280*, 40122−40129.
(281) Tamura, T.; Yamaoka, T.; Kunugi, S.; Panitch, A.; Tirrell, D. A. Effects of Temperature and Pressure on the Aggregation Properties of an Engineered Elastin Model Polypeptide in Aqueous Solution. *Biomacromolecules* **2000**, *1*, 552−555.
(282) Möller, J.; Grobelny, S.; Schulze, J.; Bieder, S.; Steffen, A.; Erlkamp, M.; Paulus, M.; Tolan, M.; Winter, R. Reentrant Liquid-Liquid Phase Separation in Protein Solutions at Elevated Hydrostatic Pressures. *Phys. Rev. Lett.* **2014**, *112*, 028101.
(283) Cinar, H.; Cinar, S.; Chan, H. S.; Winter, R. Pressure-Induced Dissolution and Reentrant Formation of Condensed, Liquid-Liquid Phase-Separated Elastomeric α-Elastin. *Chem. Eur. J.* **2018**, *24*, 8286−8291.
(284) Cinar, H.; Fetahaj, Z.; Cinar, S.; Vernon, R. M.; Chan, H. S.; Winter, R. H. A. Temperature, Hydrostatic Pressure, and Osmolyte Effects on Liquid-Liquid Phase Separation in Protein Condensates: Physical Chemistry and Biological Implications. *Chem. Eur. J.* **2019**, *25*, 13049−13069.
(285) Cinar, H.; Oliva, R.; Lin, Y.-H.; Chen, X.; Zhang, M.; Chan, H. S.; Winter, R. Pressure Sensitivity of SynGAP/PSD-95 Condensates as a Model for Postsynaptic Densities and Its Biophysical and Neurological Ramifications. *Chem. Eur. J.* **2020**, *26*, 11024−11031.
(286) Roche, J.; Caro, J. A.; Norberto, D. R.; Barthe, P.; Roumestand, C.; Schlessman, J. L.; Garcia, A. E.; García-Moreno E, B.; Royer, C. A.

AQ

Cavities Determine the Pressure Unfolding of Proteins. *Proc. Natl. Acad. Sci. U.S.A.* **2012**, *109*, 6945−6950.
(287) Wang, J.; Choi, J. M.; Holehouse, A. S.; Lee, H. O.; Zhang, X.; Jahnel, M.; Maharana, S.; Lemaitre, R.; Pozniakovsky, A.; Drechsel, D.; et al. A Molecular Grammar Governing the Driving Forces for Phase Separation of Prion-like RNA Binding Proteins. *Cell* **2018**, *174*, 688−699.
(288) Dzuricky, M.; Rogers, B. A.; Shahid, A.; Cremer, P. S.; Chilkoti, A. De novo Engineering of Intracellular Condensates Using Artificial Disordered Proteins. *Nat. Chem.* **2020**, *12*, 814−825.
(289) Schuster, B. S.; Dignon, G. L.; Tang, W. S.; Kelley, F. M.; Ranganath, A. K.; Jahnke, C. N.; Simpkins, A. G.; Regy, R. M.; Hammer, D. A.; Good, M. C.; et al. Identifying Sequence Perturbations to an Intrinsically Disordered Protein That Determine Its Phase-Separation Behavior. *Proc. Natl. Acad. Sci. U.S.A.* **2020**, *117*, 11421−11431.
(290) Wong, L. E.; Kim, T. H.; Muhandiram, D. R.; Forman-Kay, J. D.; Kay, L. E. NMR Experiments for Studies of Dilute and Condensed Protein Phases: Application to the Phase-Separating Protein CAPRIN1. *J. Am. Chem. Soc.* **2020**, *142*, 2471−2489.
(291) Bremer, A.; Farag, M.; Borcherds, W. M.; Peran, I.; Martin, E. W.; Pappu, R. V.; Mittag, T. Deciphering How Naturally Occurring Sequence Features Impact the Phase Behaviours of Disordered Prion-like Domains. *Nat. Chem.* **2022**, *14*, 196−207.
(292) Qin, S.; Zhou, H. X. Predicting the Sequence-Dependent Backbone Dynamics of Intrinsically Disordered Proteins. *eLife* **2023**, *12*, RP88958.
(293) Boisvert, F. M.; van Koningsbruggen, S.; Navascues, J.; Lamond, A. I. The Multifunctional Nucleolus. *Nat. Rev. Mol. Cell Biol.* **2007**, *8*, 574−585.
(294) Updike, D. L.; Strome, S. A Genomewide RNAi Screen for Genes That Affect the Stability, Distribution and Function of P Granules in *Caenorhabditis elegans*. *Genetics* **2009**, *183*, 1397−1419.
(295) Updike, D.; Strome, S. P Granule Assembly and Function in *Caenorhabditis elegans* Germ Cells. *J. Androl.* **2010**, *31*, 53−60.
(296) Jain, S.; Wheeler, J. R.; Walters, R. W.; Agrawal, A.; Barsic, A.; Parker, R. ATPase-Modulated Stress Granules Contain a Diverse Proteome and Substructure. *Cell* **2016**, *164*, 487−498.
(297) Hubstenberger, A.; Courel, M.; Benard, M.; Souquere, S.; Ernoult-Lange, M.; Chouaib, R.; Yi, Z.; Morlot, J. B.; Munier, A.; Fradet, M.; et al. P-Body Purification Reveals The Condensation Of Repressed mRNA Regulons. *Mol. Cell* **2017**, *68*, 144−157.
(298) Nguemaha, V.; Zhou, H. X. Liquid-Liquid Phase Separation of Patchy Particles Illuminates Diverse Effects of Regulatory Components on Protein Droplet Formation. *Sci. Rep.* **2018**, *8*, 6728.
(299) Ruff, K. M.; Dar, F.; Pappu, R. V. Ligand Effects on Phase Separation of Multivalent Macromolecules. *Proc. Natl. Acad. Sci. U.S.A.* **2021**, *118*, No. e2017184118.
(300) Ghosh, A.; Zhou, H. X. Determinants for Fusion Speed of Biomolecular Droplets. *Angew. Chem., Int. Ed.* **2020**, *59*, 20837−20840.
(301) Rowlinson, J. S.; Widom, B. *Molecular Theory of Capillarity*; Dover Publications, Inc.: Mineola, NY, 2002.
(302) Kirkwood, J. G.; Buff, F. P. The Statistical Mechanical Theory of Surface Tension. *J. Chem. Phys.* **1949**, *17*, 338−343.
(303) Irving, J. H.; Kirkwood, J. G. The Statistical Mechanical Theory of Transport Processes. IV. The Equations of Hydrodynamics. *J. Chem. Phys.* **1950**, *18*, 817−829.
(304) Ghoufi, A.; Malfreyt, P.; Tildesley, D. J. Computer Modelling of the Surface Tension of the Gas-Liquid and Liquid-Liquid Interface. *Chem. Soc. Rev.* **2016**, *45*, 1387−1409.
(305) Benayad, Z.; von Bulow, S.; Stelzl, L. S.; Hummer, G. Simulation of FUS Protein Condensates with an Adapted Coarse-Grained Model. *J. Chem. Theory Comput.* **2021**, *17*, 525−537.
(306) Pyo, A. G. T.; Zhang, Y.; Wingreen, N. S. Surface Tension and Super-Stoichiometric Surface Enrichment in Two-Component Biomolecular Condensates. *iScience* **2022**, *25*, 103852.
(307) Pyo, A. G. T.; Zhang, Y.; Wingreen, N. S. Proximity to Criticality Predicts Surface Properties of Biomolecular Condensates. *Proc. Natl. Acad. Sci. U.S.A.* **2023**, *120*, No. e2220014120.
(308) Shi, K.; Smith, E. R.; Santiso, E. E.; Gubbins, K. E. A Perspective on the Microscopic Pressure (Stress) Tensor: History, Current Understanding, and Future Challenges. *J. Chem. Phys.* **2023**, *158*, 040901.
(309) Widom, B. Surface Tension and Molecular Correlations near the Critical Point. *J. Chem. Phys.* **1965**, *43*, 3892−3897.
(310) Wang, H.; Kelley, F. M.; Milovanovic, D.; Schuster, B. S.; Shi, Z. Surface Tension and Viscosity of Protein Condensates Quantified by Micropipette Aspiration. *Biophys. Rep.* **2021**, *1*, 100011.
(311) Ghosh, A.; Kota, D.; Zhou, H. X. Shear Relaxation Governs Fusion Dynamics of Biomolecular Condensates. *Nat. Commun.* **2021**, *12*, 5995.
(312) Jawerth, L. M.; Ijavi, M.; Ruer, M.; Saha, S.; Jahnel, M.; Hyman, A. A.; Julicher, F.; Fischer-Friedrich, E. Salt-Dependent Rheology and Surface Tension of Protein Condensates Using Optical Traps. *Phys. Rev. Lett.* **2018**, *121*, 258101.
(313) Zhou, H. X. Determination of Condensate Material Properties from Droplet Deformation. *J. Phys. Chem. B* **2020**, *124*, 8372−8379.
(314) Ashkin, A.; Dziedzic, J. M.; Bjorkholm, J. E.; Chu, S. Observation of a Single-Beam Gradient Force Optical Trap for Dielectric Particles. *Opt. Lett.* **1986**, *11*, 288.
(315) Lim, S.; Moon, D.; Kim, H. J.; Seo, J. H.; Kang, I. S.; Cha, H. J. Interfacial Tension of Complex Coacervated Mussel Adhesive Protein According to the Hofmeister Series. *Langmuir* **2014**, *30*, 1108−1115.
(316) Fedorov, D.; Roas-Escalona, N.; Tolmachev, D.; Harmat, A. L.; Scacchi, A.; Sammalkorpi, M.; Aranko, A. S.; Linder, M. B. Triblock Proteins with Weakly Dimerizing Terminal Blocks and an Intrinsically Disordered Region for Rational Design of Condensate Properties. *Small* **2024**, *20*, No. e2306817.
(317) Folkmann, A. W.; Putnam, A.; Lee, C. F.; Seydoux, G. Regulation of Biomolecular Condensates by Interfacial Protein Clusters. *Science* **2021**, *373*, 1218−1224.
(318) Zhou, H. X. Viscoelasticity of Biomolecular Condensates Conforms to the Jeffreys Model. *J. Chem. Phys.* **2021**, *154*, 041103.
(319) Ijavi, M.; Style, R. W.; Emmanouilidis, L.; Kumar, A.; Meier, S. M.; Torzynski, A. L.; Allain, F. H. T.; Barral, Y.; Steinmetz, M. O.; Dufresne, E. R. Surface Tensiometry of Phase Separated Protein and Polymer Droplets by the Sessile Drop Method. *Soft Matter* **2021**, *17*, 1655−1662.
(320) Testa, A.; Dindo, M.; Rebane, A. A.; Nasouri, B.; Style, R. W.; Golestanian, R.; Dufresne, E. R.; Laurino, P. Sustained Enzymatic Activity and Flow in Crowded Protein Droplets. *Nat. Commun.* **2021**, *12*, 6293.
(321) Holland, J.; Castrejón-Pita, A. A.; Tuinier, R.; Aarts, D. G. A. L.; Nott, T. J. Surface Tension Measurement and Calculation of Model Biomolecular Condensates. *Soft Matter* **2023**, *19*, 8706−8716.
(322) Kota, D.; Zhou, H. X. Macromolecular Regulation of the Material Properties of Biomolecular Condensates. *J. Phys. Chem. Lett.* **2022**, *13*, 5285−5290.
(323) Bergeron-Sandoval, L.-P.; Kumar, S.; Heris, H. K.; Chang, C. L. A.; Cornell, C. E.; Keller, S. L.; Francois, P.; Hendricks, A. G.; Ehrlicher, A. J.; Pappu, R. V.; Michnick, S. W.; et al. Endocytic Proteins with Prion-like Domains Form Viscoelastic Condensates That Enable Membrane Remodeling. *Proc. Natl. Acad. Sci. U.S.A.* **2021**, *118*, No. e2113789118.
(324) Taylor, N.; Elbaum-Garfinkle, S.; Vaidya, N.; Zhang, H.; Stone, H. A.; Brangwynne, C. P. Biophysical Characterization of Organelle-Based RNA/Protein Liquid Phases Using Microfluidics. *Soft Matter* **2016**, *12*, 9142−9150.
(325) Alshareedah, I.; Thurston, G. M.; Banerjee, P. R. Quantifying Viscosity and Surface Tension of Multicomponent Protein-Nucleic Acid Condensates. *Biophys. J.* **2021**, *120*, 1161−1169.
(326) Sahu, S.; Chauhan, P.; Lumen, E.; Moody, K.; Peddireddy, K.; Mani, N.; Subramanian, R.; Robertson-Anderson, R.; Wolfe, A. J.; Ross, J. L. Interplay of Self-Organization of Microtubule Asters and Crosslinking Protein Condensates. *PNAS Nexus* **2023**, *2*, pgad231.
(327) Sato, Y.; Takinoue, M. Sequence-Dependent Fusion Dynamics and Physical Properties of DNA Droplets. *Nanoscale Adv.* **2023**, *5*, 1919−1925.

https://doi.org/10.1021/acs.chemrev.4c00138
Chem. Rev. XXXX, XXX, XXX−XXX

(328) Oestreicher, H. L. Field and Impedance of an Oscillating Sphere in a Viscoelastic Medium with an Application to Biophysics. *J. Acoust. Soc. Am.* **1951**, *23*, 707−714.
(329) Ziemann, F.; Radler, J.; Sackmann, E. Local Measurements of Viscoelastic Moduli of Entangled Actin Networks Using an Oscillating Magnetic Bead Micro-Rheometer. *Biophys. J.* **1994**, *66*, 2210−2216.
(330) Slie, W. M.; Donfor, A. R.; Litovitz, T. A. Ultrasonic Shear and Longitudinal Measurements in Aqueous Glycerol. *J. Chem. Phys.* **1966**, *44*, 3712−3718.
(331) O'Sullivan, T. J.; Kannam, S. K.; Chakraborty, D.; Todd, B. D.; Sader, J. E. Viscoelasticity of Liquid Water Investigated Using Molecular Dynamics Simulations. *Phys. Rev. Fluids* **2019**, *4*, 123302.
(332) Jawerth, L.; Fischer-Friedrich, E.; Saha, S.; Wang, J.; Franzmann, T.; Zhang, X.; Sachweh, J.; Ruer, M.; Ijavi, M.; Saha, S.; et al. Protein Condensates as Aging Maxwell Fluids. *Science* **2020**, *370*, 1317−1323.
(333) Green, M. S. Markoff Random Processes and the Statistical Mechanics of Time-Dependent Phenomena. II. Irreversible Processes in Fluids. *J. Chem. Phys.* **1954**, *22*, 398−413.
(334) Kubo, R. Statistical-Mechanical Theory of Irreversible Processes. I. General Theory and Simple Applications to Magnetic and Conduction Problems. *J. Phys. Soc. Jpn.* **1957**, *12*, 570−586.
(335) Maginn, E. J.; Messerly, R. A.; Carlson, D. J.; Roe, D. R.; Elliot, J. R. Best Practices for Computing Transport Properties 1. Self-Diffusivity and Viscosity from Equilibrium Molecular Dynamics [Article v1.0]. *Living J. Comput. Mol. Sci.* **2019**, *1*, 6324.
(336) Tejedor, A. R.; Collepardo-Guevara, R.; Ramírez, J.; Espinosa, J. R. Time-Dependent Material Properties of Aging Biomolecular Condensates from Different Viscoelasticity Measurements in Molecular Dynamics Simulations. *J. Phys. Chem. B* **2023**, *127*, 4441−4459.
(337) McLennan, J. A., Jr Statistical Mechanics of Transport in Fluids. *Phys. Fluids* **1960**, *3*, 493−502.
(338) Zwanzig, R. Frequency-Dependent Transport Coefficients in Fluid Mechanics. *J. Chem. Phys.* **1965**, *43*, 714−720.
(339) Tuinier, R.; Dhont, J. K. G.; Fan, T. H. How Depletion Affects Sphere Motion through Solutions Containing Macromolecules. *Europhys. Lett.* **2006**, *75*, 929.
(340) Ando, T.; Skolnick, J. Crowding and Hydrodynamic Interactions likely Dominate in vivo Macromolecular Motion. *Proc. Natl. Acad. Sci. U.S.A.* **2010**, *107*, 18457−18462.
(341) Petit, L.; Barentin, C.; Colombani, J.; Ybert, C.; Bocquet, L. Size Dependence of Tracer Diffusion in a Laponite Colloidal Gel. *Langmuir* **2009**, *25*, 12048−12055.
(342) Yeh, I.-C.; Hummer, G. System-Size Dependence of Diffusion Coefficients and Viscosities from Molecular Dynamics Simulations with Periodic Boundary Conditions. *J. Phys. Chem. B* **2004**, *108*, 15873−15879.
(343) Valentine, M. T.; Dewalt, L. E.; Ou-Yang, H. D. Forces on a Colloidal Particle in a Polymer Solution: A Study Using Optical Tweezers. *J. Condens. Matter Phys.* **1996**, *8*, 9477−9482.
(344) Michieletto, D.; Marenda, M. Rheology and Viscoelasticity of Proteins and Nucleic Acids Condensates. *JACS Au* **2022**, *2*, 1506−1521.
(345) Elson, E. L.; Magde, D. Fluorescence Correlation Spectroscopy. I. Conceptual Basis and Theory. *Biopolymers* **1974**, *13*, 1−27.
(346) Rigler, R.; Elson, E. S. *Fluorescence Correlation Spectroscopy. Theory and Applications*; Springer: Berlin, 2001.
(347) Mason, T. G.; Weitz, D. A. Optical Measurements of Frequency-Dependent Linear Viscoelastic Moduli of Complex Fluids. *Phys. Rev. Lett.* **1995**, *74*, 1250−1253.
(348) Tassieri, M.; Gibson, G. M.; Evans, R. M. L.; Yao, A. M.; Warren, R.; Padgett, M. J.; Cooper, J. M. Measuring Storage and Loss Moduli Using Optical Tweezers: Broadband Microrheology. *Phys. Rev. E* **2010**, *81*, 026308.
(349) Preece, D.; Warren, R.; Evans, R. M. L.; Gibson, G. M.; Padgett, M. J.; Cooper, J. M.; Tassieri, M. Optical Tweezers: Wideband Microrheology. *J. Opt.* **2011**, *13*, 044022.
(350) Malay, A. D.; Suzuki, T.; Katashima, T.; Kono, N.; Arakawa, K.; Numata, K. Spider Silk Self-Assembly via Modular Liquid-Liquid Phase Separation and Nanofibrillation. *Sci. Adv.* **2020**, *6*, No. eabb6030.
(351) Chatterjee, S.; Kan, Y.; Brzezinski, M.; Koynov, K.; Regy, R. M.; Murthy, A. C.; Burke, K. A.; Michels, J. J.; Mittal, J.; Fawzi, N. L.; Parekh, S. H.; et al. Reversible Kinetic Trapping of FUS Biomolecular Condensates. *Adv. Sci.* **2022**, *9*, No. e2104247.
(352) Shen, Z.; Jia, B.; Xu, Y.; Wessén, J.; Pal, T.; Chan, H. S.; Du, S.; Zhang, M. Biological Condensates Form Percolated Networks with Molecular Motion Properties Distinctly Different from Dilute Solutions. *eLife* **2023**, *12*, No. e81907.
(353) Alshareedah, I.; Moosa, M. M.; Pham, M.; Potoyan, D. A.; Banerjee, P. R. Programmable Viscoelasticity in Protein-RNA Condensates with Disordered Sticker-Spacer Polypeptides. *Nat. Commun.* **2021**, *12*, 6620.
(354) Tanaka, F.; Edwards, S. F. Viscoelastic Properties of Physically Crosslinked Networks. 1. Transient Network Theory. *Macromolecules* **1992**, *25*, 1516−1523.
(355) Tripathi, A.; Tam, K. C.; McKinley, G. H. Rheology and Dynamics of Associative Polymers in Shear and Extension: Theory and Experiments. *Macromolecules* **2006**, *39*, 1981−1999.
(356) Platani, M.; Goldberg, I.; Swedlow, J. R.; Lamond, A. I. In Vivo Analysis of Cajal Body Movement, Separation, and Joining in Live Human Cells. *J. Cell Biol.* **2000**, *151*, 1561−1574.
(357) Brangwynne, C. P.; Mitchison, T. J.; Hyman, A. A. Active Liquid-Like Behavior of Nucleoli Determines Their Size and Shape in *Xenopus laevis* Oocytes. *Proc. Natl. Acad. Sci. U.S.A.* **2011**, *108*, 4334−4339.
(358) Hubstenberger, A.; Noble, S. L.; Cameron, C.; Evans, T. C. Translation Repressors, an RNA Helicase, and Developmental Cues Control RNP Phase Transitions during Early Development. *Dev. Cell* **2013**, *27*, 161−173.
(359) Kim, J.; Han, K. Y.; Khanna, N.; Ha, T.; Belmont, A. S. Nuclear Speckle Fusion via Long-Range Directional Motion Regulates Speckle Morphology after Transcriptional Inhibition. *J. Cell Sci.* **2019**, *132*, jcs226563.
(360) Martínez-Herrera, J. I.; Derby, J. J. Viscous Sintering of Spherical Particles via Finite Element Analysis. *J. Am. Ceram. Soc.* **1995**, *78*, 645−649.
(361) Wakai, F.; Katsura, K.; Kanchika, S.; Shinoda, Y.; Akatsu, T.; Shinagawa, K. Sintering Force behind the Viscous Sintering of Two Particles. *Acta Mater.* **2016**, *109*, 292−299.
(362) Elbaum-Garfinkle, S.; Kim, Y.; Szczepaniak, K.; Chen, C. C.; Eckmann, C. R.; Myong, S.; Brangwynne, C. P. The Disordered P Granule Protein LAF-1 Drives Phase Separation into Droplets with Tunable Viscosity and Dynamics. *Proc. Natl. Acad. Sci. U.S.A.* **2015**, *112*, 7189−7194.
(363) Erkamp, N. A.; Sneideris, T.; Ausserwoger, H.; Qian, D.; Qamar, S.; Nixon-Abell, J.; St George-Hyslop, P.; Schmit, J. D.; Weitz, D. A.; Knowles, T. P. J. Spatially Non-Uniform Condensates Emerge from Dynamically Arrested Phase Separation. *Nat. Commun.* **2023**, *14*, 684.
(364) Hernandez-Candia, C. N.; Brady, B. R.; Harrison, E.; Tucker, C. L. A Platform to Induce and Mature Biomolecular Condensates Using Chemicals and Light. *Nat. Chem. Biol.* **2024**, *20*, 452−462.
(365) Gui, X.; Luo, F.; Li, Y.; Zhou, H.; Qin, Z.; Liu, Z.; Gu, J.; Xie, M.; Zhao, K.; Dai, B.; et al. Structural Basis For Reversible Amyloids of hnRNPA1 Elucidates Their Role in Stress Granule Assembly. *Nat. Commun.* **2019**, *10*, 2006.
(366) Kaur, T.; Alshareedah, I.; Wang, W.; Ngo, J.; Moosa, M. M.; Banerjee, P. R. Molecular Crowding Tunes Material States of Ribonucleoprotein Condensates. *Biomolecules* **2019**, *9*, 71.
(367) Xu, D.; Hawk, J. L.; Loveless, D. M.; Jeon, S. L.; Craig, S. L. Mechanism of Shear Thickening in Reversibly Cross-Linked Supramolecular Polymer Networks. *Macromolecules* **2010**, *43*, 3556−3565.
(368) Suzuki, S.; Uneyama, T.; Inoue, T.; Watanabe, H. Nonlinear Rheology of Telechelic Associative Polymer Networks: Shear Thickening and Thinning Behavior of Hydrophobically Modified

https://doi.org/10.1021/acs.chemrev.4c00138
Chem. Rev. XXXX, XXX, XXX−XXX

Ethoxylated Urethane (HEUR) in Aqueous Solution. *Macromolecules* **2012**, *45*, 888−898.
(369) West, J. A.; Mito, M.; Kurosaka, S.; Takumi, T.; Tanegashima, C.; Chujo, T.; Yanaka, K.; Kingston, R. E.; Hirose, T.; Bond, C.; et al. Structural, Super-Resolution Microscopy Analysis of Paraspeckle Nuclear Body Organization. *J. Cell Biol.* **2016**, *214*, 817−830.
(370) Fei, J.; Jadaliha, M.; Harmon, T. S.; Li, I. T. S.; Hua, B.; Hao, Q.; Holehouse, A. S.; Reyer, M.; Sun, Q.; Freier, S. M.; et al. Quantitative Analysis of Multilayer Organization of Proteins and RNA in Nuclear Speckles at Super Resolution. *J. Cell Sci.* **2017**, *130*, 4180−4192.
(371) Sanders, D. W.; Kedersha, N.; Lee, D. S. W.; Strom, A. R.; Drake, V.; Riback, J. A.; Bracha, D.; Eeftens, J. M.; Iwanicki, A.; Wang, A.; et al. Competing Protein-RNA Interaction Networks Control Multiphase Intracellular Organization. *Cell* **2020**, *181*, 306−324.
(372) Kaur, T.; Raju, M.; Alshareedah, I.; Davis, R. B.; Potoyan, D. A.; Banerjee, P. R. Sequence-Encoded and Composition-Dependent Protein-RNA Interactions Control Multiphasic Condensate Morphologies. *Nat. Commun.* **2021**, *12*, 872.
(373) Kelley, F. M.; Favetta, B.; Regy, R. M.; Mittal, J.; Schuster, B. S. Amphiphilic Proteins Coassemble into Multiphasic Condensates and Act as Biomolecular Surfactants. *Proc. Natl. Acad. Sci. U.S.A.* **2021**, DOI: 10.1073/pnas.2109967118.
(374) Lafontaine, D. L. J.; Riback, J. A.; Bascetin, R.; Brangwynne, C. P. The Nucleolus as a Multiphase Liquid Condensate. *Nat. Rev. Mol. Cell Biol.* **2021**, *22*, 165−182.
(375) Choi, S.; Meyer, M. O.; Bevilacqua, P. C.; Keating, C. D. Phase-Specific RNA Accumulation and Duplex Thermodynamics in Multiphase Coacervate Models for Membraneless Organelles. *Nat. Chem.* **2022**, *14*, 1110−1117.
(376) Garaizar, A.; Espinosa, J. R.; Joseph, J. A.; Krainer, G.; Shen, Y.; Knowles, T. P. J.; Collepardo-Guevara, R. Aging Can Transform Single-Component Protein Condensates into Multiphase Architectures. *Proc. Natl. Acad. Sci. U.S.A.* **2022**, *119*, No. e2119800119.
(377) Gouveia, B.; Kim, Y.; Shaevitz, J. W.; Petry, S.; Stone, H. A.; Brangwynne, C. P. Capillary Forces Generated by Biomolecular Condensates. *Nature* **2022**, *609*, 255−264.
(378) Kim, T.; Yoo, J.; Do, S.; Hwang, D. S.; Park, Y.; Shin, Y. RNA-Mediated Demixing Transition of Low-Density Condensates. *Nat. Commun.* **2023**, *14*, 2425.
(379) Rai, S. K.; Khanna, R.; Avni, A.; Mukhopadhyay, S. Heterotypic Electrostatic Interactions Control Complex Phase Separation of Tau and Prion into Multiphasic Condensates and Co-Aggregates. *Proc. Natl. Acad. Sci. U.S.A.* **2023**, *120*, No. e2216338120.
(380) Feric, M.; Sarfallah, A.; Dar, F.; Temiakov, D.; Pappu, R. V.; Misteli, T. Mesoscale Structure-Function Relationships in Mitochondrial Transcriptional Condensates. *Proc. Natl. Acad. Sci. U.S.A.* **2022**, *119*, No. e2207303119.
(381) Mazarakos, K.; Zhou, H. X. Multiphase Organization Is a Second Phase Transition within Multi-Component Biomolecular Condensates. *J. Chem. Phys.* **2022**, *156*, 191104.
(382) Jacobs, W. M.; Frenkel, D. Phase Transitions in Biological Systems with Many Components. *Biophys. J.* **2017**, *112*, 683−691.
(383) Lin, Y.-H.; Brady, J. P.; Forman-Kay, J. D.; Chan, H. S. Charge Pattern Matching as a 'Fuzzy' Mode of Molecular Recognition for the Functional Phase Separations of Intrinsically Disordered Proteins. *New J. Phys.* **2017**, *19*, 115003.
(384) Jacobs, W. M. Theory and Simulation of Multiphase Coexistence in Biomolecular Mixtures. *J. Chem. Theory Comput.* **2023**, *19*, 3429−3445.
(385) Schmit, J. D.; Bouchard, J. J.; Martin, E. W.; Mittag, T. Protein Network Structure Enables Switching between Liquid and Gel States. *J. Am. Chem. Soc.* **2020**, *142*, 874−883.
(386) Riemenschneider, H.; Guo, Q.; Bader, J.; Frottin, F.; Farny, D.; Kleinberger, G.; Haass, C.; Mann, M.; Hartl, F. U.; Baumeister, W.; et al. Gel-Like Inclusions of C-Terminal Fragments of TDP-43 Sequester Stalled Proteasomes in Neurons. *EMBO Rep.* **2022**, *23*, No. e53890.
(387) Rosenberg, G. M.; Murray, K. A.; Salwinski, L.; Hughes, M. P.; Abskharon, R.; Eisenberg, D. S. Bioinformatic Identification of Previously Unrecognized Amyloidogenic Proteins. *J. Biol. Chem.* **2022**, *298*, 101920.
(388) Mackenzie, I. R.; Nicholson, A. M.; Sarkar, M.; Messing, J.; Purice, M. D.; Pottier, C.; Annu, K.; Baker, M.; Perkerson, R. B.; Kurti, A.; et al. TIA1Mutations in Amyotrophic Lateral Sclerosis and Frontotemporal Dementia Promote Phase Separation and Alter Stress Granule Dynamics. *Neuron* **2017**, *95*, 808−816.
(389) Harmon, T. S.; Holehouse, A. S.; Rosen, M. K.; Pappu, R. V. Intrinsically Disordered Linkers Determine the Interplay between Phase Separation and Gelation in Multivalent Proteins. *eLife* **2017**, *6*, No. e30294.
(390) Hastings, R. L.; Boeynaems, S. Designer Condensates: A Toolkit for the Biomolecular Architect. *J. Mol. Biol.* **2021**, *433*, 166837.
(391) Do, S.; Lee, C.; Lee, T.; Kim, D.-N.; Shin, Y. Engineering DNA-Based Synthetic Condensates with Programmable Material Properties, Compositions, and Functionalities. *Sci. Adv.* **2022**, *8*, No. eabj1771.
(392) Dai, Y.; You, L.; Chilkoti, A. Engineering Synthetic Biomolecular Condensates. *Nat. Rev. Bioeng.* **2023**, *1*, 466−480.
(393) Ji, R.; Wang, L.; Shang, Y.; Du, S.; Xiao, Y.; Dong, W.; Cui, L.; Gao, R.; Ren, K. RNA Condensate as a Versatile Platform for Improving Fluorogenic RNA Aptamer Properties and Cell Imaging. *J. Am. Chem. Soc.* **2024**, *146*, 4402−4411.

https://doi.org/10.1021/acs.chemrev.4c00138
Chem. Rev. XXXX, XXX, XXX−XXX